This is to certify that the
dissertation entitled

CRYSTALLOGRAPHIC AND PROTEIN ENGINEERING STUDIES OF THE STRUCTURE AND FUNCTION OF CYTOCHROME C OXIDASE FROM RHODOBACTER SPHAEROIES

presented by

JIAN LIU

has been accepted towards fulfillment
of the requirements for the

Ph. D. degree in CELL AND MOLECULAR BIOLOGY

S. Ferguson-Miller
Major Professor's Signature

Dec 16, 2010
Date

CRYSTALLOGRAPHIC AND PROTEIN ENGINEERING STUDIES OF THE STRUCTURE AND FUNCTION OF CYTOCHROME *C* OXIDASE FROM *RHODOBACTER SPHAEROIDES*

By

Jian Liu

A DISSERTATION

Submitted to
Michigan State University
In partial fulfillment of the requirement
for the degree of

DOCTOR OF PHILOSOPHY

Cell and Molecular Biology

2010

ABSTRACT

CRYSTALLOGRAPHIC AND PROTEIN ENGINEERING STUDIES OF THE ATESTRUCTURE AND FUNCTION OF CYTOCHROME *C* OXIDASE FROM *RHODOBACTER SPHAEROIDES*

BY

Jian Liu

Cytochrome *c* oxidase (C*c*O) is the terminal enzyme of mitochondrial and bacterial respiratory chains. It accepts electrons from cytochrome *c* and reduces oxygen to water. Driven by this process, protons are translocated across the mitochondrial inner membrane of eukaryotes or the periplasmic membrane of prokaryotes, forming a transmembrane proton gradient that is used for the synthesis of ATP. Cytochrome *c* oxidase from *Rhodobacter sphaeroides* (*Rs*C*c*O), a homologue of mammalian C*c*O, is used as the research model for structural and functional studies in this thesis.

A *Rs*C*c*O-EYFP (Enhance Yellow Fluorescent Protein) fusion protein was created to increase the hydrophilic portion of C*c*O and form better crystal contacts. Activity and proton pumping assays showed that the fusion protein was fully active. Reconstituted vesicle results also showed that the pH-sensitive EYFP in this fusion protein could be used as a pH indicator for the study of the proton pumping mechanism. Two mutants of *Rs*C*c*O with different shortened subunit I C-termini were constructed and crystallized. The 16 residue deletion mutant (PJL33) showed lower activity at high pH and weak proton pumping, suggesting that the deletion affected the stability of the subunit III interaction with the enzyme. The crystal structure of PJL33 (2.10 Å) also showed a

conformational change at the new C-terminus, which could contribute to the activity changes. The 6 residue deletion mutant (PJL49) showed normal activity except a diminished proton pumping function. The crystal of PJL49 diffracted to 2.5 Å. In neither case did the removal of flexible regions result in higher resolution four subunit crystals, as hoped. High resolution crystal structures were obtained of the two mutants that define the proton uptake pathways in *Rs*C*c*O, D132A and K362M. In the oxidized crystal of D132A (2.15Å), the mutation caused no change in overall structure, but a localized conformational change in the D132 region. A chloride ion replaced the D132 carboxyl position and the backbone of residues 130 to 135 shifted, causing a conformational change of N207 and loss of its bound water. These changes could block proton uptake in the D-pathway and account for the strong inhibition. The oxidized crystal structure of the proton path mutant, K362M (2.30 Å), showed no significant overall structural changes, in spite of major inhibition, except for the loss of two waters adjacent to K362 and T359. This result supports the critical role for water molecules in proton uptake. Crystal structures of reduced forms of both K362M (2.50 Å) and D132A (2.15 Å) showed similar conformational changes as seen in WT, supporting the importance of redox-induced conformational effects. Spectra taken during X-ray radiation of the oxidized crystals showed reduction of the metal centers, but indicated a strained configuration that only relaxes to a native reduced form upon annealing. The results explain the ability to observe conformational differences between oxidized and reduced crystal forms.

ACKNOWLEDGEMENTS

First I would like to express my sincere thanks to my mentor, Dr. Shelagh Ferguson-Miller, for her kind support and guidance on my Ph. D. research during these years. Her wisdom, knowledge and enthusiasm in science have always inspired and motivated me. It is impossible to finish this dissertation without her.

I am very grateful to my graduate committee members Dr. Robert Hausinger, Dr. David Weliky, Dr. Zachary Burton and Dr. Gregory Zeikus, for their advice and support throughout my Ph. D. program.

I also want to thank my present and past lab mates for their valuable help and priceless friendship. I thank Dr. Carrie Hiser for all the guidance on the molecular biology techniques and for reading through my dissertation. Several important strains that were used in this dissertation were made by Dr. Carrie. I thank Dr. Denise Mills for the advices on making of the oxidase vesicles and she taught me how to use the stop-flow instrument. I thank Dr. Ling Qin for the guidance on crystallography. He taught me from the growing of crystals to the analysis and refinement of the crystal data sets. I thank Dr. Martyn Sharpe for the discussions on the mechanisms involved in cytochrome c oxidase. I also want to thank Dr. Bryan Schmidt, Dr. Namjoon Kim, Dr. Xi Zhang, Dr. Shujuan Xu, Fei Li and Leann Buhrow for their help and discussions. Dr. Namjoon Kim also helped me on the research of oxidase vesicles. Dr. Xi Zhang helped me to understand the mass spectrometry data of cytochrome c oxidase. I thank Fei Li and Leann for the advices and helping on defense presentation preparation. I also thank all the past and present

undergraduate students who have helped me growing bacteria, making reagents, and preparing cell membranes.

I also want to thank Dr R. Michael Garavito and Dr. Kaillathe Padmanabhan (Pappan) for the guidance and advices on the crystallography. Members of the Dr. Garavito Lab, Yi Zheng and Yanfeng Zhang also gave me lots of help during the synchrotron trips. Dr. Kaillathe Padmanabhan also helped me with computer hardware and software problems. I also thank Dr. Neil R. Bowlby and Dr. Steve A Seibold for the discussion and advices on the research of cytochrome c oxidase.

I thank staff scientists at LS-CAT, GM/CA-CAT, and BioCars at Advanced Photon Source, Argonne National Laboratory, particularly Dr. Joseph S. Brunzelle and Dr. Zdzislaw Wawrzak for their training, Dr. Vukica Srajer and Dr. Yu-Sheng Chen for the support and helpful suggestions on online spectra data collections.

Finally I would like to thank my parents and my sister, for their support and encouragement. Thank you all for everything.

TABLE OF CONTENTS

LIST OF TABLES

LIST OF FIGURES

ABBREVIATIONS

ATP	adenosine triphosphate
A. U.	asymmetric unit
BCA	bicinchroninic acid
BSA	bovine serum albumin
C*c*O	cytochrome *c* oxidase
CCCP	Carbonyl cyanide *m*-chlorophenyl hydrazone
COV	cytochrome *c* oxidase vesicle
DEAE	diethylaminoethyl
DDM	dodecyl maltoside
DM	decyl maltoside
EDTA	ethylenediaminetetraacetic acid
EYFP	enhanced yellow fluorescence protein
$FADH_2$	reduced form of flavin adenine dinucleotie
FCCP	trifluorocarbonylcyanide phenylhydrazone
FPLC	fast protein liquid chromatography
FRET	Förster /fluorescence resonance energy transfer
FITC	fluorescein isothiocyanate
GFP	green fluorescent protein
HEPES	4-(2-hydroxyethyl)-1-piperazineethanesulfonic acid
kD	kilodalton
LDAO	lauryl dimethylamine *n*-oxide

MD	molecular dynamics
MES	2-(*n*-morpholino)ethanesulfonic acid
NADH	reduced form of nicotinamide adenine dinucleotide
Ni-NTA	nickel-nitrilotriacetic acid
NMR	Nuclear magnetic resonance
PCR	polymerase chain reaction
Pd	*Paracoccus denitrificans*
PEG	polyethylene glycol
Rs	*Rhodobacter sphaeroides*
SDS-PAGE	sodium dodecyl sulfate polyacrylamide gel eletrophoresis
Tris	tris (hydroxymethyl) aminomethane
RCR	respiratory control ratio
WT	wild type

CHAPTER 1. INTRODUCTION

1. Background on cytochrome *c* oxidase

1.1 Energy metabolism and the respiratory chain

Energy metabolism is a very important aspect of all living organisms. From simple organisms such as bacteria to complicated eukaryotes such as mammals, a continuous supply of energy is always required to perform all the necessary functions to support life. Through catabolic metabolism, energy-containing nutrient molecules such as carbohydrates, fats, and proteins are degraded into smaller, energy-depleted products such as H_2O, CO_2, and NH_3. The energy released in this process is then stored in the form of ATP and reduced electron carriers (NADH, NADPH, and $FADH_2$). Catabolism consists of sequential metabolic pathways including glycolysis and fatty acid oxidation, citric acid cycle, and oxidative phophorylation to produce a useful chemical energy currency, ATP. Oxidative phosphorylation is a highly efficient energy-converting process. It involves the reduction of O_2 to H_2O with electrons donated by NADH and $FADH_2$. The electron flow takes place through the respiratory chain (electron transfer chain) in the inner membrane of mitochondria in eukaryotes, or the cytoplasmic membrane in prokaryotes. The free energy generated by electron flow in the respiratory chain is conserved in the form of a pH gradient and transmembrane electrochemical potential.

The respiratory chain consists of a series of transmembrane protein complexes (shown in Figure 1.1). Complex I (NADH dehydrogenase) and Complex II (succinate dehydrogenase) catalyze electron transfer to ubiquinone from soluble electron donors such as NADH and

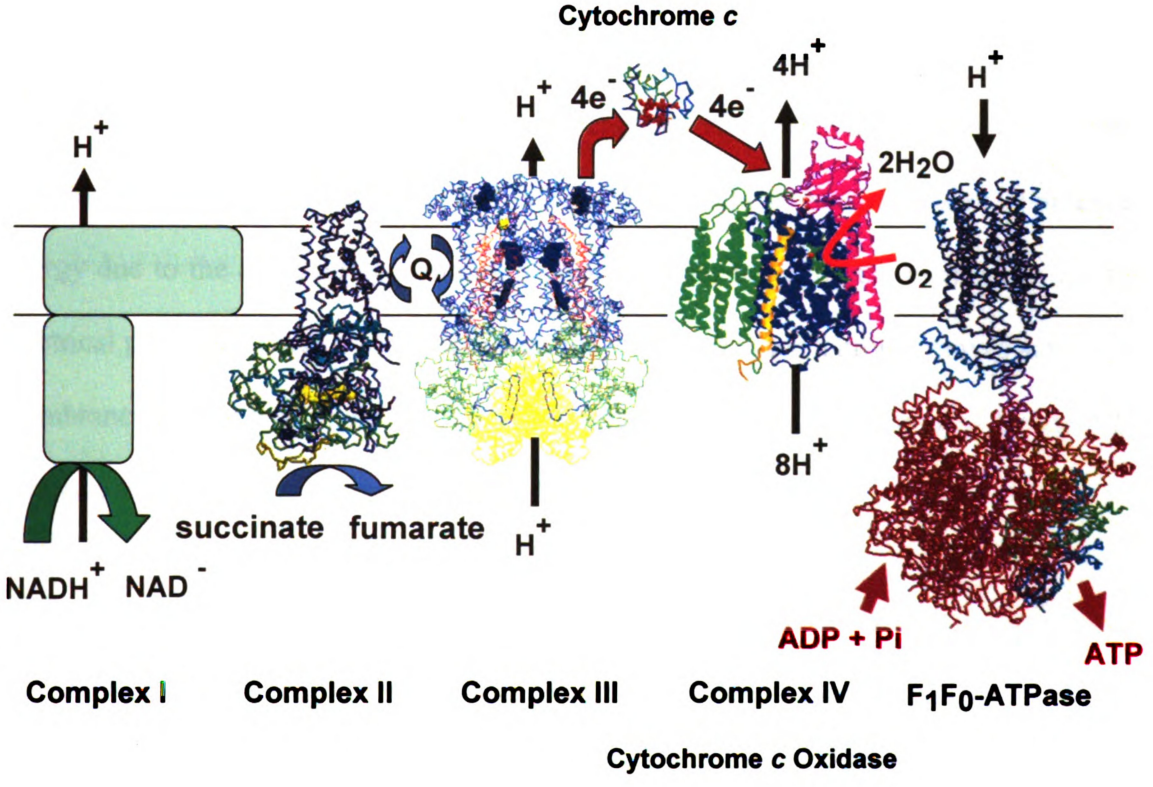

Figure 1. 1: The mitochondrial respiratory chain (Electron Transfer Chain).
The respiratory complexes are located in the innermembrane of mitochondria. Electrons from food sourcesare transferred to Complex I (NADH dehydrogenase) or Complex II (succinate dehydrogenase) through NADH and $FADH_2$, respectively. Then through the coenzyme Q transfers the electrons to complex III (bc1 complex). Cytochrome *c* then transfers the electrons from complex III to complex IV (C*c*O), which was used to reduce dioxygen to form water. Complexes I, III and IV are known to translocate protons across the inner mitochondrial membrane. The proton gradient formed across the inner mitochondrial membrane is then utilized by Complex V (ATP synthase) to generate ATP. (Images in this dissertation are presented in color).

succinate (Yagi et al. 1998; Albracht and Hedderich 2000; Iverson et al. 2000). Complex III (cytochrome bc_1 complex) transfers electrons from ubiquinol to cytochrome *c* (Berry et al. 2000; Darrouzet et al. 2000). Complex IV (cytochrome *c* oxidase, EC 1. 3. 9. 1) ends the sequence by transferring electrons from reduced cytochrome *c* to O_2 (Ferguson-Miller and Babcock 1996). Complexes I, III, and IV couple electron transfer to proton translocation across the membrane from the mitochondrial matrix or bacterial cytoplasm to the intermembrane space. For each pair of electrons transferred through the electron transfer chain to O_2, four protons are pumped out by Complex I, four protons by Complex III, and two protons by Complex IV. The energy stored in such a gradient is called the proton-motive force and consists of two different potential energies: the chemical potential energy due to the different concentration of protons separated by the membrane and the electrical potential energy due to the separation of charge when a proton moves across the membrane without a counter ion. This electrochemical energy is finally used by the ATP synthase to produce the energy currency of living organisms, ATP.

1.2 Cytochrome *c* oxidase and heme-copper oxidase superfamily

As shown in Figure 1.1, cytochrome *c* oxidase (C*c*O) is the terminal enzyme in the respiratory chain. The function of C*c*O is to catalyze the reduction of oxygen to water and pump an additional proton across the membrane for each electron and proton consumed in the reaction. The overall reaction can be expressed as:

$$4\ \text{cyt}\ c^{2+} + 8H^{+}(\text{in}) + O_2 \rightarrow 4\ \text{cyt}\ c^{3+} + 2H_2O + 4H^{+}(\text{out})$$

In this way, a transmembrane electrochemical gradient is produced (Ferguson-Miller and Babcock 1996; Michel et al. 1998).

C*c*O belongs to the heme/copper oxidase superfamily. This superfamily also includes many bacterial heme/copper oxidases, which are defined by the presence of a catalytic core containing the oxygen binding heme a_3 and Cu_B (Garcia-Horsman et al. 1994). The variation in heme/copper oxidases is due to the differences in the active site and proton channels. A- and B-families (Chang et al. 2009) need either an *o* or *a* heme in the active site, both of which have a farnesyl tail, whereas the C-family utilizes *b* heme (with no tail) in the active site (Sharma et al. 2008). The catalytic substrate can either be cytochrome *c* (in the case of C*c*O) or quinol, as in the case of cytochrome bo_3 quinol oxidase from *E.coli*. In *Rhodobacter sphaeroides* (*Rs*), there are three types of C*c*Os: the aa_3 type, the cbb_3 type and the caa_3 type. The most similar form to the mitochondrial C*c*O in *Rs*C*c*O is the aa_3 type. In this thesis, the research is all based on the aa_3 from *Rs*C*c*O.

1.3 Comparison of bovine heart C*c*O and bacterial C*c*O

The position of C*c*O as the terminal member in the respiratory chain defines the importance of this enzyme, which consumes more than 90% of the oxygen we breathe. Historically, bovine heart C*c*O has been the best studied research model, due to the cow heart being both large and a very rich source of mammalian C*c*O.

The X-ray crystal structure of bovine heart C*c*O shows that it can be a dimer in the purified state (Tsukihara et al. 1996). It is a 13-subunit transmembrane complex. The catalytic core subunits (subunit I, II and III) are encoded by the mitochondrial DNA and ten others subunits are encoded by the nuclear genome (Kadenbach et al. 1987). Extensive crystallographic studies have been carried out on the bovine heart C*c*O, including many different forms such as the fully oxidized, fully reduced, azide-bound, cyanide-bound and

carbon monoxide-bound (Yoshikawa et al. 1998). Some structural changes have been observed in the crystal structures of bovine heart C*c*O, revealing possibly important mechanisms for proton uptake. For example, the Asp-51 in subunit I was seen to undergo a conformational change in reduced compared to oxidized crystals. This finding led to the proposal of an additional proton channel for pumping in the mammalian C*c*O, the H-channel, which is not conserved in bacteria. A considerable amount of internal water is also observed in the bovine heart C*c*O, thanks to the high resolution (1.8 Å) crystal structure (Tsukihara et al. 2003). These waters could be involved in the proton pumping mechanism, especially in the D-pathway. The X-ray structure of bovine heart C*c*O also reveals the important role of lipids. In the crystal structure, thirteen lipids, including two cardiolipins, one phosphatidylcholine, three phosphatidylethanolamines, four phosphatidylglycerols and three triglycerides, are identified (Shinzawa-Itoh et al. 2007). These lipids may play a critical role not only in the structural stabilization of the dimer and the whole enzyme, but also in O_2 transfer to the active site and other as yet undetermined functions.

Although the study on bovine heart C*c*O can provide much information and insights on C*c*O, it is extremely difficult to handle when it comes to site-directed mutagenesis for functional and mechanistic analysis, due to the fact that the largest catalytic subunits are encoded in the mitochondrial genome, which has different codons for a number of common amino acids. The bacterial C*c*O, such as *Rs*C*c*O, is a good model system for mechanisic studies because the catalytic core subunits (I and II) are highly homologous to their mammalian counterparts (Figure 1.2) and ease of site-directed mutagenesis and expression in the bacterial system allows the production of numerous mutants to test

functional hypotheses. In *R. sphaeroides*, its ability to obtain energy from photosynthesis, as well as possessing multiple types of C*c*Os besides the aa_3 type, allows the production of C*c*O knock out strains with a clean background for the mutant C*c*O expression.

The bacterial aa_3-type C*c*Os are highly conserved, such as the *Paracoccus denitrificans* and *R. sphaeroides* C*c*Os (sequence similarity: 81% in subunit I, 49% in subunit II, 69% in subunit III, and 48% in subunit IV), and are closely related to the bovine C*c*O (sequence similarity of *Rs* to bovine: 76% in subunit I, 63% in subunit II, 71% in subunit III). The crystal structure of *Rs*C*c*O shows as many as 178 water molecules forming hydrogen-bonded networks inside the enzyme and a high degree of conservation of ordered, hydrogen-bonded water networks in proton pathways, suggesting a critical role of water in proton transfer (Sharpe et al. 2005).

The *Rs*C*c*O crystal structure also shows a total of six phosphatidylethanolamines in the four subunit C*c*O crystal structure (Svensson-Ek et al. 2002), with four positioned on the interface between subunit IV and I/III, and two associated with subunit III and subunit I. The two subunit crystals of *Rs*C*c*O at 2.0 Å resolution, although missing subunits III and IV and the six phospholipids associated with them, revealed the positions of many more lipid /detergent sites that also appear highly conserved in position compared with the bovine and bacterial homologs, including amino acid residues in their vicinity. These findings and those in other crystal structures suggest a specific role of lipid in membrane proteins (Qin et al. 2006) (Figure 1.3).

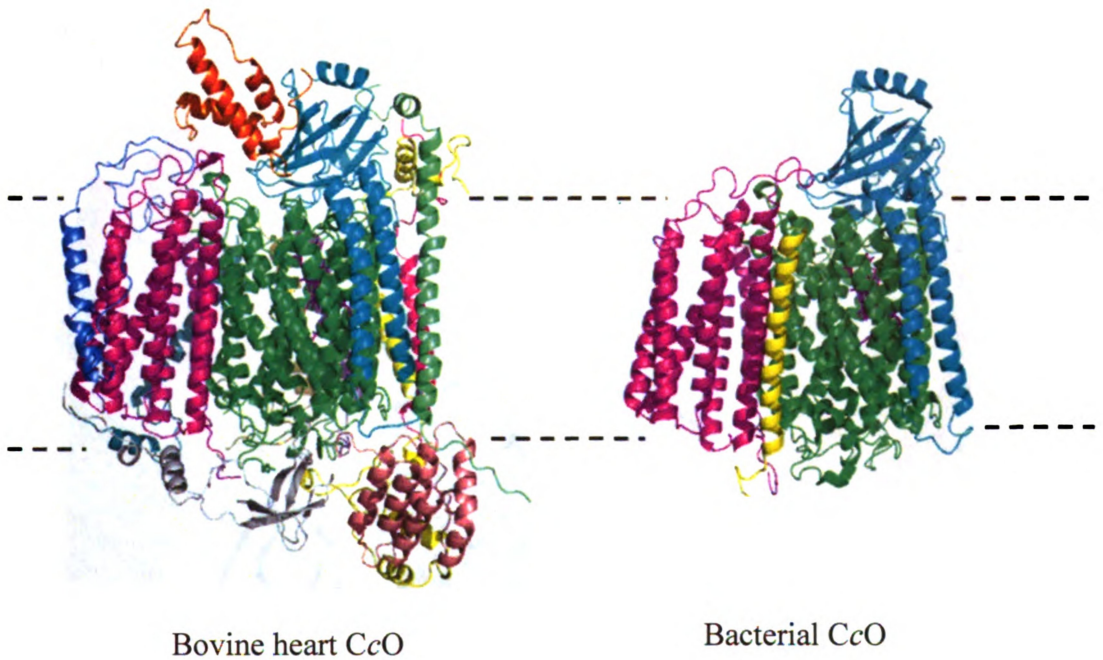

Figure 1. 2: Comparision of bovine heart C*c*O structure and bacterial C*c*O structure. C*c*O from bovine heart contains 13 subunits (left) and the C*c*O from bacteria (*Rs*) contains 4 subunits (right). The dotted lines represent the lipid bilayer membranes. The catalytic core of the bacterial C*c*O, subunit I (green) and subunit II (cyan), is highly homologous to that of the bovine heart C*c*O. The subunit III (purple) is also a conserved subunit.

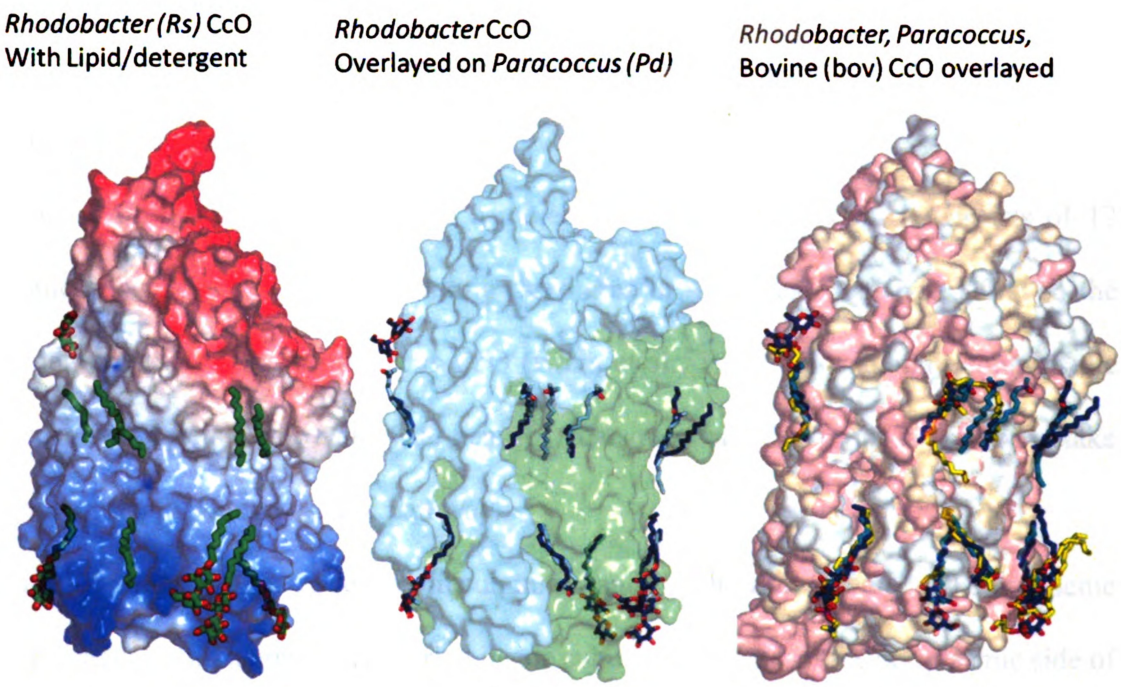

Figure 1. 3: Conserved lipid binding between bovine heart C*c*O and bacterial C*c*O. The lipids/detergent binding sites found in the 2 subunit crystal structures of bacterial C*c*O from different sources (*Rs*, left; *Pd,* middle) are conserved. Comparison of the bacterial C*c*O structure with the bovine heart C*c*O also shows that these lipid binding sites are highly conserved in position (right).The lipids/detergents from *Rs*C*c*O are shown in green (left) and deep blue color (middle and right). The lipids/detergents from *Pd*C*c*O are shown in cyan color (middle and right). The lipid/detergents from bovine heart C*c*O are shown in yellow (right). These results indicate the important role of lipids in the structure and function of C*c*O.

1.4 The structure of *Rs*C*c*O

1.4.1 Overall structure of *Rs*C*c*O

*Rs*C*c*O contains 4 subunits as shown in Figure 1. 4. Subunit I (blue) and subunit II (purple) form the catalytic core of the enzyme, performing both electron transfer and proton uptake/pumping functions.

Subunit I is the largest subunit with a molecular weight of 62 kDa. It consists of 12 transmembrane helices roughly forming three arcs of 4-helices each, noted first in the original structure of the *Paracoccus* C*c*O (Iwata et al., 1995). This subunit contains the redox active centers, heme *a* and Cu_B-heme a_3. It also contains two proposed proton uptake pathways: the D pathway and K pathway.

Figure 1.5 shows the metal centers in subunits I and II. The iron centers of the two heme groups, heme *a* and heme a_3, are buried inside subunit I, 15 Å from the periplasmic side of the membrane. The angle between the two porphyrin rings of the heme *a* and heme a_3 planes is approximately 104° and this angle is quite conserved among the aa_3 oxidases (Sharpe et al. 2005) although its functional significance is not clear. The hydroxyethylfarnesyl tail of heme *a* extends downward and remains in the hydrophobic core between the transmembrane helices while the hydroxyethylfarnesyl tail of heme a_3 bends sideways and penetrates to the lipid bilayer. Heme *a* has a low spin iron with two conserved axial histidine ligands, His102 and His421 in subunit I. Heme a_3 has a high spin iron that is five-coordinated, with only one conserved axial histidine, His419, which is ligated to the iron on the opposite side (distal side) of the heme a_3 to the Cu_B center. The distance between the Cu_B ion and the heme a_3 iron is approximately 4.9 – 5.1 Å in the

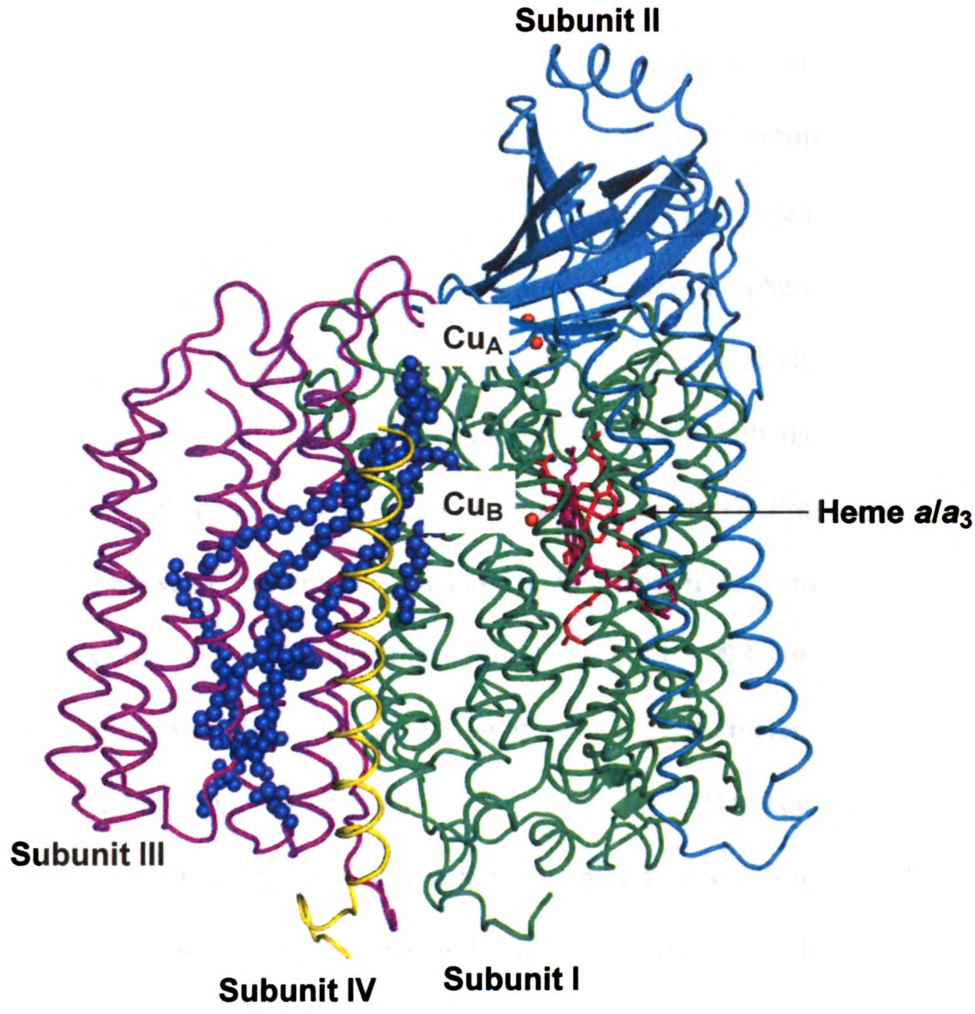

Figure 1. 4: Overall structure of *Rs*C*c*O.
The subunit I (shown in green) contains the Cu_B and heme *a* and heme a_3 (red stick model). Subunit II (cyan) contains the Cu_A. Subunit III is shown in cyan color. Subunit IV is the single helix structure shown in orange color. Between subunit III and subunit IV there are several lipid moles (shown in blue sphere and stick models).

structures of C*c*O from different species (Harrenga and Michel 1999; Svensson-Ek et al. 2002; Tsukihara et al. 2003). In between Cu_B and heme a_3 is the site where oxygen binds and is reduced to water. Cu_B has three ligands, His284, His333, and H334 in subunit I. In high resolution crystal structures, H284 is found to form an unusual covalent bond to Y288 between the $N\varepsilon_2$ and $C\varepsilon_2$ atoms from the two residues, respectively (Ostermeier et al. 1997; Yoshikawa et al. 1998; Buse et al. 1999; Tomson et al. 2002). It has been suggested that this unique linkage between His-Tyr lowers the pKa of the tyrosine phenol group below that of free TyrOH allowing the deprotonated tyrosine radical even at physiological pH. This makes the tyrosine a potential electron and proton donor with the possibility of becoming a neutral radical during catalysis (Ostermeier et al. 1997; Proshlyakov et al. 2000). The density between the heme a_3 iron and Cu_B in the oxidized form of the enzyme has been variously interpreted as a peroxide (Yoshikawa et al. 1998), or one hydroxide bound to the Cu_B and a water ligated to the Fe ion of heme a_3 (Ostermeier et al. 1997).

The molecular weight of subunit II of *Rs*C*c*O is around 32.9 kDa. The N-terminus of subunit II is composed of two transmembrane helices which forms a loop structure while the C-terminus forms an extra-membrane globular domain (Svensson-Ek et al. 2002) which is composed of a ten stranded β–barrel structure. This domain is involved in the binding of cytochrome *c*. Two mixed valance Cu ions form the Cu_A center inside subunit II, which is the initial electron acceptor from soluble cytochrome *c* (Zhen et al. 1999). The ligands for the Cu_A include Cys252, Cys256, His260, His217, and Met263 in subunit II as shown in Figure 1.5.

The two cysteines bridge the two copper atoms from two sides and the two sulfur atoms lie in the same plane as the copper atoms. The importance of this unusual copper center in the

functioning of the protein is not clear; a role in proton pumping has been proposed (Chan and Li 1990), but argued against on the basis of retention of proton pumping in mutants where the structure of the Cu_A center is significantly disrupted (Zhen et al. 2002).

In *Rs*C*c*O, the polypeptide chain of subunit II is known to undergo proteolysis after translation. After the cleavage, the signal peptide (25 residues) on the N-terminus of subunit II is removed (Steinrucke et al. 1987). Besides the N-terminal processing, there is also an incomplete proteolysis of the C-terminal 13 residues (Hiser et al. 2001). The reason for the incomplete C-terminal proteolytic cleavage is still unknown. However, it seems that this cleavage does not affect activity and function of the enzyme (Hosler et al. 1992; Zhen et al. 1998) but does interfere with crystallization due to molecular inhomogeneity.

Subunit III is also around 30 kDa (30.1 kDa). It is composed of seven transmembrane helices and forms a V-shaped cleft between two bundles of helices which appears to be designed to hold four lipid molecules that also interface with subunit I, though only 2 are resolved in the four-subunit structure (Svensson-Ek et al. 2002). The function of subunit III is still unclear. It may play a role in the structural stability of C*c*O. Research has shown that loss of subunit III causes the suicide inactivation of C*c*O (Bratton et al. 1999).

Subunit IV is the smallest subunit (6.3 kDa) with a single transmembrane helix. The function of this subunit is unknown. Deletion of subunit IV of *Rs*C*c*O does not affect the activity in any way that we can detect. The X-ray crystal structure studies, showing four lipids bound to it, indicate that subunit IV is important in lipid binding (Svensson-Ek et al. 2002). In the 2-subunit crystal structure, subunit III and subunit IV are lost during crystallization. However, the structures of subunit I and II are highly similar to those of the 4-subunit crystal structure.

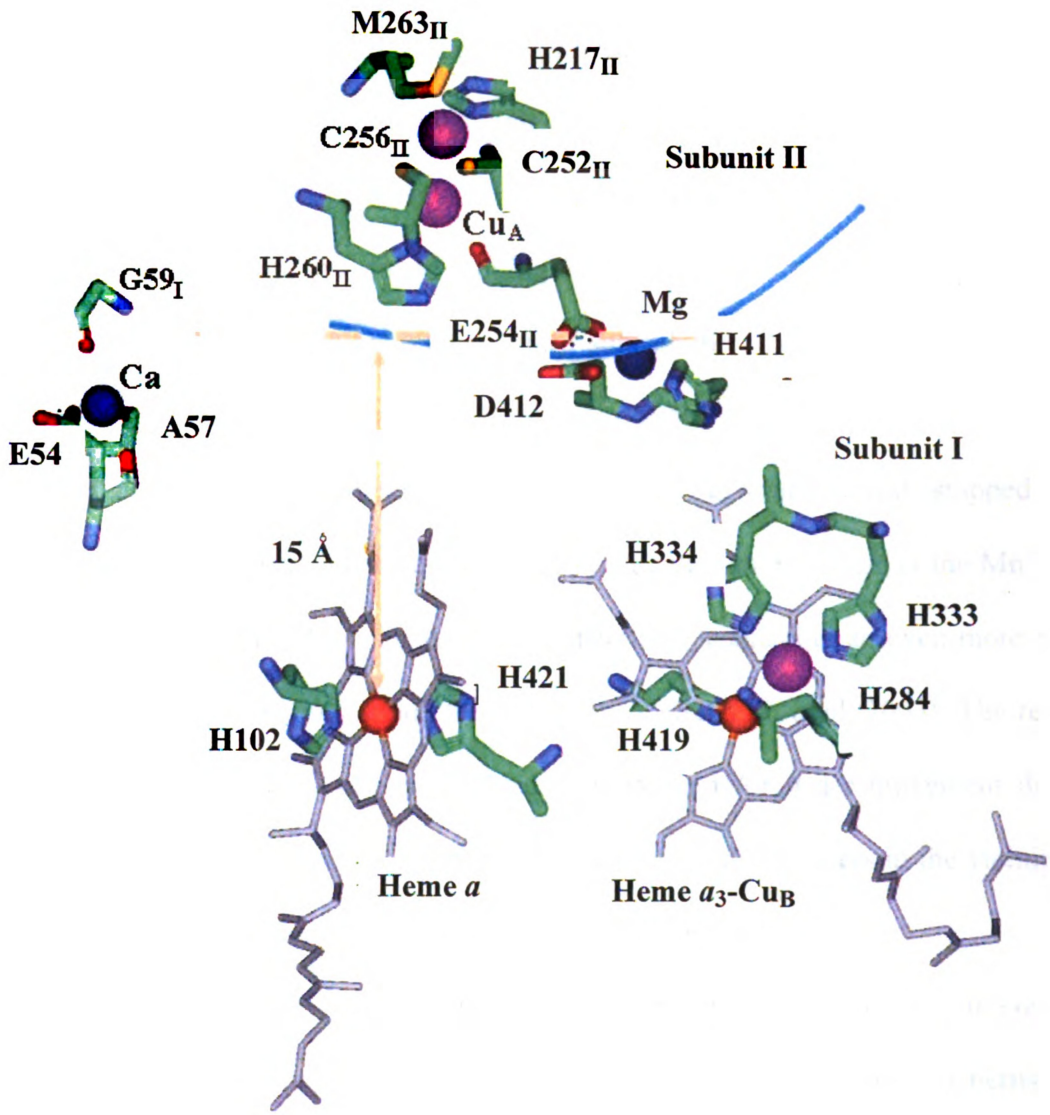

Figure 1. 5: Hemes and metal centers in *Rs*C*c*O and their amino acid ligands.
The heme groups are colored in gray and the amino acid ligands are colored by the atom types (C: green; N: blue ; O: red; S: yellow). Iron, copper, magnesium, and calcium atoms are colored in red, purple, blue and bluish green, respectively. The membrane surface of the periplasmic membrane of *Rhodobacter sphaeroide* is shown as orange dotted line and the interface between subunits I and II is represented by a light blue curve.

1.4.2 Non-redox active metal centers

A non-redox active Mg^{2+} ion is found in between subunit I and subunit II of *Rs*C*c*O, lying at the end of a proposed water channel, approximately 12 Å from the surface and immediately above heme a_3. The liganding residues of this magnesium ion are well conserved, including Asp412, His411 and a shared ligand with Cu_A, Glu254 of subunit II. Three water molecules are also found binding to this magnesium. Its location suggests a role in stabilizing the interface between subunit I and subunit II, or a role in the water exit pathway. The natural Mg^{2+} site can be substituted with Mn^{2+} for EPR studies by growing the bacteria in high manganese. Using D_2O added externally, and stopped-flow freeze-quench EPR measurements, complete proton/deuterium exchange at the Mn^{2+} site was observed in less than 11.4 ms at room temperature, suggesting an even more rapid equilibrium between the Mn site and the bulk solvent (Schmidt et al. 2003). The results suggest that the Mn^{2+}/Mg^{2+} site is involved in proton and/or water movement during turnover. Because of the complex hydrogen-bonding network of waters in the vicinity of Mn^{2+}, it is unclear where exactly water or protons are moving.

The binding of extrinsically added metals, such as Zn^{2+} and Cd^{2+}, to C*c*O is interesting because they inhibit proton movement in many proton-dependent systems (Cherny and DeCoursey 1999). In C*c*O, proton uptake is strongly inhibited by micromolar concentrations of Zn^{2+} or Cd^{2+} (Aagaard et al. 2002; Mills et al. 2002). The inhibition of C*c*O activity by Zn^{2+} or Cd^{2+}, both in the purified detergent-solubilized form and in reconstituted vesicles, suggests both internal and external binding sites (Hosler et al. 2006). A cadmium binding site was clearly identified at the entrance of the K-pathway, involving side chain atoms of E101 and H96 in subunit II, in two subunit isotropic crystals (2.0 Å) of

Rs C*c*O (Qin et al. 2006). This position at the bottom of subunit II had been previously suggested as the entry point for the K-pathway (Branden et al. 2002). Other structures of the bovine C*c*O (Shinzawa-Itoh et al. 2007) show Zn^{2+} binding at the entrance of the D-pathway, as also predicted from kinetic analyses. However, so far there has not been a site defined on the outside surface of C*c*O to account for inhibition by Zn^{2+} of the exit/backflow pathway.

There is also a Ca^{2+}/Na^{+} site found in the *Rs*C*c*O. However, the function of this site is still unknown for *Rs*C*c*O. In bovine heart C*c*O, the binding of the $Ca^{2+}$to the site that appears normally occupied with Na^{+} causes a heme *a* red shift (Nicholls 1975; Wikstrom and Saari 1975).

1.5 Electron sources and pathways

The electron transfer pathway in *Rs*C*c*O is quite clear now. The electrons are first transferred from cytochrome *c* to the Cu_A center, and then to heme *a*, finally to the binuclear center, Cu_B and heme a_3, where O_2 binds and is reduced to water (Ferguson-Miller and Babcock 1996; Michel et al. 1998).

In *R. sphaeroides*, there are two types of cytochrome *c* that have been considered as the substrates for C*c*O: cytochrome c_2, which is a soluble, mobile molecule, and cytochrome c_y, which is a membrane-anchored protein. Research results show that the latter one is the more likely physiological electron donor for the aa_3-type C*c*O in *R. sphaeroides* (Daldal et al. 2001; Daldal et al. 2003). However, for experimental purposes the soluble horse heart cytochrome *c* serves as an excellent substrate for *Rs*C*c*O. From molecular modeling using horse heart cytochrome *c*, the binding site for cytochrome *c* is proposed to be on the outside

of the membrane on a concave surface created by the globular domain of subunit II and the adjacent flat surface of subunit I (Roberts and Pique 1999; Flock and Helms 2002; Maneg et al. 2004).

Protein docking studies (Roberts and Pique 1999) and chemical modification studies (Ferguson-Miller et al. 1978) along with intensive site-directed mutagenesis analysis (Ferguson-Miller et al. 1978; Roberts and Pique 1999; Wang et al. 1999; Zhen et al. 1999) showed that the binding of cytochrome *c* to the oxidase is mainly through electrostatic interactions between the two docking faces. Five lysine residues on cytochrome *c,* Lys8, Lys13, Lys72 and Lys86/87 (horse heart cytochrome *c* numbering), form an interaction with the Glu148, Glu157, Asp195 and Asp214 residues of subunit II of C*c*O (Ferguson-Miller et al. 1978; Roberts and Pique 1999; Wang et al. 1999; Zhen et al. 1999). Research results also show that a conserved Trp143 on subunit II could be the immediate electron acceptor from reduced cytochrome *c* (Witt et al. 1998; Roberts and Pique 1999; Wang et al. 1999; Zhen et al. 1999). Mutation of W143 decreased the electron transfer rate to Cu_A by close to 1000-fold without affecting the binding of cytochrome *c* to C*c*O (Wang et al. 1999; Zhen et al. 1999). The Cu_A site, composed of two mixed-valence copper ions, is located in the extramembrane domain of subunit II. The electron transfer rate from Cu_A to heme *a* is very fast (2.3×10^4 s^{-1} in bovine heart mitochondrial C*c*O (Pan et al. 1993) and 9×10^4 s^{-1} in *Rs*C*c*O (Wang et al. 1999)). Two major electron transfer (tunneling) pathways between the Cu_A site and heme *a* have been proposed. One of the pathways starts at the ligand (Cys252). Along this pathway, 26 covalent bonds and 2 hydrogen bonds and one through space jumping are involved. However, results showed that for this pathway the electron transfer rate would be much slower than the measured rate.

The other pathway starts with a hydrogen bond between the Cu_A ligand His260 in subunit II, which bonds to a carbonyl group of the peptide bond between two highly conserved arginine residues Arg481 and Arg482 in subunit I, and then through Arg482 to one of the propionate groups in heme *a*. This pathway is composed of 14 covalent bonds and two hydrogen bonds (Iwata et al. 1995; Ramirez et al. 1995; Regan et al. 1998; Tan et al. 2004). The importance of the residues along the pathway is supported by the site-directed mutants H260N and R482P, which showed an approximately 2000 fold slower electron transfer rate between Cu_A and heme *a* (Wang et al. 2002; Zhen et al. 2002; Qian et al. 2004).

These results can be used to support the concept of a "through bond" pathway of electron transfer. Although the distance between Cu_A and the heme a_3 is only about 1.5 Å longer than that between Cu_A and heme *a*, evidence for significant rates of electron transfer between Cu_A and the heme a_3-Cu_B binuclear center has not been found (Regan et al. 1998). There are two possible electron transport pathways between heme *a* and heme a_3. The electrons could either be transported through the closely approaching heme edges, or the histidine ligands to each heme connected through helix X (Regan et al. 1998). The direct electron transfer between the two heme porphyrin rings would occur through "edge to edge" transfer since the closest edge to edge distance between the two heme groups is only approximately 4.6 – 5.2 Å in C*c*O from different organisms (Ostermeier et al. 1997; Harrenga and Michel 1999; Svensson-Ek et al. 2002; Tsukihara et al. 2003; Tan et al. 2004). The center-to-center transfer via the histidine ligands involves some through space jumps and a distance of approximately 13.5 Å between the two heme Fe atoms.

1.6 Proton uptake channels: D- pathway and K- pathway

In each catalytic cycle, four protons are taken up from the inner side of the membrane to react O_2 and produce water; four other protons are taken up from the inside to be pumped to the outside of the membrane against the membrane potential and pH gradient (electrochemical gradient)(Ferguson-Miller and Babcock 1996; Michel 1998; Schultz and Chan 2001; Mills and Ferguson-Miller 2003). Two possible proton uptake pathways, D and K pathways have been proposed in *Rs*C*c*O as shown in Figure 1.8 (Iwata et al. 1995; Wikstrom et al. 2000; Svensson-Ek et al. 2002) .

1.6.1 The D proton pathway

The D pathway was named after a conserved aspartate residue Asp132, which is located on the inner surface of subunit I and is considered to be the entrance of the D pathway because of its dramatic inhibition of activity when mutated and its location close to the start of a hydrogen bonded chain of waters leading toward the active site. The chain of waters is organized by a series of hydrophilic residues including N121, N139, N207, S142, Y33, S201, S200, and ending at E286 near the Cu_B-heme a_3 binuclear center. Changes to these residues have marked effects on enzyme activity and the proton pumping, in some case inhibiting and in others uncoupling the proton pump (that is, allowing activity without proton pumping).

In the crystal structure of *Rs*C*c*O, the chain of water molecules is very well defined in this pathway (Svensson-Ek et al. 2002; Qin et al. 2006). The importance of the ordered water in the function and kinetics of this pathway are still being studied. Computational and experimental results suggest that the side chain of E286, at the interior end of the pathway close to the hemes, might be a regulatory "switch control," undergoing a conformational

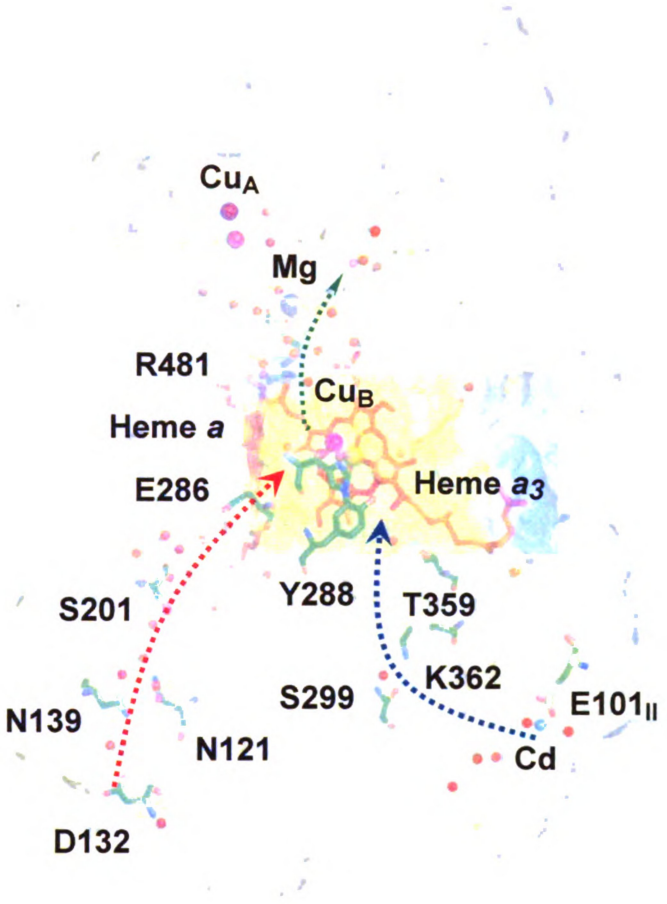

Figure 1. 6: Proton uptake pathways in *Rs*C*c*O.
The subunit I is shown in yellow color and the subunit II is in blue color. Red dotted line and the blue dotted line are the D-pathway and K-pathway respectively. The water molecules in the structure are shown in red spheres. The green dotted line is a proposed water/proton exit pathway.

change that directs a D-path proton to either the active site Cu_B-heme a_3 or to the exit pathway to be pumped out (Konstantinov et al. 1997; Hofacker and Schulten 1998);(Sharpe et al. 2005). The proton transfer pathway after E286 is still unclear. However, a reduced crystal structure of *Rs*C*c*O shows the disappearance of one water, W301, between E286 and heme a_3 upon reduction that could break the connection of the D-path to the active site. At the same time, reduction leads to the rearrangement of the water molecules below the Cu_B-heme a_3 site, suggesting increased water access from the K path and thus a possible alternating gating mechanism (Qin et al. 2009) .

1.6.2 The K-pathway.

The K pathway was named after a conserved lysine, K362 of subunit I, which has a profound effect on activity (<0.02% WT) and was predicted (and found) to be in the middle of a conserved transmembrane region. This region does not show an organized water chain, but does lead to the active site, and MD calculations predict that water can organize in it. The K-pathway in *Rs*C*c*O appears to start with a glutamate residue E101 in subunit II, and continues through S299, K362 and T359 in subunit I, up to the binuclear center, where molecular oxygen is reduced to water (Braenden et al. 2002; Tomson et al. 2003) . This pathway ends with a tight (2.6 Å) hydrogen bond between the hydroxyl group of Y288 and the carboxyl group from the farnesyl tail of heme a_3. There is also a water associated with this bond and with T359 at the top of this channel. The K pathway is believed to transport substrate protons to the active site. Mutation of the K362 to methionine shows extremely low activity. Mutations of S299 and T359 strongly inhibit the activity as well. Unlike the D132A C*c*O, whose activity can be stimulated by the presence of a transmembrane potential, the K362M mutant does not show an increase of the activity with

the membrane potential (Fetter et al. 1995; Mills et al. 2000). This lack of enhancement of activity in the K path mutants suggests that the K pathway is not connected to the external surface via any reversible proton path and is exclusively used for substrate proton uptake. Yet it remains unclear which and how many of the four required substrate protons are supplied by each pathway, and when and how these protons are used in the oxygen reduction reaction, a central issue in understanding the coupling of proton pumping and electron transfer.

1.6.3 The H proton pathway in bovine heart C*c*O

In bovine heart C*c*O, an H pathway is proposed in addition to the D and K pathways, based on the high-resolution crystal structure (Tsukihara et al. 1996; Yoshikawa et al. 1998). This pathway connects the mitochondrial matrix side of the membrane to the outside via water pools and residues in close proximity to heme *a*. It is postulated to be an exclusive pathway for the pumped protons in mammalian C*c*O, due to there being little or no conservation of the residues involved in the bacterial enzymes. Indeed, mutagenesis results show that some of the essential residues along this pathway had no effect on the bacterial C*c*Os, indicating that the H pathway is not likely to be a universal proton uptake pathway (Lee et al. 2000).

1.7 Oxygen pathway in C*c*O

Because of the nonpolar character of the O_2 molecule, it is more concentrated in the membrane than in aqueous solution and could simply reach the active site through diffusion from the membrane into the hydrophobic regions of the protein. However, three specific oxygen pathways were proposed in the bovine enzyme based on hydrophobic channels in the crystal structure (Tsukihara et al. 1996). In one of them, which is supported

by molecular dynamics studies, oxygen would reach the binuclear center through a hydrophobic hole leading from the V-shaped cleft formed by helices of subunit III through subunit I to the binuclear center active site (Hofacker and Schulten 1998). Based on the positions of the xenon atoms resolved in the structure of *Rs*C*c*O crystal pre-pressurized with xenon, an alternative oxygen pathway was proposed which accessed the binuclear center through subunit I between two other transmembrane helices (Svensson-Ek et al. 2002).

1.8 The water/proton exit pathway(s)

In *Rs*C*c*O there is another channel-like structure at the interface of subunit I and subunit II. This channel is considered to be a possible water/proton exit channel. It starts from the binuclear center and continues up via the magnesium center to the outside of the membrane. The non-redox-active Mg appears to be a control point in this channel. The octahedral coordination of this metal center has 3 amino acid residues and 3 waters as its ligands (Tsukihara et al. 1996; Svensson-Ek et al. 2002). Furthermore, in the *Rs*C*c*O crystal structure, water molecules are found around this region. Experiments using ^{18}O isotopes of oxygen and water show that water produced at the catalytic site binds to the Mg^{2+}/Mn^{2+} (Schmidt et al. 2003). The evidence indicates that the Mg^{2+} could be a part of water/proton exit channel for the product released during the reaction catalysis. The results also suggested that the water produced at the active site exits by a discrete pathway rather than by random diffusion.

One possibility for the proton exit is that protons transported through the D pathway are picked up by E286. Via conformational movement of E286 and new water chain formation,

protons could be moved to the vicinity of the D-ring propionate group of heme a_3 (Hofacker and Schulten 1998; Cukier 2004). The latter is connected to the exterior through several hydrogen-bonded water networks. However, it is not yet clear whether there is a specific proton exit path, and if so, where.

1.9 Reaction cycle of *Rs*C*c*O

Spectroscopic and fast kinetic measurements have contributed to our understanding of the chemistry involved in O_2 reduction as shown in Figure 1.7 (Michel et al. 1998; Zaslavsky and Gennis 2000; Kim et al. 2004). The reaction cycle could start from the oxidized form of *Rs*C*c*O (intermediate O), which has hydroxyls bound to both heme a_3 and Cu_B. The first two electrons and protons that enter C*c*O are expected to go to Cu_B and heme a_3 of the binuclear center, causing reduction of these two centers and the conversion of their bound hydroxyls to water (intermediate R). An oxygen can then bind to the reduced binuclear center. The oxygen bond is rapidly cleaved by a four electron transfer event, using two electrons from the heme a_3 to form a ferryl-oxo and one electron from Cu_B to form a cuprous hydroxide, as well as an electron and proton from a nearby Tyr288 (MacMillan et al. 1999). Intermediate P (peroxy) is formed in this step. Then a third electron and proton are injected which likely reduce the Tyr288 free radical back to its stable state, forming intermediate F. Finally, a fourth electron is injected with an accompanying proton to convert the *Rs*C*c*O from the Fe^{4+} ferryl intermediate to its Fe^{3+} oxidized state, with hydroxyls on both heme a_3 and Cu_B. Some research results suggested that the proton pumping occurs during the oxygen reduction cycle (Vygodina et al. 1997), in the P $\rightarrow$ F and F $\rightarrow$ O steps. Others proposed that one proton is likely to have been transferred before

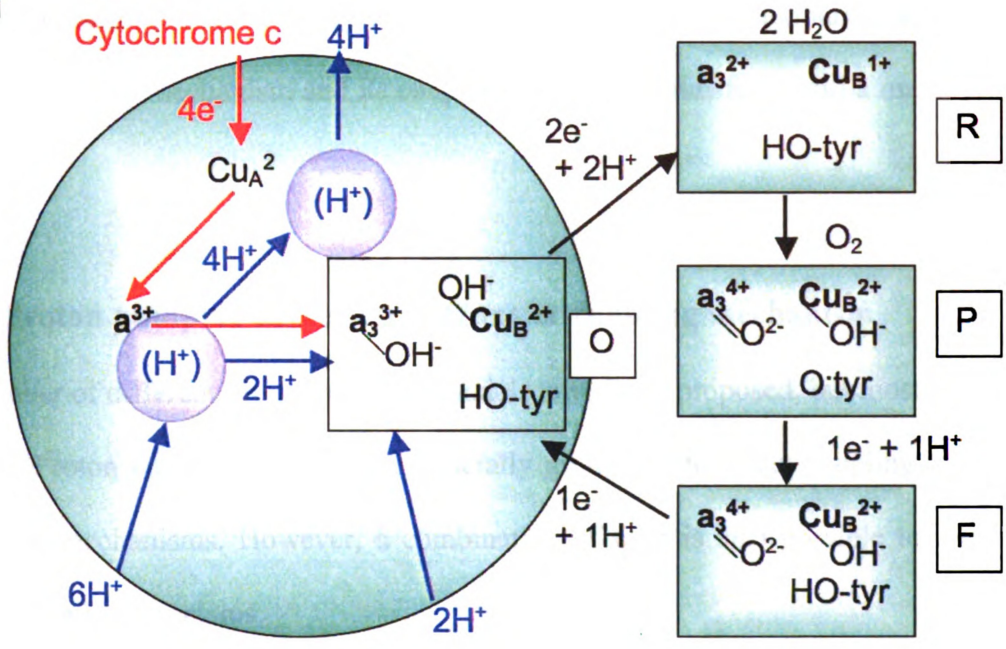

Figure 1. 7: Reaction cycle of *Rs*C*c*O The green circle is the C*c*O.
The red arrows are the electron transfer pathways in *Rs*C*c*O, the blue arrows are the proton uptake pathways. The boxes show the reaction intermediates in the oxygen reduction chemistry. O, oxidized; R, reduced; P, peroxy; F, ferryl. The purple circles indicate proton loading sites during transfer to the active site or to the outside.

the formation of the P intermediate. (Michel 1999). The proton pumping could also occur during each one-electron step of reduction of the enzyme (Sharpe and Ferguson-Miller 2008; Stuchebrukov 2007; (Wikstrom and Verkhovsky 2002; Tsukihara et al. 2003). The proton pumping mechanism and its coupling to electron transfer is still a major unsolved problem.

1.10 Proton pumping and electron transfer coupling mechanism

A number of different proton pumping models have been proposed, but most are difficult to test. Proton pumping theories are generally grouped into direct coupling and indirect coupling mechanisms. However, a combination of both is also possible to explain the complicated mechanisms.

In the direct coupling mechanism, the protons are bound and released by the metal centers or their direct ligands in response to changes in redox state. Since in the case of C*c*O there are two different types of protons involved, two separate proton uptake pathways can be proposed to bring the protons to the active site, one for substrate protons and one for protons to be pumped. One example of direct coupling is the ligand exchange model first proposed by Chan and colleagues. In this model, a redox-active metal center, Cu_A, could drive the proton pump by undergoing ligand exchange, where the protonation state of the ligand changes. However, later experimental results showed that Cu_A, the redox center they proposed in the model, is not crucial for proton pumping (Zhen et al. 2002). Another example of a direct coupling mechanism that involves changes at the active site, is the histidine cycle model proposed first by Wikstrom and colleagues (Wikstrom et al. 1994). In this model, H290 (*Rs* number: H333) is proposed to cycle between imidazolium and

imidazolate states, so that two protons could be pumped in each of two cycles. First, H290 in the imidazolate form binds to the oxidized Cu_B. Then after reduction, a negatively charged oxygen intermediate binds to heme a_3. To balance the negative charge, two pumped protons are taken up from the matrix side and H290 goes back to the imidazolium state and dissociates from the Cu_B. At this point, two substrate protons are taken up and one water is formed. Since the electrostatic stabilization is no longer needed, the two pumped protons are released to the other side of the membrane, and H290 binds to the Cu_B again. The balance of electrostatics at the binuclear center is the key in the model.

In a recently proposed model from our research group (Sharpe et al. 2005), the covalently bound H284–Y288 pair is suggested to go through cycles of ligation and de-ligation from Cu_B in response to changes in charge and ligand state of the Cu_B. The rotation of its imidazole-tyrosine rings leads to alternate opening and closing of the K pathway by breaking or reforming the tight hydrogen bond between the tyr –OH and the farnesyl-OH. Therefore, protons can move into the active site alternately from the D and K pathways, depending on the Cu_B ligation state and the charge present in the binuclear center. Protons are transported either to the active site to form water or to a conserved water molecule bound between the propionates of heme a_3, via the histidine 334 ligand of Cu_B. The latter proton is released to the outside of the membrane. This is a new version of the histidine cycle model which fits with the conformational changes seen in the *Rs*C*c*O crystal structure upon reduction (Qin et al, 2009) but remains to be tested by other approaches.

In the indirect coupling mechanism, a long-range protein-mediated coupling is required between redox changes at the active site and conformational changes at a distance that lead to proton uptake and release. One example of the indirect coupling model was proposed by

Yoshikawa's group (Yoshikawa et al. 1998). Based on their high resolution X-ray crystal structures of oxidized and reduced bovine heart C*c*O, residue D51 in subunit I (bovine numbering) at the top of the proposed H channel was suggested to be involved in proton pumping. The loop between subunit I helix I and helix II, including D51, is seen to be the main region of the enzyme undergoing a conformational change. In the oxidized state of enzyme, D51 is buried under the protein surface and connected to the matrix side via a hydrogen bonded network and internal water pools. Its conformation changes upon reduction of the C*c*O, leading to exposure of its protonated carboxyl to the intermembrane surface, a p*K* change and proton release (Yoshikawa et al. 1998). This proton pumping mechanism bypasses the binuclear center and is proposed to be driven by heme *a* redox changes (Tsukihara et al. 2003). However, the residue D51 is not conserved in bacterial enzymes, so the model cannot easily be generalized. Nor is it readily testable, since mutant forms of the bovine C*c*O are difficult to produce and test in the purified state.

1.11 The Regulation of C*c*O

C*c*O is the fourth and final complex in the respiratory chain and therefore plays a critical role in regulating the rate and efficiency of the whole energy transduction process, which impacts in turn on many physiological processes. Thus the control of C*c*O activity is crucial, but there are no established mechanisms for how this is accomplished.

Nucleotides have been found to have regulatory effects on the C*c*O. In the crystal structure of bovine heart C*c*O two binding sites that were occupied by cholate molecules were observed and postulated to be actual binding sites for nucleotides (Shinzawa-Itoh et al.

2007). A deoxycholate binding site is also found in a similar position in the *Rs*C*c*O crystal structure, suggesting conservation and an important role for this site (Qin et al. 2008).

The activity of C*c*O is observed to be affected by a variety of factors, such as fatty acids (Sharpe et al. 1996), thyroid hormones (Kadenbach and Arnold 2000), zinc ions (Mills et al. 2002), nitric oxide (Antunes et al. 2004), and by the direct energy indicator, the ATP/ADP ratio (Kadenbach 1986; Beauvoit and Rigoulet 2001). The proton pumping efficiency of C*c*O is also regulated by changes in the membrane potential. Evidence suggests that in C*c*O there is a proton backflow pathway that allows protons to be taken up from the outside to support oxygen reduction activity in the presence of a membrane potential, decreasing the proton pumping efficiency (Mills et al. 2002). Zinc inhibition of C*c*O reconstituted into lipid vesicles in the presence of a membrane potential is concluded to be due to the blockage of the proton exit/backflow (Mills et al. 2002). In spite of these many possibilities, little conclusive evidence is available to provide a meaningful picture of how the activity and efficiency of C*c*O is regulated under physiological conditions.

2. Membrane Protein Crystallography

To further understand the functional and regulatory mechanisms of the proteins, acquiring atomic-resolution structural information has become more and more important. Solving X-ray crystallographic structures is a widely used technique in the biological science field. In comparison, the nearest competing method in terms of structural analysis is nuclear magnetic resonance (NMR) spectroscopy. However, the solution-state NMR is restricted to relatively small proteins while X-ray crystallography can solve the detailed structures of relatively large proteins and membrane proteins.

The results from X-ray crystallography of C*c*O from difference sources have already provided us with a better understanding of the structure and functional relationships in this enzyme. However, there are still many questions remaining in C*c*O research, such as the underlying mechanism of the vectorial translocation of protons and how proton pumping is coordinated with electron transfer and oxygen reduction. Recent structures of *Rs*C*c*O show that not only the protein residue conformation but also the water molecules in the structure are important for the function (Qin et al. 2006; Qin et al. 2009). To resolve these issues, more high resolution crystal structures of C*c*O are still needed. Unfortunately, C*c*O is a large multiple-subunit transmembrane complex and high resolution X-ray crystallography of membrane proteins has always been a challenge in the structure biology.

2.1 Challenges in membrane protein crystallography

The first problem facing membrane protein crystallography is the expression and purification of the protein. To get crystals of the protein of interest, significant amounts of protein are required. Many membrane proteins exist at very low levels in the membranes natively. The over-expression of a membrane protein in the usual system, such as *E. coli*, often causes the protein to aggregate and be improperly posttranslationally modified.

Therefore, finding a good expression system is a very important step for the membrane protein crystallography. *R sphaeroides*, a gram-negative bacterium with an abundant membrane system, has been proved to be a good expression host not only for C*c*O (Zhen et al. 1998), but also for various membrane proteins (Wadhams et al. 2000).

Some evidence also shows that the lipid content in the membrane could also be critical for the expression and correct folding of the membrane proteins (Dowhan et al. 2004). In order

to extract a membrane protein from the lipid bilayer into solution, detergents are added to solubilize the protein. In this step, the lipid environment of the membrane protein is changed by the replacement of the lipids with detergent molecules. This usually makes the protein less stable and may lead to loss of its native conformation. Thus choosing the right detergent is very important in the crystallization of a membrane protein (le Maire et al. 2000; Garavito and Ferguson-Miller 2001; Gohon and Popot 2003). There are three classes of detergents: ionic, nonionic, and zwitteronic, named after the biochemical features of their head groups. The nonionic detergents with sugar-based head groups, such as alkyl maltosides (Rosevear et al. 1980) are often used in membrane protein purification and crystallization since less denaturing effects on membrane proteins are observed. In our case, decyl maltoside and dodecyl maltoside were used in the solublization and crystallization of *Rs*C*c*O (Qin et al. 2006). Zwitterionic detergents such as LDAO have also been used in several successful membrane crystallization experiments (McLuskey et al. 2001). However, there are no universal standards for which detergent is the best candidate for a particular membrane protein. Successful crystallization of membrane proteins usually requires large amounts of screening for the best detergent.

Another obstacle for membrane protein crystallization is the lack of proper crystal contacts for the crystallization. Membrane proteins usually have a large hydrophobic/ amphiphilic surface covered by lipids and detergents. Unlike soluble proteins, their surface lacks the hydrophilic residues which can form good ionic interactions during crystallization. Good crystals that can diffract to high resolution under X-rays usually have a well ordered formation in the crystal unit cells. The hydrophobic character of the membrane protein surface favors non-specific interactions and often causes the protein to precipitate and

denature. This is one of the reasons why the right detergent is very crucial in the crystallization of membrane proteins.

2.2 Progress in membrane protein crystallization

Despite the difficulties of getting membrane protein crystals, considerable progress has been made since the first reported crystal structure more than 20 years ago (Michel 1982). For example, high resolution crystal structures have been solved for C*c*O from various sources (Iwata et al. 1995; Tsukihara et al. 1995; Tsukihara et al. 1996; Ostermeier et al. 1997; Svensson-Ek et al. 2002; Qin et al. 2006; Qin et al. 2009). Other than high throughput screening of crystallization conditions, and availability of a variety of pure detergents and crystallization additives, other approaches have been used to overcome the difficulty of membrane protein crystallization. These approaches include micro- and macro-seeding (Fromme and Witt 1998), semi-directed mutagenesis of selected surface residues (Pautsch et al. 1999) and crystal dehydration (Kuo et al. 2003). Besides the conventional crystallization methods, several new techniques involving use of lipids and adding protein domains have been developed to aid in membrane protein crystallization.

2.2.1 Crystallization of membrane proteins in lipid cubic phase

The lipid cubic phase methods were first developed in hope of maintaining the native environment of the protein including the lateral pressure exerted by lipid bilayers and minimizing the disturbance and disordering of the membrane protein. In this method, a continuous membrane formed by mixing lipids and water is used as a support matrix for nucleation and crystal growth. Since membrane proteins tend to be less stable when they are extracted from native membranes and incorporated into detergent micelles,

crystallizing membrane proteins in a quasi-solid membrane environment throughout the crystallization process seems to have an advantage. The first successful case for lipid cubic phase crystallization was the application to bacteriorhodopsin (Landau and Rosenbusch 1996). Later results showed that this method was very successful in a class of membrane proteins with seven transmembrane helices including bacteriorhodopsin (Landau and Rosenbusch 1996; Luecke et al. 1999), halorhodopsin (Kolbe et al. 2000), and sensory rhodopsin II (Gordeliy et al. 2002).

2.2.2 Antibody assisted membrane protein crystallization

One of the main reasons membrane proteins are difficult to crystallize is their lack of hydrophilic residues on the protein surface, which are important in forming crystal contacts between molecules. Adding certain peptides or proteins, such as an antibody, could extend the hydrophilic portion of the membrane protein, thus favoring more crystal contacts. In the crystal structure of the four subunit cytochrome *c* oxidase from *Paracoccus denitrificans (Pd)*, all crystal contacts were found between attached antibody molecules (Iwata et al. 1995). The antibody assisted crystallization also succeeded in the crystallization of the two subunit *Pd*CcO (Ostermeier et al. 1997), yeast cytochrome bc_1 complex (Hunte et al. 2000), and the KcsA K^+ channel (Zhou et al. 2001).

2.2.3 Fusion protein strategy to assist membrane protein crystallization

Another way of increasing the hydrophilic portion of a membrane protein is fusion to a soluble protein. One example of this method is the crystallization of *E. coli* cytochrome bo_3 ubiquinol oxidase, in which case a small peptide (peptide Z) was engineered into the membrane protein with the hope of forming crystal contacts (Byrne et al. 2000). However, the fusion protein approach did not produced well-diffracting crystals yet, presumably

because of the flexible nature of the linker region. One successful case of the fusion protein strategy is the solving of the first crystal structure of human β_2-adrenergic G protein-coupled receptor (GPCR) (Cherezov et al. 2007). In this case, Cherezov et al. removed the flexible loop of the GPCR and inserted a T4-lysozyme by molecular engineering. Combined with the cubic phase method, the fusion protein was crystallized and diffracted to 2.4 Å. The widely-used bio-fluorescent marker protein, green fluorescent protein (GFP), could also be used in the fusion protein strategy. The highly soluble, compact structure of the GFP makes it a good candidate in the crystallization of various proteins (Hakansson and Winther 2007; Suzuki et al. 2010).

3. Background of Green Fluorescent Protein

The green fluorescent protein (GFP, as shown in Figure 1.8) is a spontaneously fluorescent soluble protein isolated from the jellyfish, *Aequoria victoria* (Shimomura et al. 1962; Ormo et al. 1996; Tsien 1998). Its natural role is to transduce the blue chemiluminescence of aequorin into green fluorescent light by energy transfer (reference). However, the purpose of both bioluminescence and GFP fluorescence in jellyfish is unknown. The structure and fluorescent mechanisms of GFP have been well studied since it was first found by Shimomura et al in 1960 (Shimomura et al. 1962). GFP has become a good expression marker that is widely used in life science research. Roger Tsien, Martin Chalfie and Osamu Shimomura were awarded the 2008 Nobel Prize in chemistry for their discovery and the development of the GFP.

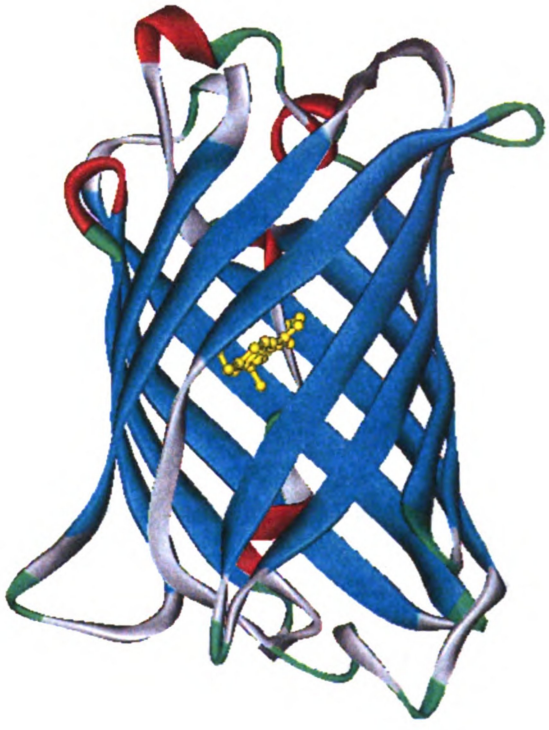

Figure 1. 8: Structure of Green Fluorescent Protein.
GFP is composed of 11 β-sheets and 4 α-helices. The chromophore (yellow colored structure) is buried inside this β-sheet barrel structure. This figure is created by ViewLite software with coordinates from PDB file 1EMC.

3.1 Structure of GFP

WT GFP is composed of 238 amino acid residues (MW 26.9 kDa). It has a typical beta barrel structure, consisting of 11 β-sheets with one alpha helix structure containing the chromophore in the center (Ormoe et al. 1996). The chromophore of GFP is a *p*-hydroxybenzylideneimidazolinone. The side chains of the barrel face inward and induce specific cyclization reactions in the conserved tripeptide Ser65–Tyr66–Gly67 that lead to chromophore formation. Figure 1.9 shows the current proposed mechanism for chromophore formation (Heim et al. 1994; Cubitt et al. 1995). GFP first folds into a near-native conformation, then the nucleophilic attack of the amide of Gly67 on the carbonyl of Ser65 forms the imidazolinone structure. After a dehydration reaction, molecular oxygen dehydrogenates the α–β bond of residue 66 to put its aromatic group into conjugation with the imidazolinone. This process is not dependent on other proteins or special cofactors except oxygen. The formation of the chromophore does not happen in obligate anaerobes. Oxygen has no further effect after the formation of the chromophore (Swaminathan et al. 1997) .

3.2 GFP derivatives

The hydrogen bonding network and electron stacking interactions with side chains near the chromophore influence the fluorescent properties of GFP. Therefore many different mutants of GFP have been engineered for the potential of widespread usage and the evolving needs of researchers. A single mutant (S65T) reported in 1995 in *Nature* by Roger Tsien was the first major improvement on WT GFP. It greatly improved the spectral characteristics of GFP, resulting in increased fluorescence and photostability. The major

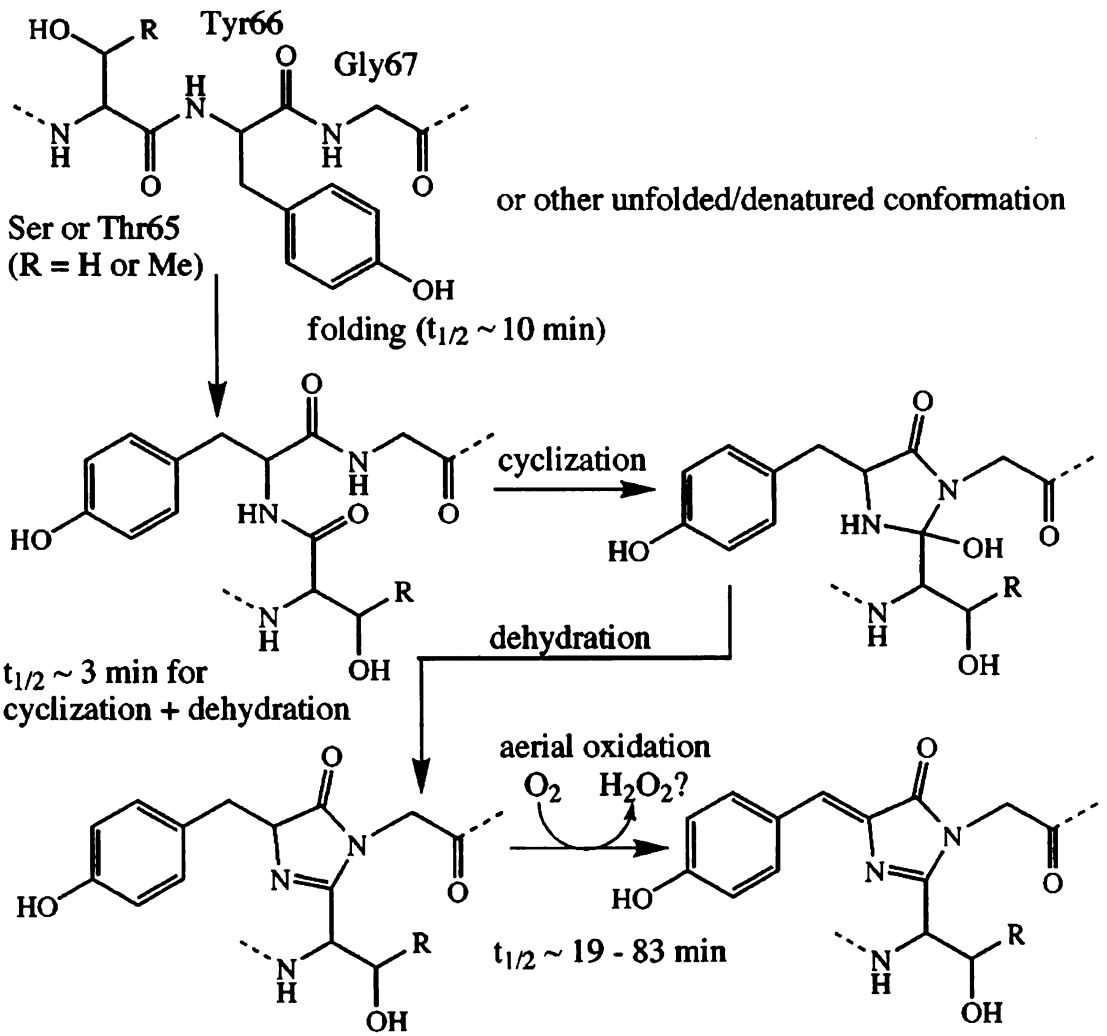

Figure 1. 9: A proposed mechanism of the formation of the chromosphere of GFP. In this mechanism (Heim et al. 1994; Cubitt et al. 1995), the formation of the chromophore is a self-catalyzed reaction and does not require other protein factors.

excitation peak of this mutant is 488 nm and the peak emission stays at 509 nm. This matched the spectral characteristics of commonly available FITC filter sets, increasing the practicality of use by the general researcher. Many other color mutations have also been made, such as blue fluorescent protein (EBFP), cyan fluorescent protein (ECFP) and yellow fluorescent protein derivatives (EYFP). EBFP derivatives contain the Y66H mutation, which causes the chromophore to form with an indole rather than phenol component. Several additional compensatory mutations in the surrounding barrel are required to restore brightness to this modified chromophore due to the increased bulk of the indole group. The red-shifted wavelength of the EYFP derivatives is accomplished by the T203Y mutation and is due to π-electron stacking interactions between the substituted tyrosine residue and the chromophore. Besides the color variation, some other modifications have also been made on GFP to change its fluorescent characteristics, such as calcium-sensitive GFP, redox-sensitive GFP and pH-sensitive GFP.

3.3 Usage of GFP and its derivatives

GFP and its derivatives are widely used in the life science research field. GFP is usually much less harmful when illuminated in living cells compared to most small fluorescent molecules such as fluorescein isothiocyanate and FITC, which are strongly phototoxic when used in live cells. GFP can also be expressed in many different organisms, from bacteria to mammalian cells, without losing its fluorescence properties. This makes GFP a very good expression marker for detecting gene expression and regulation. The emergence of Ca^{2+}-sensitive, pH-sensitive (Miesenbock et al. 1998) and redox-sensitive GFP derivatives (Hanson et al. 2004; Cannon and Remington 2006) also allows observation and

study of changes of physiological conditions in living cells or various systems, such as reconstituted vesicles. Another important use of GFP is the application in the fluorescence resonance energy transfer (FRET). An electronic excited donor chromophore may transfer energy to a proximate acceptor chromophore through nonradiative dipole–dipole coupling. By this mechanism, FRET can be used to investigate the interaction between macromolecules and the dynamic molecular events within living cells (Pollok and Heim 1999). Besides the fluorescence applications of GFP, it could also be used as a fusion protein tag for crystallization. In the crystallization of GFP-ubiquitin and GFP-UBM fusion proteins, the tyrosine residues that are involved in mediating crystal contacts are arranged in a belt on the surface of the β -barrel structure of GFP in both crystals (Hakansson and Winther 2007; Suzuki et al. 2010). This indicated that GFP could assist the crystallization of fusion proteins. Considering its good solubility and structural stability, GFP is a good candidate for a fusion partner to increase the hydrophilic portion of a membrane protein.

CHAPTER 2. MATERIAL AND METHODS

1. Molecular Engineering of *Rhodobacter sphaeroides*

Molecular engineering has been performed on different *Rhodobacter sphaeroides* strains to produce various mutants of *Rs*C*c*O. Histidine tags are engineered onto either the C-terminus of subunit I or the C-terminus of subunit II of *Rs*C*c*O (Zhen *et al*, 1998) so that after expression the protein could be purified with Ni-NTA columns. Genes encoding all four subunits were inserted into the over-expression plasmid pRK415-1 (Zhen et al. 1998) in different combinations. Biparental conjugation (Zhen *et al.*, 1998) was used to transfer the expression plasmid from *E. coli* strain S17-1 to *Rhodobacter* expression host strains (Δ123 or Δ1Δ4). Different constructs of *Rs*C*c*O used in this research and their genotyes are listed in Table 2.1. Detailed constructions of the expression plasmids for these mutants are shown in each chapter.

2. Cell Growth

Rhodobacter sphaeroides strains were first streaked from single colonies onto Sistrom's plates and grown at 30°C for 4-5 days. Then the cells were scraped into 2.8 L Fernbach flasks containing 800 mL of Sistrom's medium (Sistrom *et al*, 1962) with 25mg/mL streptomycin, 25 mg/mL spectinomycin and 1mg/mL tetracycline and grown aerobically in the dark at 30°C as described (Hiser et al. 2001). After 3 days at an optical density of 1.5-1.8 at 600 nm and pH of 8.5-9.0, *R.sphaeroides* cells were harvested by centrifugation in a GS-3 rotor at 14,000 x g for 20 minutes at 4°C. The KPi buffer

Strain name	Host strain	Histag position	Phenotyes
PJL16 (Chapter 3)	Δ123	Subunit II	Subunit I –EYFP fusion mutant, wild type subunit IV EYFP gene is linked through a 4 amino acids linker (GGAS) to the C-terminus of subunit I.
PJL33 (Chapter 4)	Δ123	Subunit II	Short-short subunit I mutant. 16 amino acids were removed from the C-terminus of subunit I.
PJL45 (Chapter 4)	Δ123	Subunit I	E552A mutation on subunit I. wild type subunit IV
PJL49 (Chapter 4)	Δ123	Subunit I	Short subunit I mutant. Wild type subunit IV W560 is mutated into a stop codon (TGG->TGA), so last 6 amino acid of subunit I C-terminus are "deleted" from the expressed protein.
PJL63 (Chapter 4)	Δ123	Subunit II	Subunit I –subunit III fusion mutant. Wild type subunit IV. N-terminus of subunit III gene is linked to the C-terminus of subunit I.
PJL34 (Chapter 5)	Δ1Δ4	Subunit II	K362M with short short subunit IV
PJL35 (Chapter 5)	Δ1Δ4	Subunit II	D132A with short short subunit IV

Table 2. 1: Mutant strains created and used in this thesis

containing 50 mM KH_2PO_4 and 1 mM EDTA, pH 6.5 (Zhen et al. 1998) was used to resuspend the harvested cells. The cells were stored frozen at -70°C.

3. Preparation of *R.sphaeroides* Cytoplasmic Membranes

Before the thawing of *R.sphaeroides* cells , small amounts of DNase I and RNase were added. More KPi buffer was added according to the amount of the cells (for a growth of 24L the final volume of the cell resuspension is usually ~ 200 mL). The cell resuspension was then homogenized and cells were broken with two passages through the French press at 20,000 psi. Unbroken cells and debris were removed by centrifugation at 30,000 x g for 30 minutes at 4°C. Then the supernatant was collected and an ultracentrifugation at 200,000 x *g* for 1.5 hours was performed to harvest the cell membrane fraction. The cell membrane pellet was resuspended in either a lower salt buffer containing 10 mM Tris, 40 mM KCl, pH 8.0 for subunit I histidine-tagged strains, or a high salt buffer containing 10 mM Tris, 220 mM KCl, pH 8.0 for the subunit II histidine-tagged strains. The membrane sample were then quick-frozen in liquid nitrogen and stored at –80°C.

4. UV-Visible Spectroscopy

UV-Visible spectra were taken using a Perkin-Elmer Lambda 40P UV-visible spectrophotometer. A reduced minus oxidized C*c*O difference spectrum was performed on the *R.sphaeroides* membrane fraction; sodium dithionite and ferricyanide were used to fully reduce or oxidize the enzyme samples, respectively. The enzyme was first diluted in a buffer containing 100 mM HEPES, pH 7.9, 1 mM EDTA, and 0.1% dodecyl maltoside prior to the spectra being taken. The extinction coefficient used was $\Delta\varepsilon_{606\text{-}630} = 24$

$cm^{-1}mM^{-1}$ (Zhen et al. 1998). For absolute spectra of the dithionite-reduced C*c*O, the extinction coefficient used was $\Delta\varepsilon_{606\text{-}640} = 40\ cm^{-1}mM^{-1}$ (Zhen et al. 1998).

5. Protein Concentration Assay

The BCA (bicinichonic acid) Protein Assay Reagent Kit from Pierce (Smith et al. 1985) was used to measure the total protein concentration in the membrane sample. Bovine serum albumin (BSA) standards and the resuspended membrane samples were diluted in a buffer containing 10 mM Tris, 40 mM KCl and 0.25% deoxycholate, (pH 11.2). Reagent A containing 1% BCA-Na_2, 2% $Na_2CO_3.H_2O$, 0.16% Na_2 tartrate, 0.4% NaOH, 0.95% $NaHCO_3$, pH 11.25 and reagent B containing 4% $CuSO_4 \cdot 5\ H_2O$ were mixed in a 50:1 ratio, and then 2 mL of the mixture was added to each of the diluted sample and BSA standard tubes. After incubation at 60°C for 30 min, the absorbance of these samples was measured at 562 nm. A standard curve was produced with the absorbance measurements at 562 nm for the BSA standards with known protein concentration. The protein concentration of the membrane sample was calculated with this standard curve.

6. Solublization of the Membranes

The *R. sphaeroides.* cell membrane sample was diluted to a protein concentration of 10 mg/ml with buffer containing 10 mM Tris (pH 8.0), 40 mM or 220 mM KCl depending on the position of the histidine tag as described above, and 1 mM imidazole. Dodecyl maltoside was then added to the membrane resuspension sample to a final concentration of 1% (w/v). The solution was stirred for 20 minutes at 4°C and unsolublized material was

removed by ultracentrifugation at 200,000 x g for 30 minutes. The supernatant containing *Rs*C*c*O was collected and used immediately for further column purification.

7. SDS-PAGE

Sodium dodecyl sulfate polyacrylamide gel electrophoresis (SDS-PAGE) was used to detect the C*c*O subunit composition including different forms of subunits and the impurities contained in the C*c*O sample. Approximately 10 μg of protein in sample buffer containing 25 mM Tris, pH 6.5, 40% glycerol, 8% SDS and 0.08% bromophenol blue was loaded onto an 8% acrylamide stacking gel at pH 6.8 on top of an 18% acrylamide separating gel at pH 8.8. The gel was electrophoresed at 100 V at room temperature (Peiffer et al. 1990). The gel was then stained with Coomassie blue and destained with 7.5% glacial acetic acid for 3 times (Hiser et al. 2001). Polypeptide sizes were estimated from low-molecular weight range markers from New England Biolabs.

8. Purification of the *Rs*C*c*O

In order to obtain purified *Rs*C*c*O enzyme complex for crystallization or the reconstituted vesicle assay, different FPLC (fast protein liquid chromatography) column purification protocols were used. For crystallization, the enzyme was purified via a single step Ni-NTA FPLC purification method developed by Ling Qin (Qin et al. 2006). To reconstitute *Rs*C*c*O into vesicles, a further purification procedure with a DEAE sepharose ion-exchange column was used.

8. 1 Ni-NTA purification of the Subunit I Histidine-Tagged *Rs*C*c*O

A home-packed Ni-NTA (Qiagen) column (typical volume: 18 ml) connected to an AKTA FPLC system (Pharmacia) was used to purify the *Rs*C*c*O with histidine–tags on the C-terminus of subunit I. The column was first equilibrated with 80 ml of low salt buffer A containing 10 mM Tris, 40 mM KCl, 10 mM imidazole and 0.05% dodecyl maltoside, pH 8.0. The solubilized membrane fraction of *Rs*C*c*O was slowly loaded onto the column via a 150 mL superloop (flow speed 0.4 mL/min). The column was washed extensively with 12 column volumes of buffer A. A linear gradient of 0 – 100% of 15 column volumes of buffer B containing 10 mM Tris (pH 8.0), 40 mM KCl, 150 mM imidazole, 0.05% dodecyl maltoside was applied onto the column after the washing step.

The *Rs*C*c*O containing fractions were selected based upon the UV absorbance from the FPLC and then collected together. The imidazole in the collected fraction was removed by washing and concentrating multiple times by using an Amicon YM100 filter unit (MW cutoff 100 kDa; maximum volume 15ml, Millipore). The yield of this column purification step was typically around 50%.

8.2 Ni-NTA Purification of the Subunit II Histidine-Tagged *Rs*C*c*O

The method used for the subunit II histidine tagged *Rs*C*c*O purification is very similar to the method for the subunit I His-tag *Rs*C*c*O. Firstly the detergent solublized membrane sample was loaded onto the home-packed Ni-NTA column (column volume: 18-20 ml) connected to an AKTA FPLC system that was pre-equilibrated with 80 ml high salt buffer A containing 10 mM Tris , 220 mM KCl, 2.5 mM imidazole and 0.05% dodecyl maltoside, pH 8.0. After washing with 12 column volumes of buffer A, a two step gradient of increasing concentration of buffer B containing 10 mM Tris, pH 8.0, 220 mM KCl, 150

mM imidazole, 0.05% dodecyl maltoside was used instead of the one step gradient step in methods 2.8.1. First the percentage of buffer B was increased to approximately 8-10% (approximate imidazole concentration: 15 mM) and held constant for approximately 6 column volumes. The first peak, a impure, red-colored cytochrome *c* oxidase bound to an contaminating species including cytochrome bc_1 was eluted in this step. After this washing step, the concentration of buffer B was increased to 100% (final imidazole concentration: 150 mM) with a linear gradient and the second peak containing purer green colored C*c*O was eluted and the green fractions in the second peak were collected. The collected enzyme was then concentrated with a Amicon YM100 filter unit. The buffer was exchanged to 10 mM Tris, pH 8.0, 150 mM NaCl, with 0.16% decyl maltoside by washing and concentrating 2 – 3 times. The typical yield of purified protein is approximately 30-40%.

8. 3 Ion-exchange Column Purification of *Rs*C*c*O

For *Rs*C*c*O that is used for activity and proton pumping mechanism study, a second purification with DEAE ion exchange column was performed. Concentrated enzyme from Ni-NTA purification (equilibrated in buffer A below) was loaded onto a DEAE ion exchange column (column size: 20 ml) pre-equilibrated with 100 ml buffer A containing 10 mM Tris, 0.05% dodecyl maltoside, pH 8.0. The column was washed with buffer A for three column volumes before a linear gradient of 0-100% buffer B containing 10 mM Tris, 0.5 M KCl, 0.05% dodecyl maltoside, pH 8.0 was applied. The length of the gradient was 15 column volumes. Green fractions from the linear gradient were pooled, concentrated and the buffer was exchanged to 10 mM Tris, pH 8.0, 0.16% - 0.24% decyl maltoside by washing and concentrating 2 - 3 times by using a YM100 filter unit or in a stirred

ultrafiltration cell as described above. The typical yield of this column purification step with washing and concentrating was around 50%.

9. Reconstitution of Cytochrome *c* Oxidase into Vesicles

To investigate proton pumping abilities and the respiratory control ratios of the various *Rs*C*c*O proteins, the *Rs*C*c*O was reconstituted into vesicles (*Rs*COV). A cholate dialysis method (Hiser, Mills *et al.* 2001) is used to reconstitute *Rs*COVs. In this method, cholate detergent is added to the enzyme to displace the dodecyl/decyl maltoside detergent from the enzyme. Cholate detergent is subsequently easily eliminated by dialysis due to its high CMC, critical micelle concentration, of 14 mM. As the detergent concentration is gradually decreased in the presence of lipid a unilamellar vesicular structure is formed. The soybean polar lipid extract, asolectin obtained from Avanti Polar Lipid, Inc. (Cat No 541602) is used in the procedure. It mainly contains phosphatidyl ethanolamine (22.1%), phosphatidyl inositol (18.4%), phosphatidyl choline (45.7%), phosphatidic acid (6.9%), and other components (6.9%). Before usage, the asolectin was precipitated with acetone and then extracted with diethyl ether. The asolectin was suspended to a concentration of 40mg/ml and sonicated at 4°C under argon gas using a microtip sonicator (Heat systems-Ultrasonics sonicator Model W-225) with in a buffer containing 75 mM HEPES-KOH, 14 mM KCl (pH 7.4) 2% cholate. After the solution became translucent, the suspension was centrifuged for 15min at 12,000 x *g* to remove unsolublized particles. *Rs*C*c*O was prepared at a final concentration of 4μM with 4% cholate in the same buffer condition (75 mM HEPES-KOH, 14 mM KCl, pH7.4). The *Rs*C*c*O solution was then mixed with the sonicated asolectin suspension to obtain a final concentration of 2 μM

oxidase and 20 mg/ml lipids (Hiser et al. 2001). The cholate was removed using five steps of dialysis with rapid stirring at 4°C in Spectrapor dialysis tubing (#25225/204, 12-14,000 Mr cut-off) to remove detergent and form the COVs. (1) 6 hours in a 100 volume of 75mM HEPES-KOH pH7.4, 14mM KCl with, and (2) without 0.1% cholate respectively; (3) 12 hours in 100 volumes of 50 mM HEPES-KOH pH7.4, 25mM KCl, 15 mM sucrose; (4) and (5) a 12 hours dialysis two times in 500 volume of 50 M HEPES-KOH (pH 7.4), 45 mM KCl and 44 mM sucrose as previously described (Hosler et al. 1992). Sucrose was added to maintain the osmotic conditions.

After cholate dialysis, the vesicles were shown to have C*c*O in the predominantly mitochondrial configuration (Nicholls et al. 1980) with the the cytochrome *c* binding site on the outside and to have a high respiratory control ratio.

10. Cytochrome *c* Oxidase Activity Assay

The oxidase activity of *Rs*C*c*O and was measured polarographically by using a Gilson model 5/6H oxygraph with a closed thermostatted chamber containing a Clark-type oxygen electrode (Ferguson-Miller et al. 1976). The assay is performed at 25°C in a 1.75 mL reaction cell containing 50 mM KH_2PO_4, pH 6.5, 0.05% dodecyl maltoside, 2.8 mM ascorbate, 0.55 mM TMPD and 30 μM of horse heart cytochrome *c*. The oxidase concentrations were in the range of 5 nM to 50 nM. Soybean phospholipids, asolectin (1 mg/mL) was also added to stimulate the enzyme for full activity. The activity of *Rs*C*c*O is calculated as described in (Fetter et al. 1995)

Measurement of the activity of COVs was performed in the controlled state (absence of ionophores), and with the addition of valinomycin, which dissipates the membrane

potential by equilibrating K^+ across the membrane to remove the charge ($\Delta\psi$=0). The uncontrolled condition occurs with the addition of uncouplers, FCCP (or CCCP), which transfers protons across the membrane, and this causes the proton gradient to be dissipated (ΔpH=0) and shows the highest rate of activity. Then the Respiratory Control Ratio, RCR for the *Rs*COV is calculated (RCR=uncontrolled state activity/ controlled state activity). For a typical cytochrome *c* oxidation rate measurement, 4.2 μM of cyt^{2+} was mixed with 0.04 μM of aa_3 in the COVs (Inside buffer: 50 mM HEPES-KOH, pH7.4 +43 mM KCl). Data scans were collected (1000 scans/s) by Photophysics stopped flow apparatus. For the measurement of alkalinization inside the vesicle, 4.2 μM of cytochrome c was mixed with 0.04 μM of oxidase in the COVs (Inside buffer: 50 mM HEPES-KOH, pH 7.4 +43 mM KCl). Data scans were collected (1000 scans/s) by Photophysics stopped-flow apparatus. For EYFP-COVs, the fluorescence is and detected at 525 nm. For the wild type COVs, the fluorescence is excited at 465 nm detected at 510 nm

11. Crystallization of the *Rs*C*c*O

11.1 Four-subunit RsCcO Crystallization

To obtain the four-subunit *Rs*C*c*O crystals, either hanging drop or sitting drop crystallization setups could be used. Figure 2.1 shows the hanging-drop crystallization set-up and sitting-drop crystallization setup. In the hanging drop set up, the crystal grows faster than the sitting drop set up. However, in a sitting-drop crystallization experiment, a much larger volume can be used in order to obtain larger crystals. All the crystallization experiments were performed at 4°C. In the hanging-drop crystallization set up, 2 μL of enzyme solution containing 10 mM Tris, 0.16-0.24% decyl maltoside, pH 8.0 and 100-120

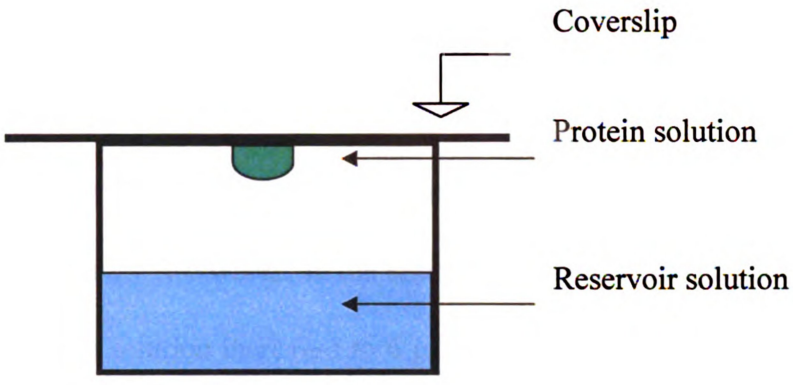

A: Hanging Drop

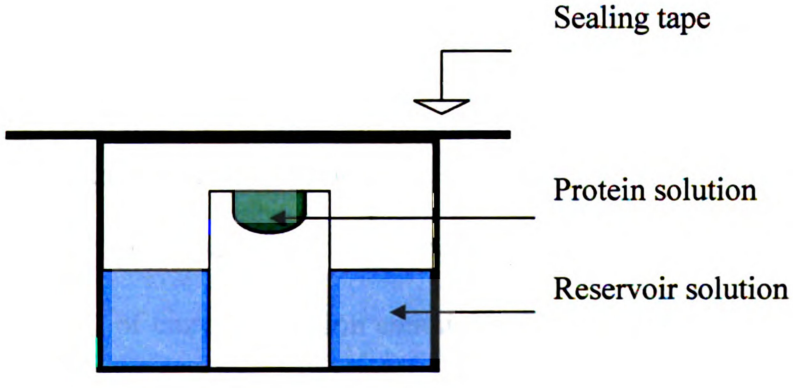

B: Sitting Drop

Figure 2. 1: Crystallization setup for the *Rs*C*c*O

μM *Cc*O was mixed with 1 μL of reservoir solution containing 100 mM sodium citrate, 100 mM NaCl, 18-23% PEG-400, pH 5.6-5.8 and 1 μL of crystallization additive solution containing 5% heptanetriol, 33 mM $MgCl_2$, and 0.026% dodelcyl maltoside. The crystallization drop was then incubated at 4°C for crystal growing. Triangular crystals of four subunit *Rs*C*c*O usually appeared after 3-4 days and continued growing to up to 0.2 × 0.2 × 0.1 mm in approximately two weeks. In the sitting drop crystallization set-up, the typical volume of the drop solution increased to 6 μL of enzyme solution containing 10 mM Tris, pH 8.0, 0.16-0.20% decyl maltoside and 80-120 μM *Cc*O mixed with 3 μL of reservoir solution and 3 μL of crystallization additive solution as described above. The crystallization drop was incubated at 4°C and triangular crystals usually appears after 2 weeks incubation.

11.2 Two-subunit *Rs*C*c*O Crystallization

In a typical crystallization experiment to obtain crystals of the I-II subunit *Rs*C*c*O, a sitting drop crystallization set-up was mainly used as shown in Figure 2.2. For a typical crystallization set-up, 6 μL of enzyme solution containing 10 mM Tris, 50 mM NaCl, 0.20% decyl maltoside, pH 8.0 and 120 μM *Cc*O was mixed with 3 μL of reservoir solution containing 100 mM MES, pH 6.3-6.9, 24-26% PEG-400 and 3 μL of crystallization additive solution containing 5% heptanetriol, 32 mM $MgCl_2$, 1.3 mM $CdCl_2$ and 0.026% dodecyl maltoside. The crystallization drop was then incubated at 4°C and crystal showers of tiny triangular crystals of the four subunit *Rs*C*c*O started to appear after approximately 3-4 days. Larger, clustered crystals of I-II subunit *Rs*C*c*O crystals started to appear after

approximately 2 weeks and continued to grow to their full size of up to 0.2 × 0.2 × 0.1 mm in 3-4 weeks.

12. Flashcooling of the *Rs*C*c*O Crystals

Flashcooling of the crystals was performed to freeze the crystals prior the synchrotron X-ray diffraction. The 4-subunit *Rs*C*c*O crystals were grown at 4°C, and would quickly dissolve under room temperature, thus the flashcooling procedures were performed in the cold room. Drierite could be used as a desiccant in the cold room to reduced the humidity and prevent the formation of ice crystals during the procedure. The crystals of the *Rs*C*c*O were picked up from the original crystallization drop with a cryoloop and soaked in approximately 25 μL of stabilizing solution in a sitting drop well. The stabilizing solution was made to mimic the assumed concentration of ingredients in the crystallization drop after equilibrium except for a little less detergent in a sitting drop well. Usually the stabilizing solution contained 91 mM sodium citrate (pH 5.6-5.8), 91 mM NaCl, 18 mM Tris (pH 8.0), 30 mM $MgCl_2$, 1.5 mM CdCl, 2.5% heptanetriol, 0.16% decyl maltoside, 0.016% dodecyl maltoside, and 18-23% PEG-400. A small aliquot (10μL) of the cryosolution containing the same ingredients as those in the stabilizing solution except for a higher (30-32%) PEG-400 concentration was added to the stabilizing solution containing the crystals and then the two solutions were carefully mixed. A small aliquot (10 μL) was then taken out from the sitting drop well to return the drop volume to 30 μl. The same procedure was repeated several times until approximately the entire solution in the sitting drop well had been exchanged to the cryosolution. Adding small aliquots of the cryosolution ensured the gradual increase of PEG-400 concentration and thus protected the crystals from being damaged due to dramatic increase in the osmotic pressure in the

surrounding environments. The crystals were then picked up again using a cryoloop and submerged into liquid nitrogen. The flashcooled crystals were then stored in liquid nitrogen in cryovials until data collection.

13. Data Collection and Processing

X-ray diffraction data were collected at GM/CA-CAT Station 23D-B and LS-CAT, Station 23D-G, Advanced Photon Sources, Argonne National Laboratory. The detector used was MARCCD-300. The data set was collected by the rotation method. During the data collection from the I-II subunit C*c*O crystals, a 180° rotation about the ϕ angle was performed with 0.3° per frame. The exposure time was set to 0.5second to 2 second depended on the X-ray intensity. Sometimes two data sets were collected on a single crystal, one for the high resolution range with a crystal-to-detector distance of about 180 mm and a longer X-ray exposure time, and another data set for the low resolution range with a crystal-to-detector distance of approximately 260 mm and a shorter X-ray exposure time. The data were integrated, scaled and merged using with the software HKL2000 (Otwinowski and Minor 1997).

14. Molecular Replacement and Structural Refinement

For the crystal structure determination of the four subunit *Rs*C*c*O, a rigid body refinement using the coordinates of the published structure of the four subunit *Rs*C*c*O (PDB entry 1M56) or structure of the 2 subunit *Rs*C*c*O (2GSM) as the initial phasing model was performed with CNS 1.1 (Brunger et al. 1998), followed by simulated annealing, and cycles of energy minimization, model visualization and manual model building. A group B

factor refinement was performed at later stages of the refinement. Molecular visualization and model building were performed by using the program (Sack and Quiocho 1997). For the crystal structure determination of the I-II subunit *Rs*C*c*O, an initial molecular replacement search was performed by using the program Phaser (Storoni et al. 2004), using the coordinates of the two-subunit cytochrome *c* oxidase (PDB entry 2GSM) as the original search model. Refinement of the structure was performed with CNS 1.1 using cycles of simulated annealing, and energy minimization (Brunger et al. 1998). B factors were refined at the later stages. Molecular visualization and model building were performed by using the program CHAIN (Sack and Quiocho 1997). The structure was first refined at 2.5 Å resolution and then the resolution was extended to include all data up to 2.15 Å. Towards the end of refinement, restrained refinement with TLS refinement were performed using Refmac5 (Bailey 1994; Murshudov et al. 1997; Winn et al. 2001).

CHAPTER 3. CONSTRUCTION OF A FUSION PROTEIN OF *RSCCO* WITH A GREEN FLUORESCENT PROTEIN VARIANT FOR CRYSTALLOGRAPHY AND PROTON PUMPING MECHANISM STUDY

1. Introduction

Resolution of the structure of C*c*O is a crucial requirement for the full elucidation of the function and mechanism. Unfortunately, membrane proteins, due to their amphiphilic character, are particularly difficult to crystallize, and success in growing three-dimensional crystals is relatively infrequent. For the *Rs*C*c*O, more high-resolution crystal structures are still needed, especially of key mutants of C*c*O. Protein engineering provides new hope to solve this problem. Analysis of the crystal packing of the available membrane proteins shows that most crystal lattice contacts are made by the polar extra-membranous parts of the membrane protein. Therefore, increasing the polar part of a membrane protein could be a promising method of getting a well-ordered membrane protein crystal. This could be achieved by adding the proper antibody, as was done for the crystallization of C*c*O from *Paracoccus denitrificans* (Iwata et al. 1995). Another method is to use genetic engineering to fuse a soluble protein to the polar part of the membrane protein. Green fluorescent protein, GFP, is a good choice for making this kind of fusion protein(Hakansson and Winther 2007; Suzuki et al. 2010).

GFP is a spontaneously-fluorescent soluble protein isolated from the jellyfish, *Aequoria victoria* (Figure 1.8). Its natural role is to transduce the blue chemiluminescence of another protein, aequorin, into green fluorescent light by energy transfer. Its crystal structure and mechanism of fluorescence have been well studied. The formation of this chromophore is not dependent on other proteins or special co-factors. Thus active GFP can be expressed in many species, from bacteria to mammalian cells. The special chemical and physical characteristics of GFP also make it an ideal fusion protein tag. GFP is very stable under physiological conditions. Denaturation of GFP requires treatment with 6 M guanidine hydrochloride at 90°C or pH of <4.0 or >12.0.

Many GFP mutants have been produced. An interesting member of them is a yellow colored pH sensitive GFP, named Enhanced Yellow Fluorescent Protein or EYFP (Elsliger et al. 1999). The fluorescence intensity of this mutant, which is modified in residues T203Y/S65G/V68L/S72A, changes according to the environmental pH, so that it can be used as an intracellular pH indicator. In our case, it could be used with C*c*O reconstituted into vesicles to study proton pumping. Thus, in addition to providing a possible route to a higher resolution structure, a C*c*O-EYFP fusion protein could provide a sensitive tool for monitoring C*c*O function.

2. Methods and Results

The purpose of making C*c*O-GFP fusion proteins is to increase the hydrophilic portion of this membrane protein complex. By doing this the C*c*O molecules could have better contacts with each other and form better crystals that diffract to higher resolution. A GFP

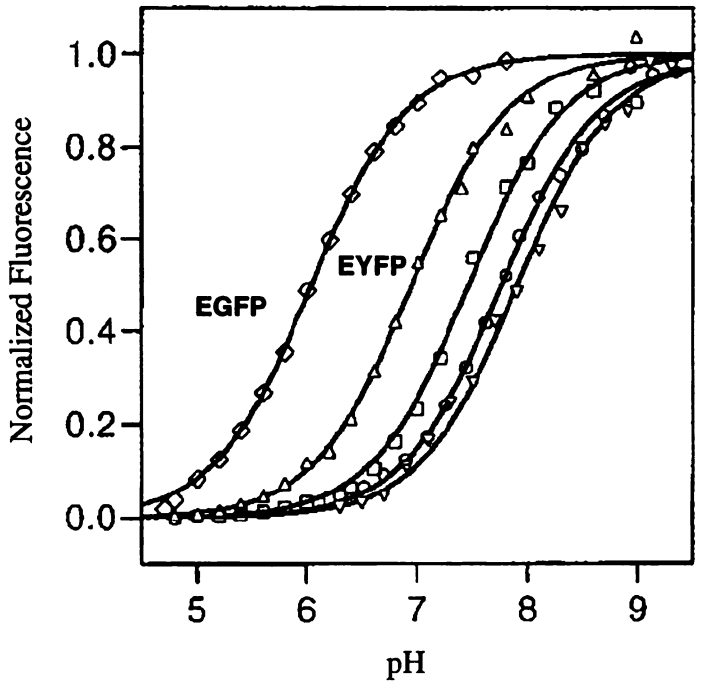

Figure 3. 1: GFP pH sensitive mutants.
This chart shows that the fluorescence strength of these mutant proteins is correlated to the pH change (Δ: EYFP. □: EYFP-H148Q). (Elsliger, M et al Biochemistry 38, 5296-5301.1999)

mutant, EYFP, was used in this project (gift from James Remington, University of Oregon). The fluorescence strength of EYFP is better than that of the traditional GFP and its pH sensitivity make it doubly valuable. In the pH range from 6 to 8, its fluorescence emission will increase with an increase in pH (Figure 3.1). A *R. sphaeroides* strain Δ123(Zhen et al. 1998) was chosen as the expression host strain. The genes for C*c*O subunits I, II and III are deleted in this strain to provide a clean background for the expression of C*c*O-GFP fusion proteins.

2.1 Expression of GFP under the control of C*c*O subunit I promoter in *Rs*

As the first step, to prove that EYFP can be expressed in *Rs*, an EYFP expression plasmid, pJL-4, was constructed (Figure 3.2). A splicing PCR method was used to integrate the gene of subunit I promoter and the coding region of EYFP together. A histidine tag and an EK site were placed between the C*c*O subunit I promoter and the EYFP gene so that the expressed protein could be further purified by Ni-NTA column chromatography. This fragment was cut with PstI and ligated into the multi-cloning site of the vector pRK415. The pRK415 is a widely used expression vector for *R. sphaeroides* (Zhen et al. 1998). It can be maintained in *E.coli* cells, and transferred into *R. sphaeroides* cells by conjugation. Firstly, through transformation, pJL-4 was transferred into E.coli strain S17-1. Then R. sphaeroides strain Δ123 cells were mixed with these S17-1 cells. In this way, pJL-4 was transferred into R. sphaeroides cells through conjugation(Zhen et al. 1998). Finally, the positive colonies were picked up on tetracycline-containing Sistrom plates and named as PJL4. A *R. sphaeroides* negative control strain PJL-C was constructed with the similar procedures except that a pRK415 empty vector was used as the conjugation plasmid.

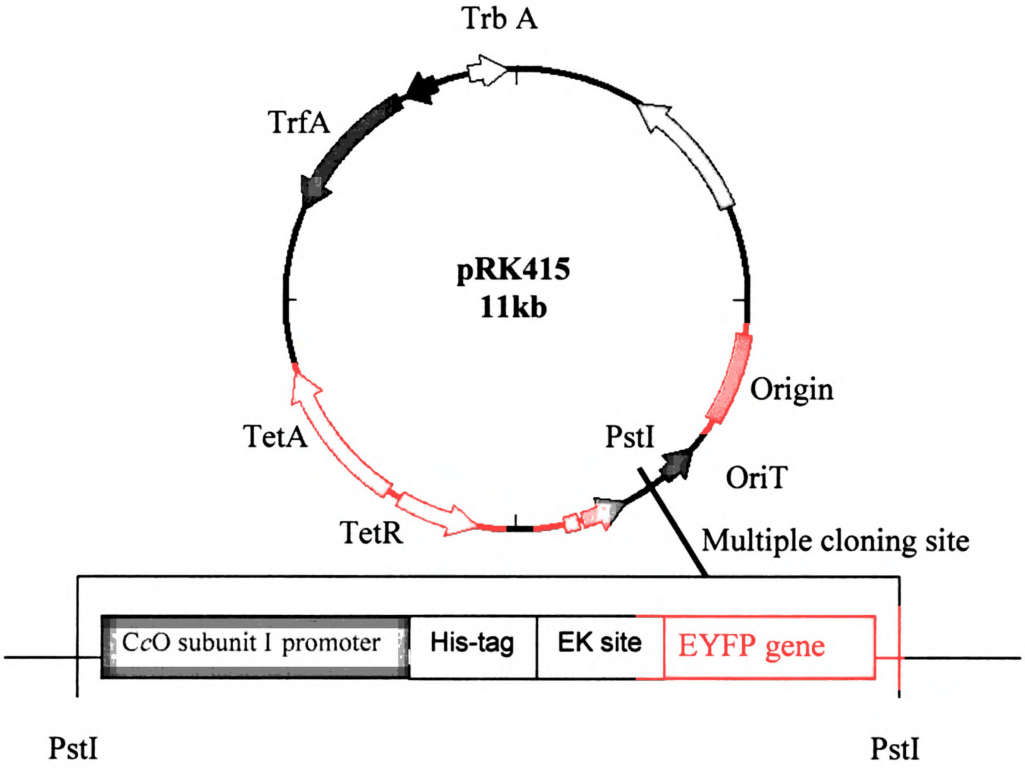

Figure 3. 2: Plasmid construction of pJL-4.
The gene for EYFP (yellow) was PCR cloned and ligated behind the C*c*O subunit I promoter (blue). Between the promoter and the EYFP gene, a DNA fragment containing a encoding 6 x histidine tag and a EK site were inserted. The histidine tag can be used to purify the expressed protein with a Ni-NTA column. The EK site is a proteolysis site that can be used to remove the His-tag from the purified protein. The whole fragment was then ligated into the pRK415-1 plasmid at the Pst I site.

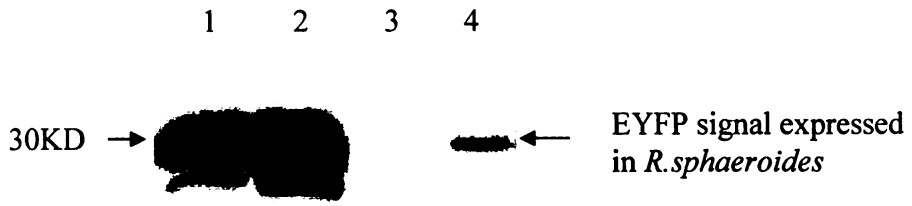

Figure 3. 3: Expression of EYFP in *Rs*.
Western blot samples: Lane 1: GFP protein (expressed and purified from *E. coli*); Lane 2: EYFP protein (expressed and purified from *E. coli*); Lane 3: Cell lysates of JL-C strain (negative control); Lane 4: Cell lysates of JL4 strain. SDS-PAGE gel concentration: 12%

Protein expression in *R. sphaeroides* was detected by western blotting using a GFP specific monoclonal antibody. Purified GFP and EYFP proteins (produced in *E. coli*) were used as the positive controls. R. sphaeroides strain cell lysates were prepared and the proteins are separated by SDS-PAGE. The results were shown in Figure 3.3, showing that this monoclonal GFP antibody can be used to detect both GFP and EYFP proteins. An EYFP signal was also detected in the cell lysates of the PJL4 strain, indicating that the EYFP was successfully expressed in this R. sphaeroides strain.

2.2 Expression of the CcO-EYFP fusion protein in *R. sphaeroides*

A CcO subunit I- EYFP expression plasmid pJL-16 was constructed (Figure 3.4). It contains the subunit I-EYFP fusion sequence and a His-tagged subunit II in its operon withe the wild type III operon. The whole protein complex can be purified with a Ni-NTA column. A short linker peptide sequence, GGAS, was placed between subunit I and EYFP to avoid a possible folding disruption. pJL-16 was transferred into R. sphaeroides strain Δ123 by conjugation to produce the CcO-EYFP expression strain PJL16.

The expression of CcO-EYFP was examined by both spectrophotometric analysis and western blotting (Figure 3.5). The western blot showed that the subunit I-EYFP fusion protein was expressed in JL16 cells and most of the signal was concentrated in the membrane fraction (Figure 3.5A). Reduced forms of heme a and heme a_3 in CcO should have a specific absorbance peak at 606 nm. Thus the CcO in the membrane extraction of R. sphaeroides can be identified and quantified by the dithionite-reduced minus ferricynide-oxidized difference spectrum. The spectrum (Figure 3.5B) showed that CcO was expressed in the strain PJL16, which is consistent with the western blot result.

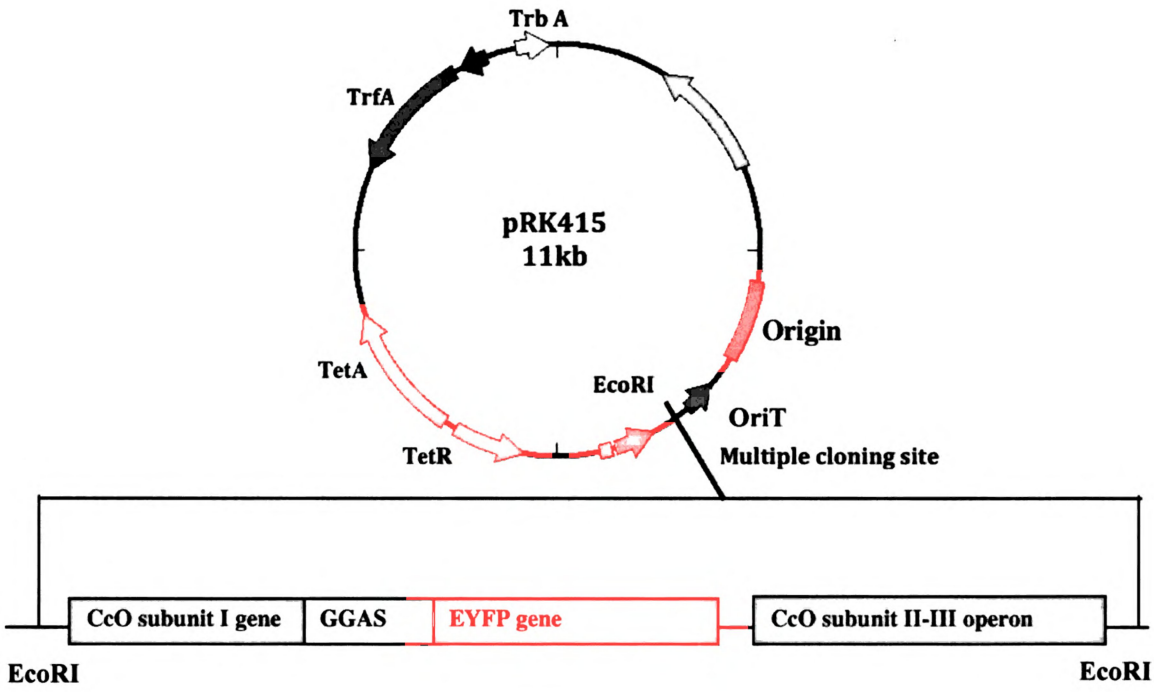

Figure 3. 4: Plasmid construction of pJL-16
The gene encoding EYFP (yellow) was linked to the gene of C*c*O subunit I (blue) through a 4 amino acids linker gene (Gly-Gly-Ala-Ser, white). The GGAS linker was used to help the folding of both EYFP and subunit I. This subunit I –EYFP fusion, together with a fragment containing the subunit II-II operon with a His-tagged subunit II, was then cloned into the expression plasmid pRK415-1 through an EcoRI site.

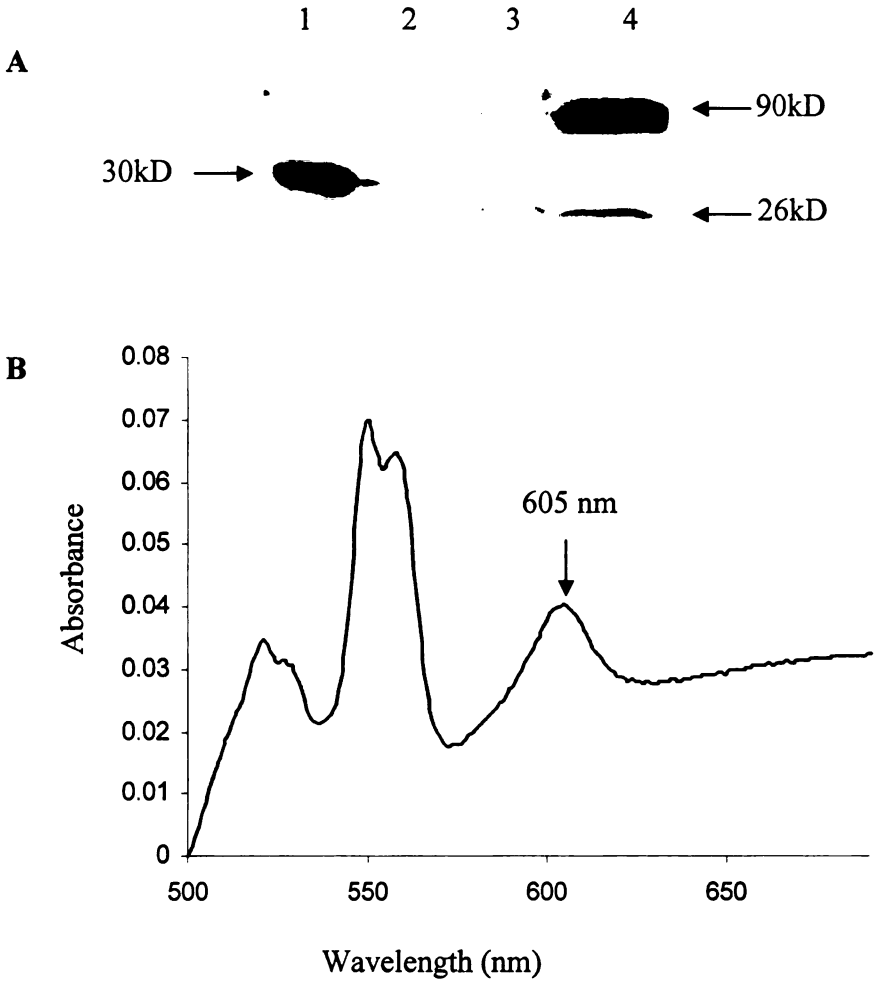

Figure 3. 5: Expression of Subunit I-EYFP CcO fusion protein.
A: Western blot result: Lane 1: EYFP protein (Purified from *E.coli,* used as a positive control), Lane 2: Cell lysates of PJL-C,used as a negative control. Lane 3: Soluble fraction of JL16 cell lysates. Lane 4: Membrane fraction of PJL16 cell lysates. **B**: Dithionite-reduced-minus-ferricyanide-oxidized difference spectra of the membrane extract from the JL16 strain

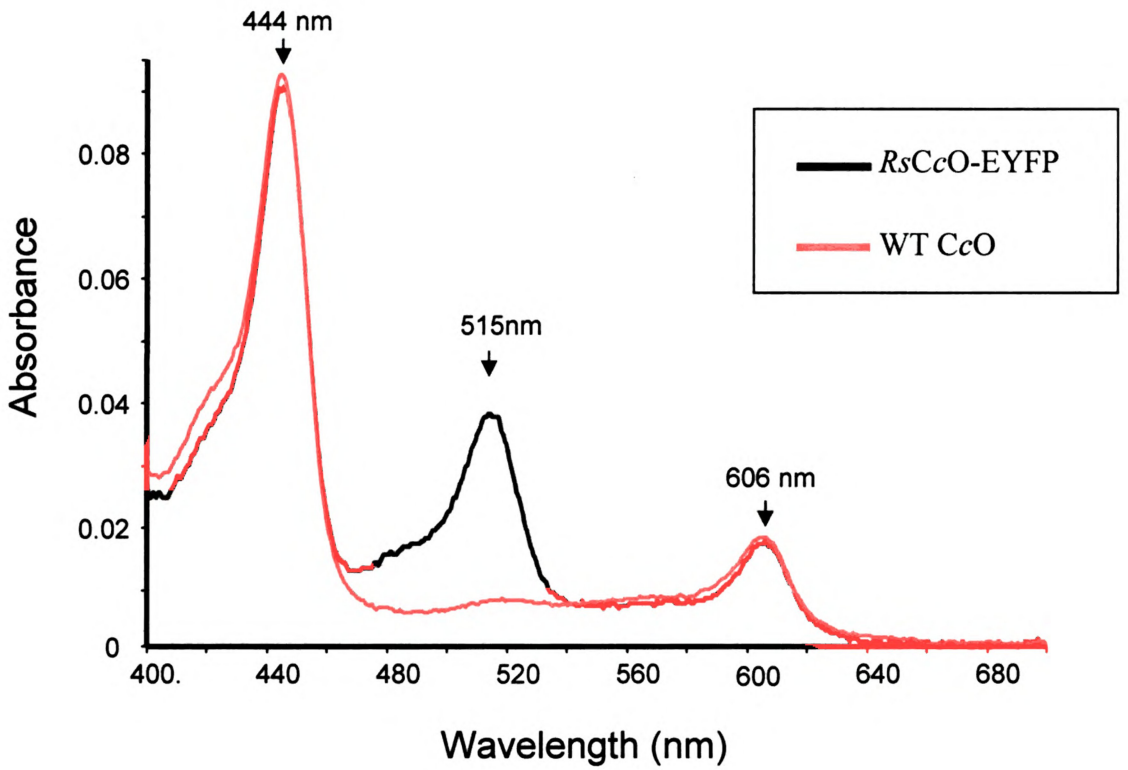

Figure 3. 6: Reduced spectra of FPLC purified RsC*c*O-EYFP fusion protein.
The blue curve is the dithionite reduced spectrum of RsC*c*O-EYFP. The red curve is the dithionite reduced spectrum of WT C*c*O. Besides the 444 nm Soret peak and the 606 nm alpha peak, a new absorbance peak was observed in the spectrum of the *Rs*C*c*O-EYFP fusion protein. This absorbance peak is believed to be caused by the EYFP.

2.3 Purification of C*c*O-EYFP fusion protein

After the confirmation of expression of C*c*O-EYFP, the fusion protein complex was purified with a Ni-NTA column followed with a DEAE-5PW anion exchange column. The protein purification procedure is described in Chapter 2. Previous studies showed that dithionite-reduced C*c*O has a Soret peak absorbance (444 nm) and a α peak absorbance (606 nm). This absorbance pattern is caused by the heme a and heme a_3 of C*c*O and has been used as the spectrum fingerprint of C*c*O (Shapleigh et al. 1992; Zhen et al. 1998). EYFP has a strong absorbance at 515 nm. Thus all those absorbance peaks were expected in the spectrum of C*c*O-EYFP. The dithionite-reduced spectrum of pu rified C*c*O-EYFP proved this expectation (Figure 3.6). As a comparison, the WT C*c*O only has the Soret peak and the α peak. A fluorescence spectrum was also taken for the purified C*c*O-EYFP protein. Results showed that this fusion protein has a similar fluorescence pattern as the purified EYFP (Figure 3.7). During the purification, this subunit I-EYFP C*c*O protein was partially degraded. The running profile of DEAE-5PW column showed that there were 2 different fractions for the CcO-fusion protein (Figure 3.8A). SDS-PAGE was performed to compare the proteins of these two fractions (Figure 3.8B). The results showed that in the first peak fraction, subunit I-EYFP protein was heavily degraded while in the second peak, the protein is purer than in the first peak. The spectrum of the degraded form of CcO-EYFP showed a decrease in the 515 nm, suggesting that the EYFP was cut off from the subunit I-EYFP full-length protein (Figure 3.8C). Therefore, after this column, the peak 2 fraction was collected and concentrated.

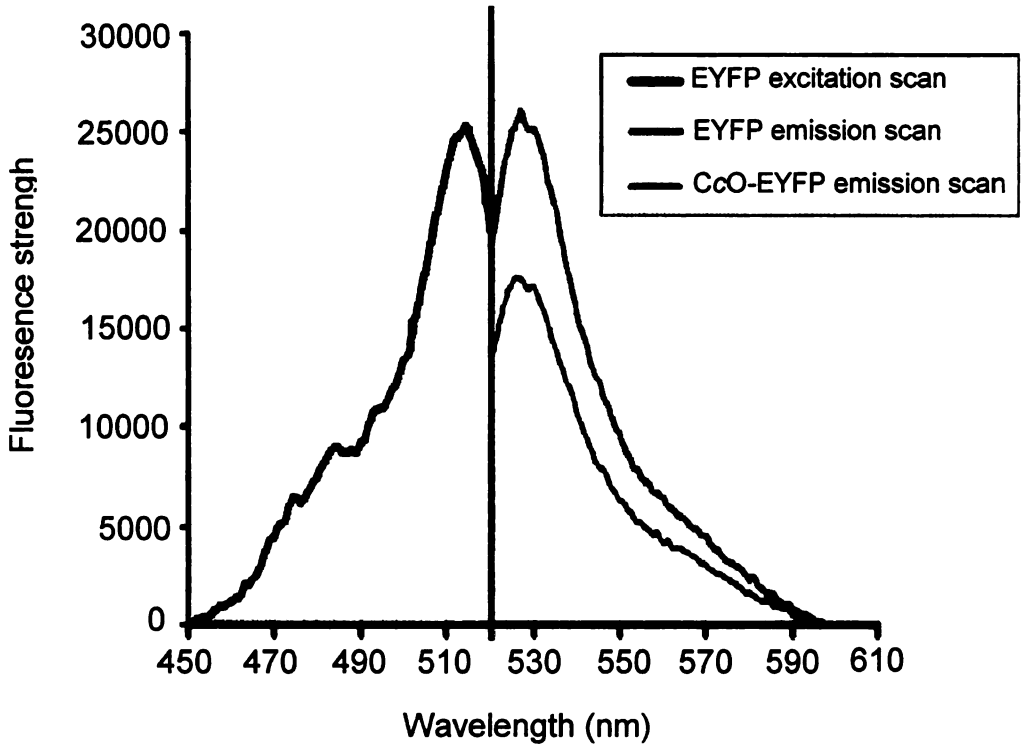

Figure 3. 7: Fluorescence spectrum of EYFP and CcO-EYFP fusion protein.
The left side of this figure is the excitation scan, shows that the excitation wavelength of EYFP is 515 nm. The right side showed that the C*c*O-EYFP and EYFP have the same emission feature. (Buffter: 50 mM HEPES-KOH, pH 7.4, with 0.1% DDM. Protein concentration: EYFP: 5μM, C*c*O-EYFP: 3.5 μM)

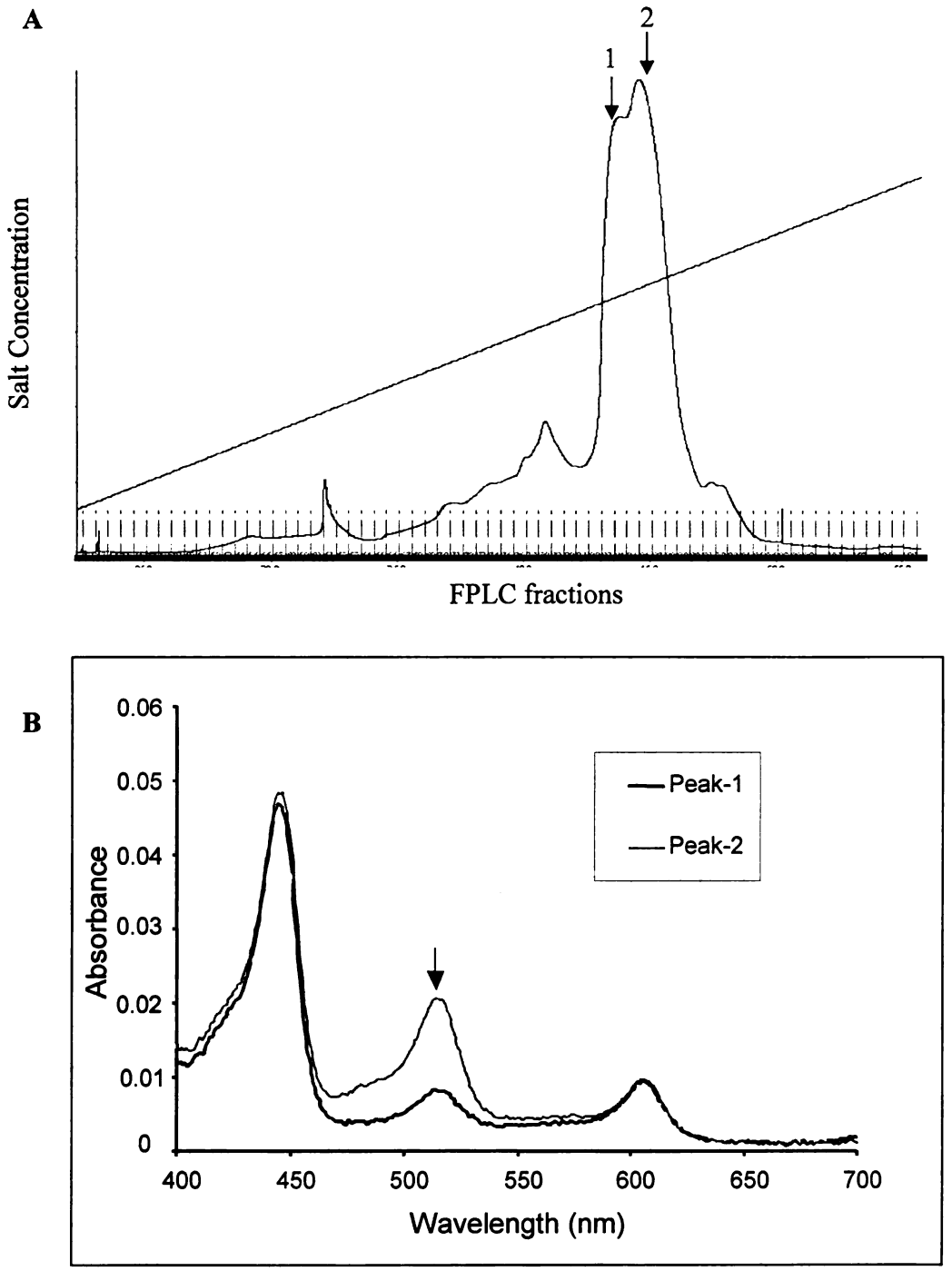

Figure 3. 8: Proteolysis of CcO-EYFP protein

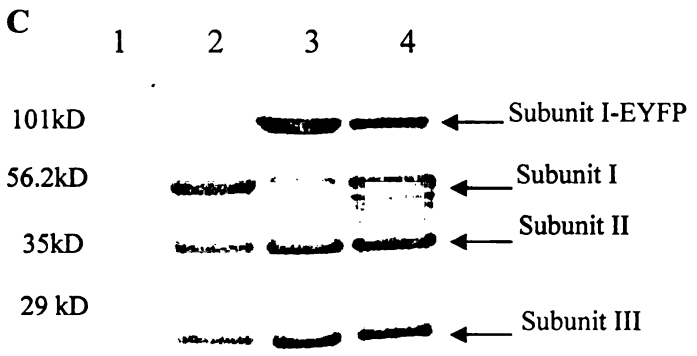

Figure 3. 8: Proteolysis of CcO-EYFP protein
A: DEAE-5PW column running profile **B**: Dithionite-reduced only spectrum for proteins from peak-1 and peak-2 fraction. The decrease at 515 nm indicated that the EYFP of peak-1 fraction is partially lost. **C**: SDS-PAGE analysis of proteins from peak-1 and peak-2 fraction. Lane 1: Bio-Rad Prestain Broad Range Protein marker. Lane 2: Purified wild type C*c*O protein. Lane 3: Purified CcO-EYFP from peak-2 fraction. Lane 4: Purified C*c*O-EYFP from peak-1 fraction. (SDS-PAGE gel concentration: 18%)

2.4 Activity assay of *Rs*C*c*O-EYFP fusion protein

An activity assay was also performed on the purified *Rs*C*c*O-EYFP fusion protein. The maximum turnover number (molecular activity) of *Rs*C*c*O-EYFP fusion protein and WT C*c*O was measured polarographically. The results show that the *Rs*C*c*O-EYFP fusion protein has the similar activity as the wild type C*c*O (Table 3.1).

2.5 Crystallization attempts and results

Preliminary crystallization attempts of the purified C*c*O-EYFP protein were performed. Wild type C*c*O crystallization conditions as described in Chapter 2 have been tried on this fusion protein. No crystal was achieved in either 2 or 4 subunit crystallization conditions. A Hampton crystallization screening kit was also used. Of the 48 different conditions of this kit, some small irregular crystals were formed in one drop. The color of the crystal was dark red, which was similar to the color of wild type C*c*O crystals. Four crystals were analyzed at the Advanced Photon Source synchrotron radiation facility, Argonne National Laboratory. However, none of them provided useful diffraction data. This indicated that the quality of the crystals and the crystallization conditions still needed to be improved.

2.6 Use of GFP mutants as indicators of pH in reconstituted vesicle to study the proton pumping mechanism

C*c*O not only reduces O_2 to water, but also pumps protons to produce a transmembrane electrochemical potential. The proton pumping and pathways and mechanisms have been studied (Michel 1998; Mills and Ferguson-Miller 1998; Zaslavsky and Gennis 2000). However, the mechanism of coupling of the proton pumping with the oxygen reaction chemistry and the pathway for proton backleak are still unclear. Reconstituted C*c*O in

Proteins	Activity ($e^-/aa_3/sec$)
WT C*c*O	1135
CcO-EYFP	1097

Table 3. 1: Activity of FPLC purified RsCcO-EYFP fusion protein

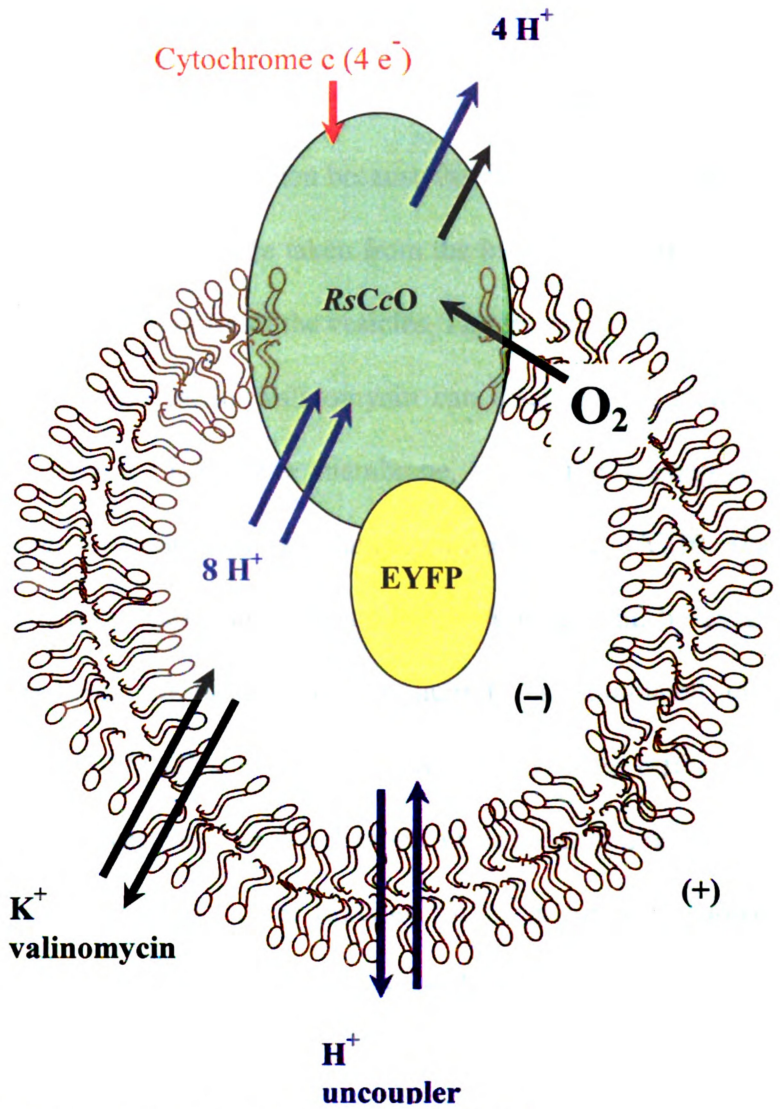

Figure 3. 9: Reconstituted vesicles of *Rs*C*c*O-EYFP

This is a diagram of Cytochrome Oxidase Vesicles (COVs) and ionophore condition for measuring proton pumping and uncoupling with Photophysics stopped-flow apparatus. Reconstituted cytochrome *c* oxidase vesicles (COVs) was produced with different concentration of HEPES-KOH, pH 7.4 buffer using the cholate dialysis method. EYFP, which is conjugated onto the subunit I of C*c*O, was placed inside the vesicle. In the controlled state high membrane potential difference ($\Delta\Psi$) and pH gradient (ΔpH) is maintained, so that C*c*O shows low activity. The membrane potential and proton gradient can be dissipated by adding valinomycin and uncoupler (CCCP) respectively.

proteoliposome vesicles (COV) has provided some insights on movement of protons in C*c*O (Hosler et al. 1992; Zaslavsky and Gennis 2000; Mills et al. 2002; Mills and Ferguson-Miller 2003).

The difference between C*c*O free enzyme and C*c*O in COVs is that the membrane separates the inside from the outside (Figure 3.9). A membrane potential and a proton gradient is built up during the reaction because the electrons are donated from cytochrome *c* on the outside, while protons are taken from the inside to support the oxygen chemistry and to be pumped to the exterior of the vesicles. This potential gradient inhibits the activity of C*c*O. The potassium carrier valinomycin can dissipate the membrane potential by equilibrating potassium across the membrane, while the uncoupler reagents, FCCP (carbonylcyanide-*p*-trifluoromethoxy-phenylhydrazone) or CCCP (carbonyl cyanide m-chlorophenyl-hydrazone), can eliminate the proton gradient, by equilibrating protons. When both gradients are dissipated, the activity is stimulated giving rise to the "uncontrolled" state of COVs. During this process, by using different pH sensitive dye outside or inside the vesicles, the pH change can be measured and the proton movement pattern can be investigated. However, previous studies in our group showed that if we put a pH sensitive dye, such as phenol red, inside the vesicles, the absorbance signal and properties of the dye appear to be modified when inside the vesicle. Another dye, pyranine, behaves better and is preferred to study inside vesicle pH changes, but its signal is also very weak and hard to quantify due to the small interior capacity of the vesicles (Thesis of Dr. Namjoon Kim, personal communication). The GFP pH sensitive mutant protein can be an alternative candidate for the fluorescent pH probe. In construct pJL16, EYFP is attached to the C-terminus of subunit I. After reconstitution, the EYFP should be oriented to be inside

the vesicles. The fluorescence emission of EYFP will change according to the internal pH environment. This special characteristic makes it a good fluorescent pH probe to measure the pH change inside the vesicles. However, the size and the hydrophilic characteristics of EYFP might disrupt the vesicle reconstitution. So the first question was, could this EYFP-C*c*O fusion protein be reconstituted into the vesicles like the wild type enzyme?

2.6.1 Reconstitution of COVs with C*c*O-EYFP fusion protein

Both subunit I-EYFP and wild type C*c*O reconstituted vesicles were prepared with cholate dialysis method (Hosler et al. 1992) as described in Chapter 2. After the reconstitution, the inside of vesicles contained 75 mM HEPES-KOH buffer and the vesicles were resuspended in 50 μM HEPES-KOH buffer with 45 mM KCl and 44 mM sucrose to stabilized the osmotic pressure. The final concentration of enzyme in COVs is measured by a dithionite-reduced-minus-oxidized spectrum.

2.6.2 Activity assay and RCR of EYFP-COVs

The activity and respiratory control ratio (RCR, the ratio of uncontrolled state rate to the controlled state rate) of EYFP-COVs was measured with a Gilson oxygraph as described in Chapter 2. The purpose of this assay is to compare the activity of *Rs*C*c*O-EYFP COVs and WT COVs. The results are shown in Table 2. Usually the RCR of wild type COVs is in a range of 6~10. From these results we can see that the *Rs*C*c*O-EYFP COVs had a similar reaction rate and RCR as the wild type COVs. This means that the EYFP did not affect with the reconstitution of COVs, and that the C*c*O-EYFP is in its normal orientation with the cytochrome *c* binding site on the outside of the vesicles.

Type of COVs	Controlled state activity (e^-/aa3/sec)	Uncontrolled state activiy(e^-/aa3/sec)	RCR
Measured by oxygen consumption			
WT CcO	303	1320	6.2
CcO-EYFP s	166	950	5.7
Measured by cytochrome c oxidation (stop flow)			
WT CcO	201	1470	7.3
CcO-EYFP	185	1018	5.5

Table 3. 2: RCR measurement results of RsCcO-EYFP COV

2.6.3 Preliminary fluorescence stop-flow analysis of EYFP-COV

The main purpose of reconstituting vesicles with EYFP-C*c*O was to use the EYFP directly to measure the pH changes inside the vesicle. The stopped-flow method, as described in Chapter 2, was used to measure the cytochrome *c* oxidation and the proton pumping of EYFP-COVs. RCR and pre-steady state rates of EYFP-COVs were measured with the cytochrome *c* oxidation assay. Reduced cytochrome *c* was used as the substrate. Oxidation of cytochrome *c* will cause the decay of its 550 nm absorbance. COVs were placed in one syringe of stopped-flow instrument and cytochrome *c* was placed in the other syringe. After mixing the sample with either no ionophores (controlled state) or valinomycin or valinomycin + CCCP (uncontrolled state), scans were collected (1000/s), and from the reduction of cytochrome *c* (550 nm), the rates were fit using single exponential fitting to the kinetic traces with Microcal Origin software. The results showed the same pattern and reaction rate as the WT COVs (Figure 3.10). The RCR calculated from these data is 5.5, which is also consistent with the results of oxygen consumption assay (Table 3.2).

Proton pumping measurements of EYFP-COVs were also performed. In this experiment the EYFP is used as a pH indicator inside the vesicles. In the measurement, the excitation wavelength was set at 515nm. Fluorescence emission changes were measured at 525nm. The results are shown in Figure 3.11 .The result showed an increase in the fluorescence level at the beginning of the controlled state. After adding valinomycin into the system, the level of this increase was faster and the level was higher than in the controlled state. This increase indicated the alkalinization due to the proton uptake catalyzed by the C*c*O. A similar result was seen with the wildtype CcO reconstituted with the pyranine dye on the inside of the vesicle.

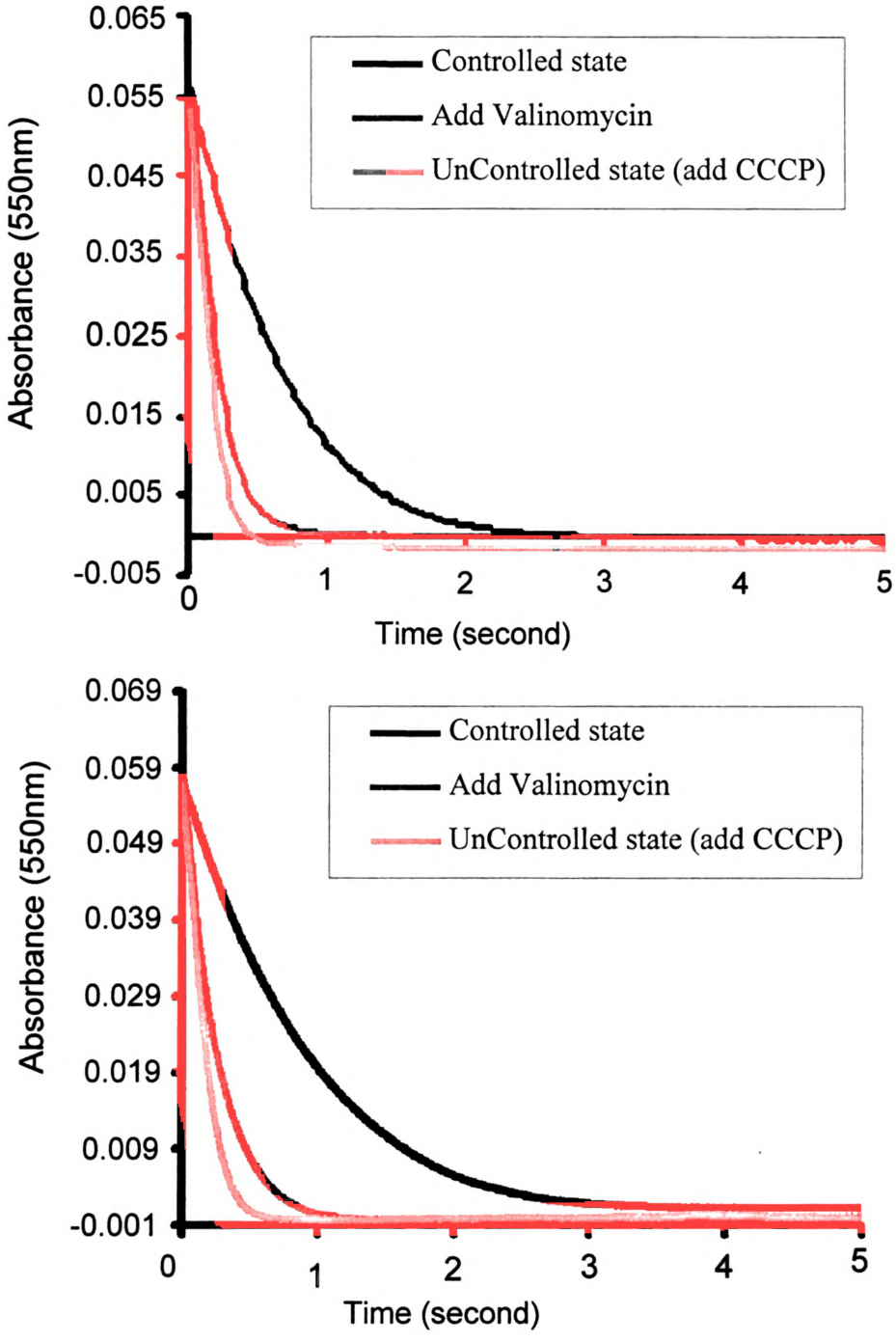

Figure 3. 10: Cytochrome c oxidation by WT COVs and CcO-EYFP COVs.
A: WT-COV. **B** 4: *Rs*C*c*O-EYFP COV. For the assay, 2 μM of cyt c^{2+} was mixed with 0.04 μM of oxidase in the COVs (Inside buffer: 50mM HEPES-KOH, pH7.4 +43 mM KCl). Data scans were collected (1000 scans/s) by Photophysics stopped flow apparatus.

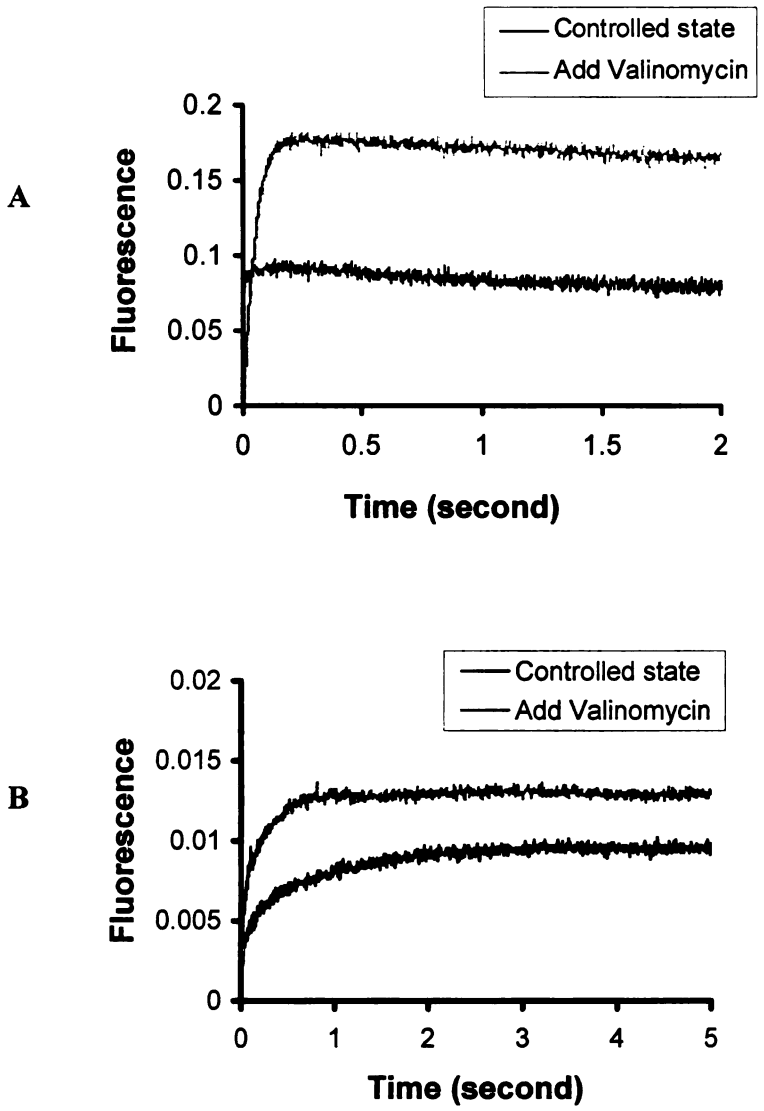

Figure 3. 11: Proton pumping by *Rs*CcO-EYFP COVs
A: WT COV, fluorescence dye pyranine was used inside vesicles. **B: *Rs*CcO-EYFP COV,** the EYFP in the fusion protein is used as pH fluorescence detector inside vesicles. The Data scans were collected (1000 scans/s) by Photophysics stopped-flow apparatus. For EYFP-COVs, the fluorescence is and detected at 525 nm. For the wild type COVs, the fluorescence is excited at 465 nm detected at 510nm.

3. Discussion

The C*c*O-EYFP protein has been expressed in *R. sphaeroides* and purified. The attached EYFP is soluble and increases the hydrophilic portion of C*c*O. Preliminary crystallization was also performed on this fusion protein. Although some small crystals were formed, no diffraction was observed with these small crystals. There are several possible reasons:

(a) Subunit I-EYFP protein was partially degraded during the purification. After the DEAE 5PW purification, most of the truncated protein was separated from the full-length protein. However, SDS-PAGE showed that there is still some truncated form of subunit I-EYFP in the purified protein (Figure 3.8C). This impurity and non-homogeneity of the enzyme might have undermined the crystallization. An improved the purification method or engineering a more stable fusion protein will be useful in solving this problem.

(b) EYFP has likely changed the hydrophilic/hydrophobic character of C*c*O. The crystallization conditions such as concentration of detergent or precipitant reagents and types of detergent may need to be changed and optimized.

(c) Although EYFP may have increased the hydrophilic interaction between protein molecules, the new domain is only attached by one linkage and that is likely to be flexible so that the new domain does not help to make a stable crystal contact. Inserting the EYFP into the C*c*O by two attachments might help reduce the flexibility of the construct.

My results showed that the C*c*O-EYFP reconstituted vesicles had similar activity and RCR as the wild type C*c*O vesicles. Another key question is, can EYFP be used as a pH indicator inside the vesicles? To answer this question, fluorescence stopped-flow was performed to investigate the pH sensing ability of the EYFP-COVs. In the COVs, the environments of inside and outside of the vesicles are separated. Thus the pH and electrochemical potential

changes caused by the proton pumping can be observed independently and quantified. For the *Cc*O-EYFP fusion protein, EYFP could act as a pH sensor to investigate the pH changes inside the vesicles. Proton pumping will cause the pH to increase inside the vesicles, so we would expect to see an increase in fluorescence signal due to this change. At the beginning of the controlled state, the proton will be pumped out from the inside of the vesicles. For each catalytic cycle, four protons will be used to react with O_2 and 4 more protons will be pumped out. However, after the transmembrane potential is built up, the proton pumping is constrained, and the rate of alkalinization inside the vesicle will be slowed down until a balance is reached. After adding valinomycin, the transmembrane potential of COV is dissipated and more protons will be taken up for substrate and to be pumped out (Figure 3.11). The experiment results are consistent with this postulate. Furthermore, comparing the data of cytochrome *c* oxidation and proton pumping, we find that the reaction rate and the proton pumping are also co-related (Figure 3.10 and Figure 3.11). Since the results obtained with the modified *Rs*C*c*O-EYFP were similar to the results obtained with the WT C*c*O, but with lower signal to noise, the concept of using the *Rs*C*c*O-EYFP as a internal pH monitor appears feasible. However, there is clearly a need for larger vesicles that hold more protein and hence give a stronger signal. Our lab has developed several methods to do this (Dr.Namjoon Thesis; Hiser, personal communication) which will be tested in the future to see how robust this method might be.

4. Summary and Conclusions

An *Rs*C*c*O-EYFP fusion protein was produced and expressed in *Rs* strain. The purpose is to increase the hydrophilic portion of *Rs*C*c*O and form better crystal contacts. The results

showed that the fusion protein was fully active. The cytochrome *c* oxidation rate and proton pumping ability of this fusion protein is very similar to that of WT C*c*O, suggesting that the fusion of EYFP did not affect the normal function of the enzyme.

The reconstitution of the fusion protein into liposome vesicles was successful and fluorescence changes could be observed according to the pH changes inside the vesicles. The fluorescent signal was still weak for accurate proton pumping measurement, better conditions still need to be developed, such as making of larger vesicles, lower internal buffering capacity etc.

Extensive crystallization screening on this fusion protein was also performed, however, no evidence that the fusion helped crystallization. This result could due to the partial proteolysis of the fusion protein, suggesting a two-site attachment would be worth trying in the future, given the close positioning of the N and C terminals of EYFP.

CHAPTER 4. STUDY OF THE SUBUNIT I C-TERMINUS MUTANT FORMS

1. Introduction

Following the first successful crystallization of the four subunit C*c*O from *Rhodobacter sphaeroides*(Svensson-Ek et al. 2002), neither the Swedish group nor our group were able to reproduce the level of resolution initially achieved (2.3-2.8 Å, anisotropic, in only one crystal) in spite of several years of effort in both groups. Our success in producing a new, reproducible, high resolution (2.0 Å, isotropic, Qin et al., 2006) crystal form that contained the two core catalytic subunits did not obviate the need to continue our efforts to obtain a better four subunit structure.

Previous studies have shown that removal of the flexible portions of certain proteins can help the protein crystallize or improve the crystal quality to get better diffraction data

The last 16 amino acids of the C-terminus of *Rs*C*c*O subunit I are not observed in the 2-subunit crystal structure, indicating this end may be flexible in nature. In the 4-subunit crystal of *Rs*C*c*O, 6 amino acids are missing (Figure 4.1). This apparently flexible end might interfere with the crystal contact formation as mentioned in Chapter 3. A possible solution is to use molecular engineering to remove the flexible portion of subunit I, to create a new C-terminus with new crystal contacts, and improve crystal quality. This region is not highly conserved, adding to the likelihood that its removal may not disturb the function of *Rs*C*c*O.

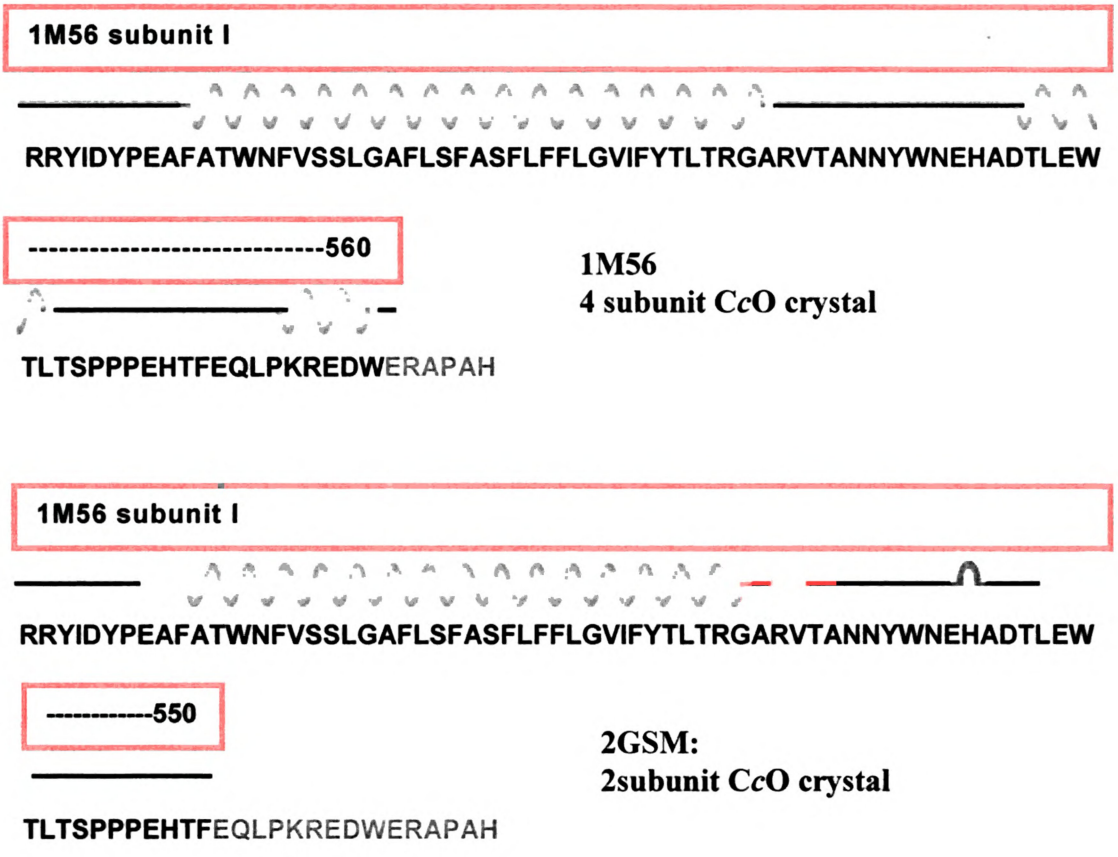

Figure 4. 1: C-terminus comparision of 4-subunit *Rs*C*c*O crystal and 2-subunit C*c*O crystal.

These results are from the crystal structures of *Rs*C*c*O 1M56 and 2GSM. In structure 1M56 (4 subunit crystal of *Rs*C*c*O), last 6 amino acids of C-terminus of subunit I were not defined (blue letters). In crystal structure 2GSM (2 subunit crystal of *Rs*C*c*O), last 16 amino acids of subunit I C-terminus were defined (blue letters, and the F551 is always poorly defined). These residues could be very flexible in the structure.

Anther potential problem for crystallography is subunit III of *Rs*C*c*O, a highly hydrophobic transmembrane subunit with some tendency to be lost during purification. The 4-subunit crystal structure of *Rs*C*c*O shows that it has multiple lipids bound (Svensson-Ek et al. 2002) and could be very flexible in the structure. It is possible that the instability and partial loss of subunit III is another factor that affects the crystal quality of *Rs*C*c*O. Crystallization results of 4-subunit and 2-subunit crystals of *Rs*C*c*O are consistent with this hypothesis. The 2-subunit crystal of *Rs*C*c*O, which does not contain subunit III or subunit IV, has consistently higher resolution (routinely 2.0~2.5 Å) compared to the 4-subunit crystal of *Rs*C*c*O (routinely 2.9~3.5 Å). To stabilize subunit III in the 4-subunit crystal could be another way of improving the crystal diffraction quality. The known crystal structures of *Rs*C*c*O show that the C-terminus of subunit I is very close to the N-terminus of subunit III (Figure 4.2), suggesting a possible interaction between these two subunits at this region. Through molecular engineering, we can link the C-terminus of the subunit I gene to the N-terminus of the subunit III gene, to stabilize subunit III in the whole structure, preventing its loss during purification and thus improving the crystal quality of the 4-subunit crystal of *Rs*C*c*O.

In this chapter, two mutants of *Rs*C*c*O containing short versions of subunit I are described (PJL33 and PJL49) and characterized to investigate the effects of C-terminal deletions on the crystallization. A single mutant at residue E552 was also created to test the possibility that it might be responsible for observed loss of pumping in one of the shortened versions. A subunit I-subunit III fusion mutant, PJL63, was also created to study the effects of subunit III on the crystallization.

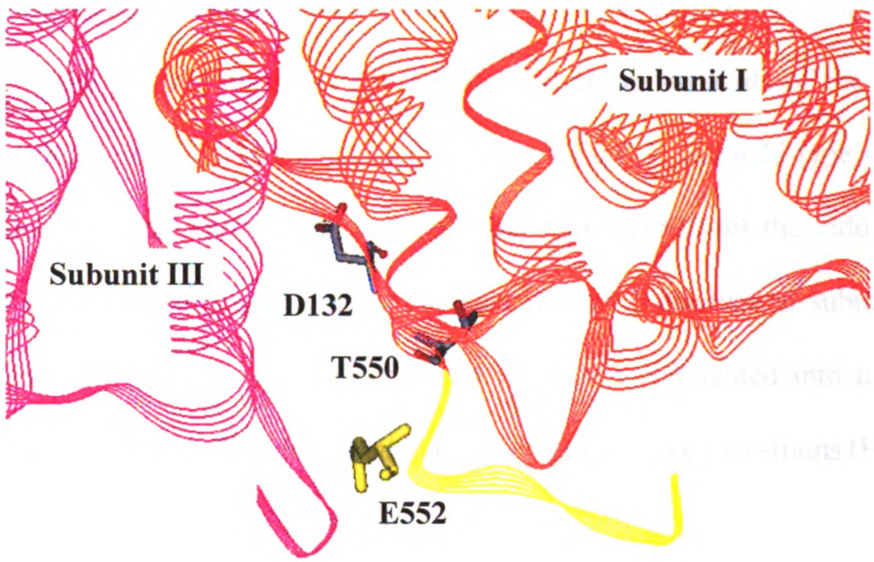

Figure 4. 2: Possible interaction between subunit I and subunit III of *Rs*C*c*O.
The subunit III is shown in purple color. The subunit I is shown in red color. The yellow colored loop end region is the C-terminus of subunit I, from residue number F551 to W560. This region could not be resolved in the 2 subunit *Rs*C*c*O due to its flexibility in the structure. The N-terminus of subunit III is very close to this region, providing the possible interactions in subunit I C-terminus.

2. Methods and Results

2.1 Construction of the short subunit I *Cc*O mutants PJL33 and PJL49

The construction of short subunit I *Rs*C*c*O mutants PJL33 and PJL49 is shown in Figures 4.3 and 4.4. In the plasmid construct pJL-33, the last 16 amino acids of the subunit I C-terminus were deleted, pJL-33 contains a his-tagged subunit II and wild-type subunit III operon (Figure 4.3) for the purification. In the plasmid construct pJL-49, the codon of E561 was mutated to a stop codon so it does not contain the last 6 residues of subunit I after translation (Figure 4.4). The plasmid constructs were then conjugated into the *R.sph* D1D4 strain by using the method described in Chapter 2 to produce two strains (PJL33 and PJL49) that express short subunit I *Rs*C*c*O.

2.2 Protein expression and purification of PJL33 and PJL49

The proteins of PJL33 and PJL49 were expressed and purified as described in Chapter 2. The reduced-minus-oxidized spectra of the membranes showed normal spectra for both PJL33 and PJL49 compared to the wild type membrane spectrum (Figure 4.5), suggesting the expression of PJL33 and PJL49 was successful. The expression level of both PJL33 and PJL49 are quite high judging from the ratio of the 550 nm peak to the 605 nm peak. The proteins of PJL33 and PJL49 were then purified with the FPLC-NiNTA column. A further purification step of a DEAE-5pw column was also performed to facilitate the *Rs*COV reconstitution.

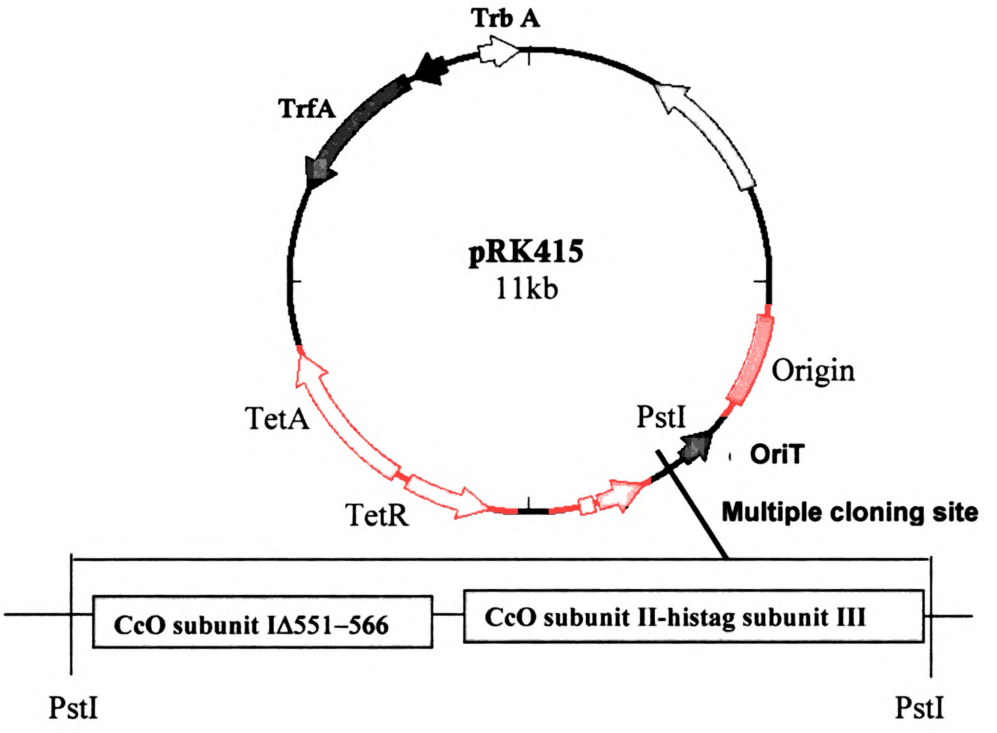

Figure 4. 3: Construction of pJL-33 expression plasmid
The subunit I gene missing the last 16 amino acids was cloned into the pRK415-1 plasmid at the Pst I site together with a fragment containing subunit II-III operon. His-tagged subunit II was in the operon and can be used to purify the enzyme with a Ni-NTA column.

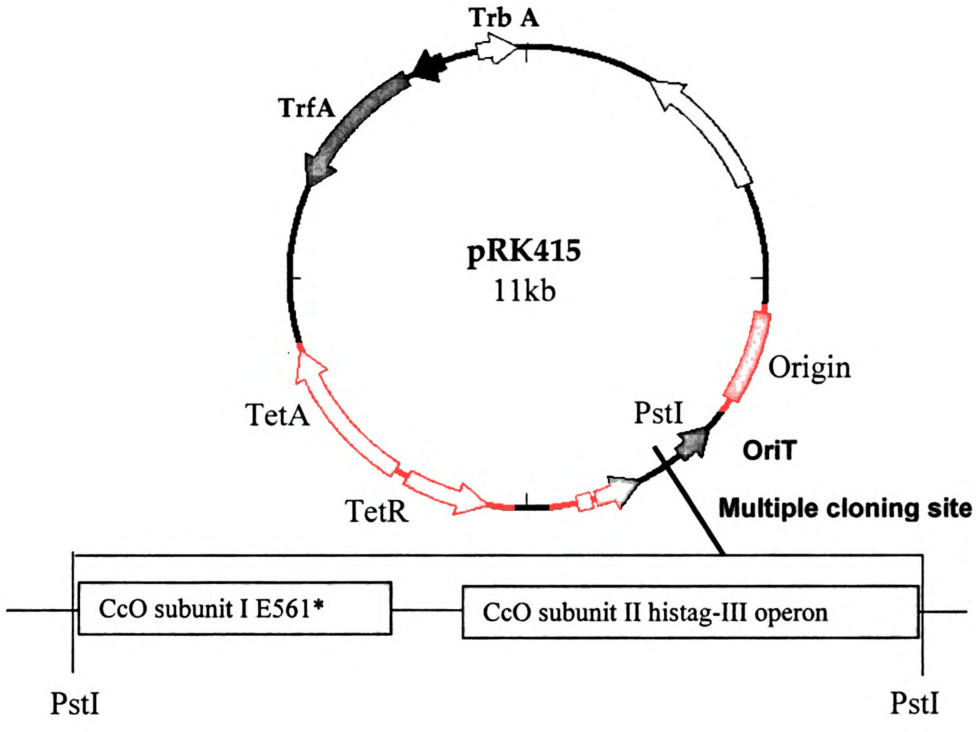

Figure 4. 4: Construction of pJL-49 expression plasmid
The subunit I E561 codon was mutated into a stop codon, so the expressed protein will be 6 residues less in C-terminus of subunit I.

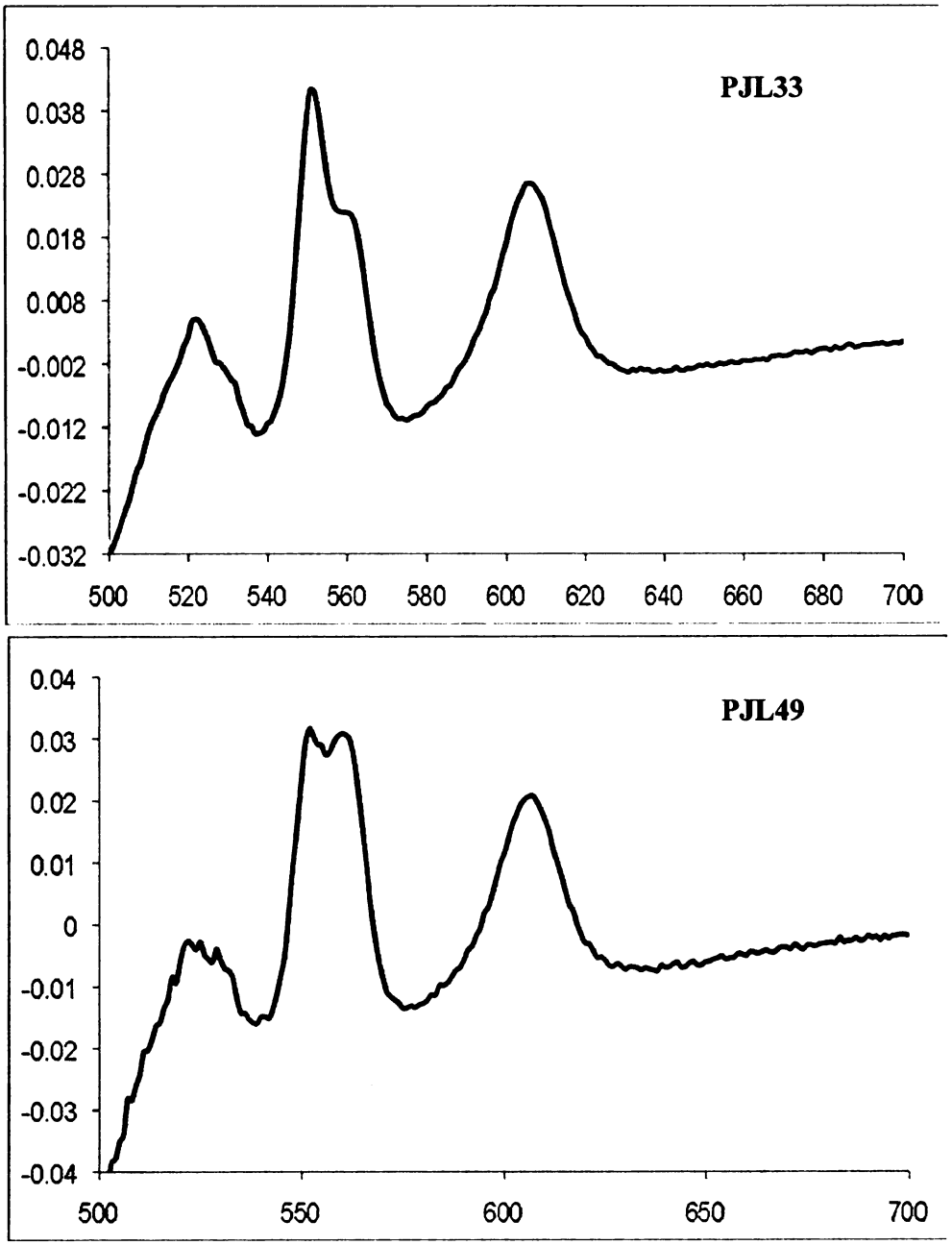

Figure 4. 5: Reduced –minus-oxidized spectrum of the membrane fraction of PJL33 and PJL49 C*c*O

The α peak (605 nm) from PJL33 and PJL49 is relatively high compared to the 550 nm bc1 complex peak, suggesting a high expression level of C*c*O in the membrane.

2.3 SDS-PAGE of purified PJL33 and PJL49 C*c*O

The SDS-PAGE was performed to verify the result of the purified PJL33 and PJL49 C*c*O (Figure 4.6). The result showed that in both PJL33 and PJL49 C*c*Os, the subunits I are shorter than the wild type *Rs*C*c*O subunit I, and the size of subunit I from PJL49 is slightly larger than the subunit I from PJL33, indicating the mutations were successful constructed in these two strains.

The SDS-PAGE also showed that in purified PJL33, the amount of subunit III was much less than the amount of subunit III from wild type C*c*O. Considering the possible interaction between the subunit I C-terminus and the subunit III N-terminus, this reduced amount of subunit III could be the result of the loss of certain residues among the 16 deleted from subunit I in PJL33, thus the loss of the interaction. However, PJL49 contained a similar amount of subunit III as wild type *Rs*C*c*O, suggesting the effects in PJL33 could be caused by the deletion of the 551 to 561 region of subunit I.

2.4 UV-vis spectra of purified PJL33 and PJL49 C*c*O

The reduced spectra of PJL33 and PJL49 C*c*O were measured as described in Chapter 3. The results are shown in Figure 4.7. The reduced spectra of PJL33 and PJL49 purified proteins were very similar to that of WT *Rs*C*c*O, with the 444nm Soret peak and the 606nm α peak, suggesting that the deletion did not affect the heme centers of *Rs*C*c*O.

2.5 Activity of PJL33 and PJL49

The steady state activities of purified PJL33 and PJL49 proteins were measured over a range of pH conditions. The method used was described in Chapter 2. The results are

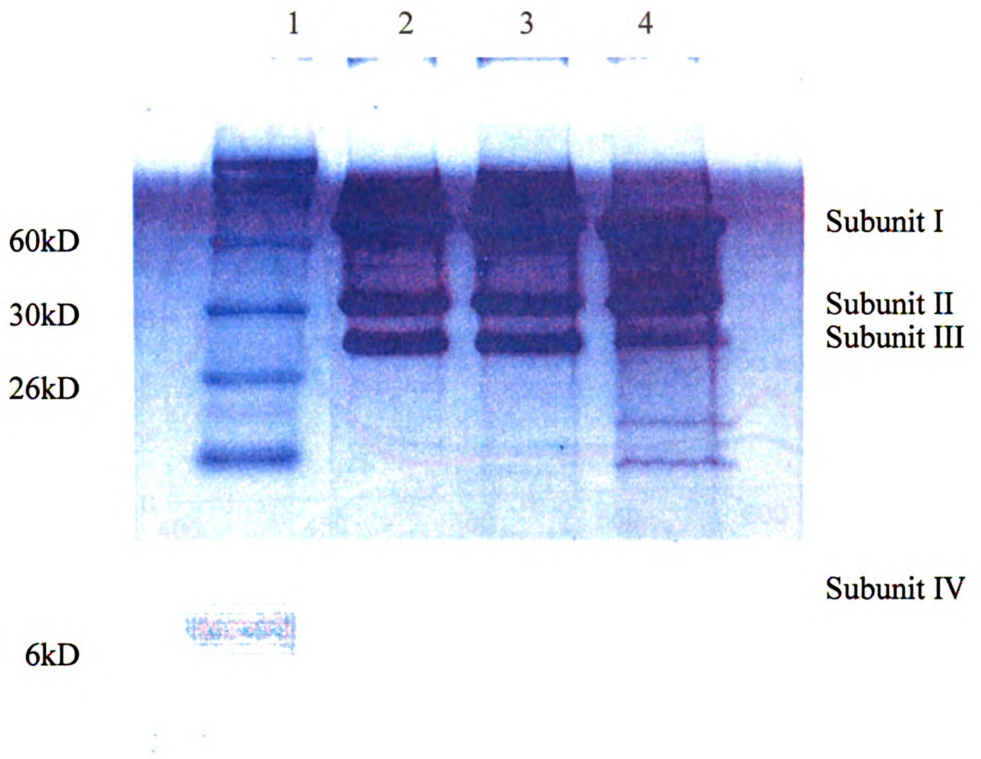

Figure 4. 6: SDS-PAGE of FPLC purified PJL33 and PJL49 protein
Lane 1: NEB protein ladder
2: W.T C*c*O (Full length subunit I)
3: PJL49 (6 residues deletion subunit I)
4: PJL33 (16 residues deletion subunit I)
18 % urea SDS-PAGE

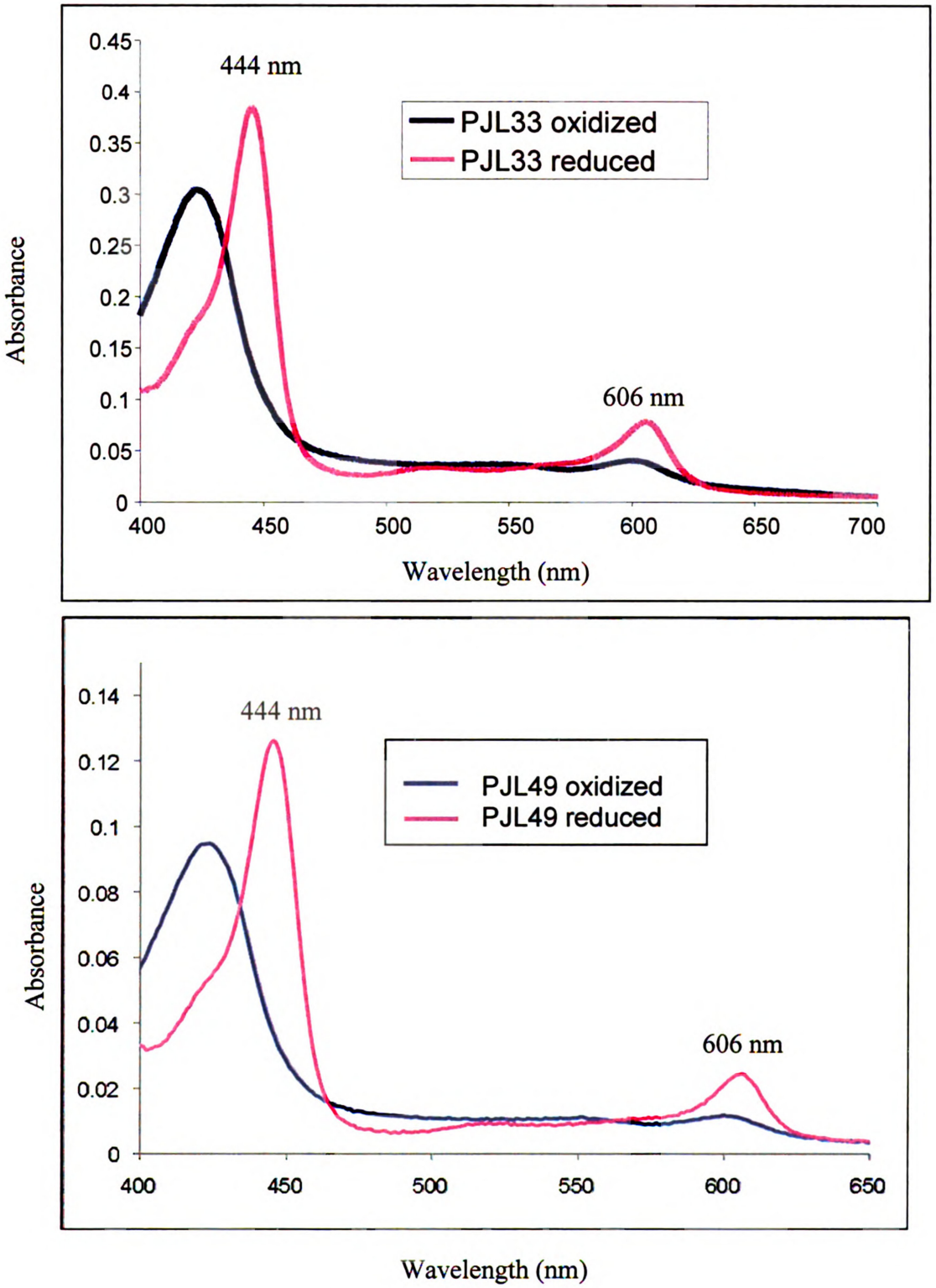

Figure 4.7: Spectrum of FPLC purified PJL33 and PJL49 C*c*O
The reduced spectrum of purified PJL33 and PJL49 C*c*O showed the normal soret peak (444 nm) and α peak (606 nm), suggesting normal redox centers in both proteins.

shown in Figure 4.8. Compared to the wild type *Rs*C*c*O, the mutant PJL33 had much lower activity, especially at the high pH region. In the low pH region, the activity of PJL33 was about 60% of wild type enzyme activity. In the high pH region, the activity of PJL33 was only 30% of wild type. Also, as the pH increased, suicide inactivation was observed during the reaction (Figure 4.9) evidenced by the slowing of the turnover rate during the assay. Unlike the 16-residue deletion construct PJL33, the overall activity of PJL49 is at the same level as the wild type *Rs*C*c*O. No suicide inactivation was observed in the enzyme reaction of PJL49.

2.6 Proton pumping assay results of PJL33

To further study the characteristics of PJL33, the pre-steady state activity and proton pumping ability were also investigated. The stop flow results are shown in Figure 4.10 and Figure 4.11. In the cytochrome *c* oxidation assay, the PJL33 showed a slower reaction rate when a membrane potential was present across the COV membrane (controlled state) as shown in Figure 4.10. When valinomycin and FCCP were added to eliminate the transmembrane potential, the reaction rate increased, similar to wild type enzyme behavior, showing the phenomenon of respiratory control. The pH change outside the COVs was measured with phenol red, which indicates proton concentration changes on the outside of the membrane. From the experimental results, the proton pumping ability of PJL33 COVs is much lower than that of wild type COVs (Figure 4.11). The loss of activity could be the result of losing key residues in the 551-566 region of subunit I. There are several conserved residues in this region, such as E548 and E552. However, the result of the mutation or deletion of these residues is still unknown.

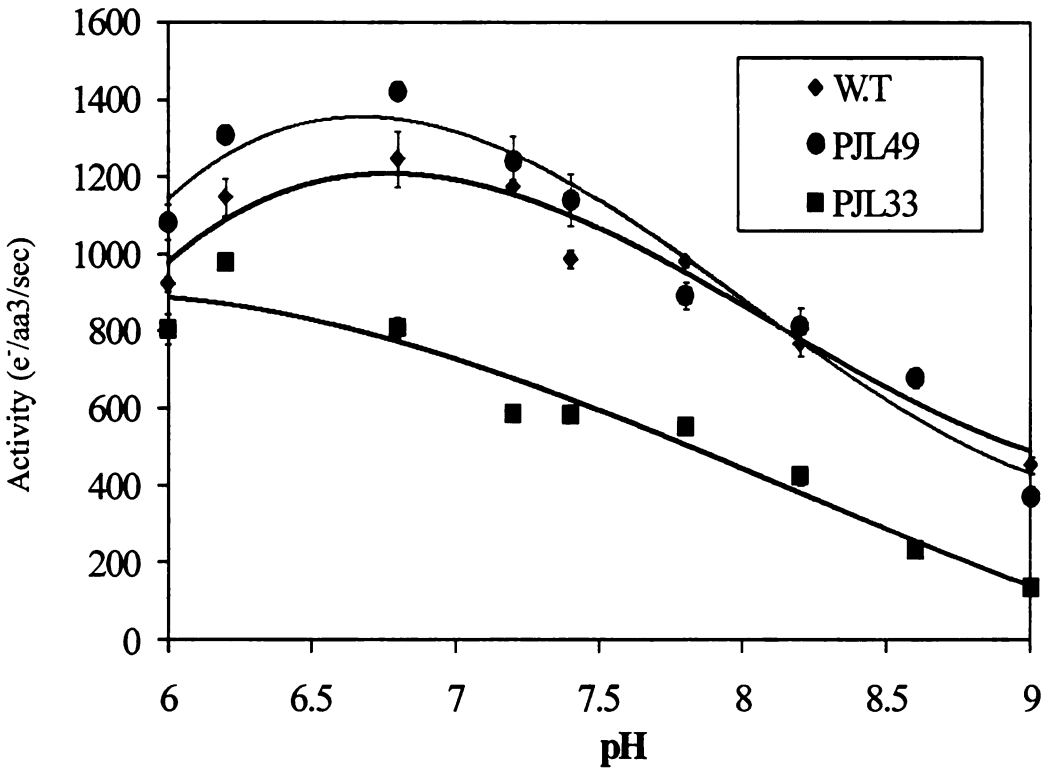

Figure 4. 8: Activity curve of PJL33 and PJL49 compared to WT C*c*O
The maximum turnover number (molecular activity) of C*c*O was measured polarographically by using a Gilson model 5/6 H oxygraph at 25 °C in a reaction medium containing a series of buffer with different pH, in the presence of 0.05 % DDM, 2.8 mM ascorbate, 0.55 mM TMPD (tetramethyl phenylene diamine) and 30 μM of horse cytochrome *c*.

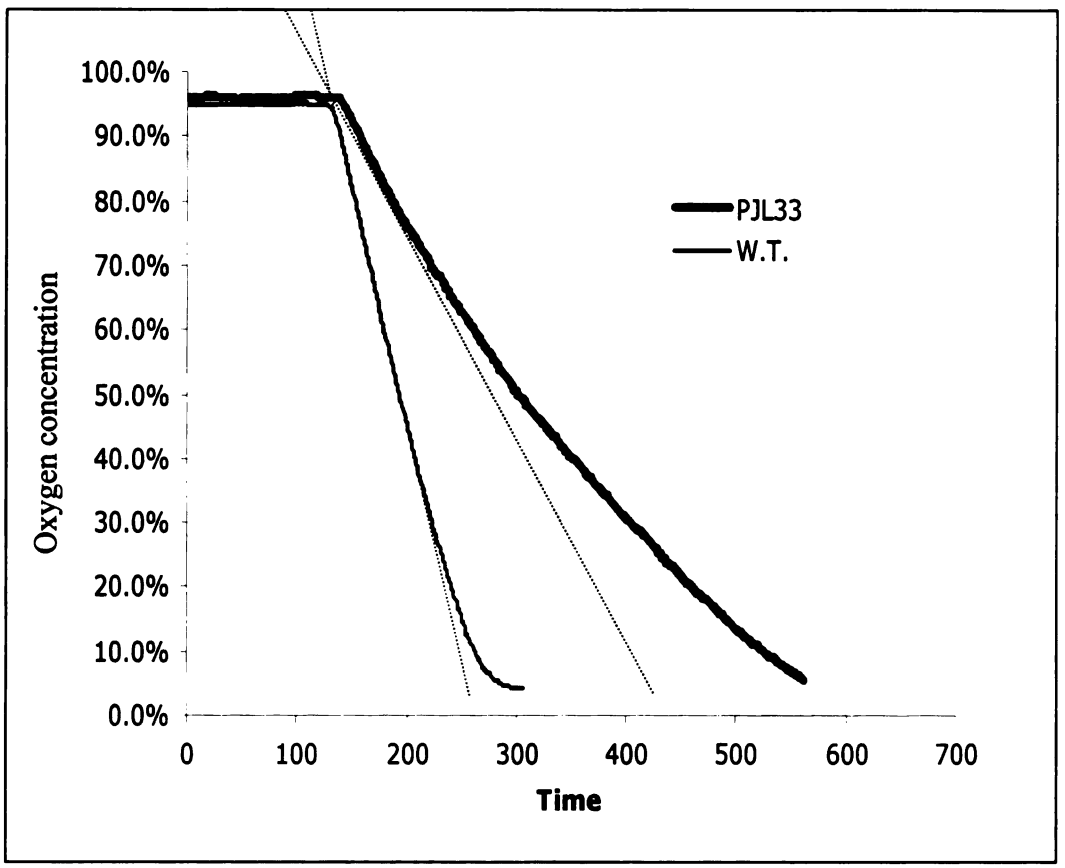

Figure 4. 9: Suicide inactivation of PJL33 C*c*O

The blue curve is the oxygen consumption by WT C*c*O in the Gilson model 5/6 H oxygraph reaction. The black curve is the the PJL33 C*c*O reaction curve. The dotted line is the initial reaction rate of the enzymes. It shows that, as reaction proceeds, the activity of PJL33 C*c*O is quickly reduced. This is always observed in the subunit III less C*c*O.

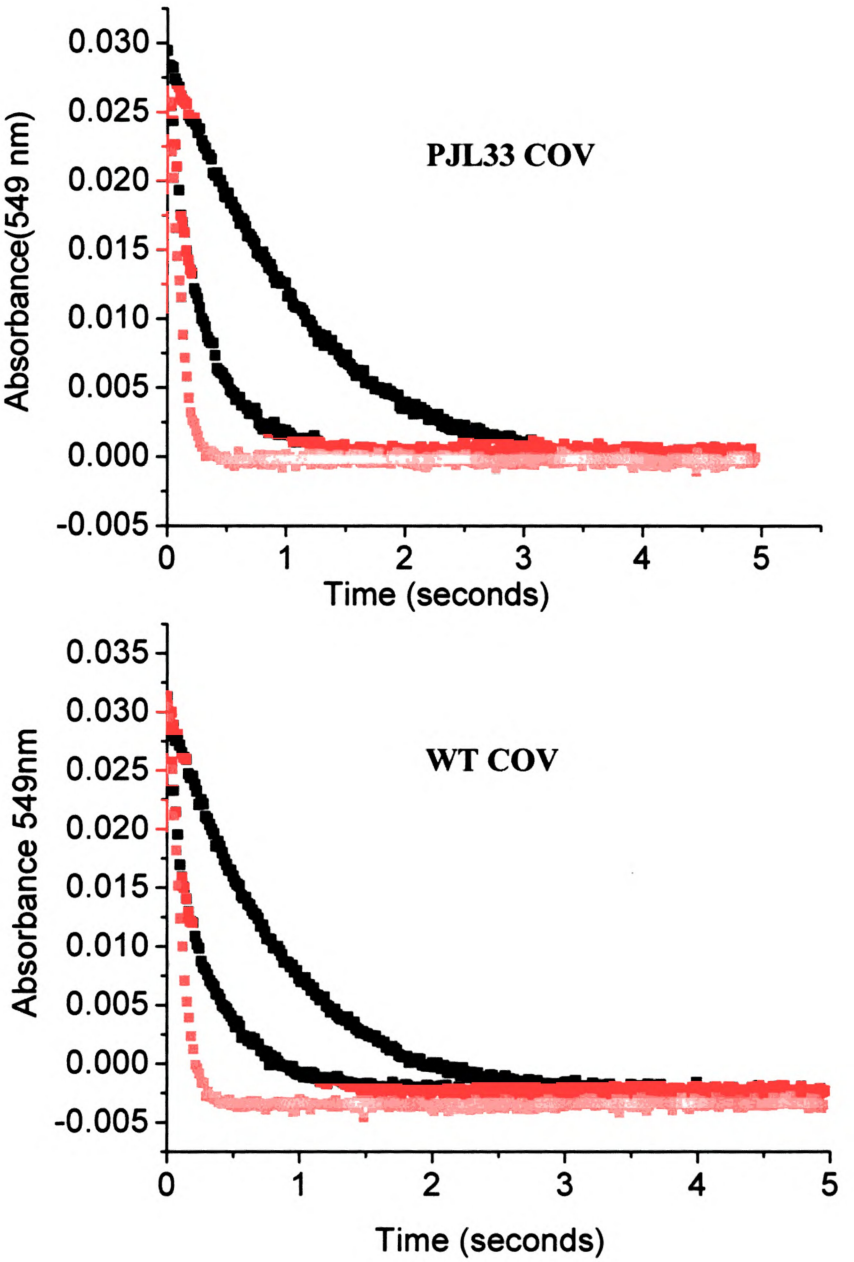

Figure 4. 10: Cytochrome *c* oxidation of PJL33 COVs measured by stopflow.
The curves were created by measuring the absorbance change of cytochrome *c* at 549 nm during the reaction.The black curve is the controlled state. The blue curve is the reaction after valinomycin was added, and the red curve is the reaction after CCCP was added, which is the uncontrolled state.

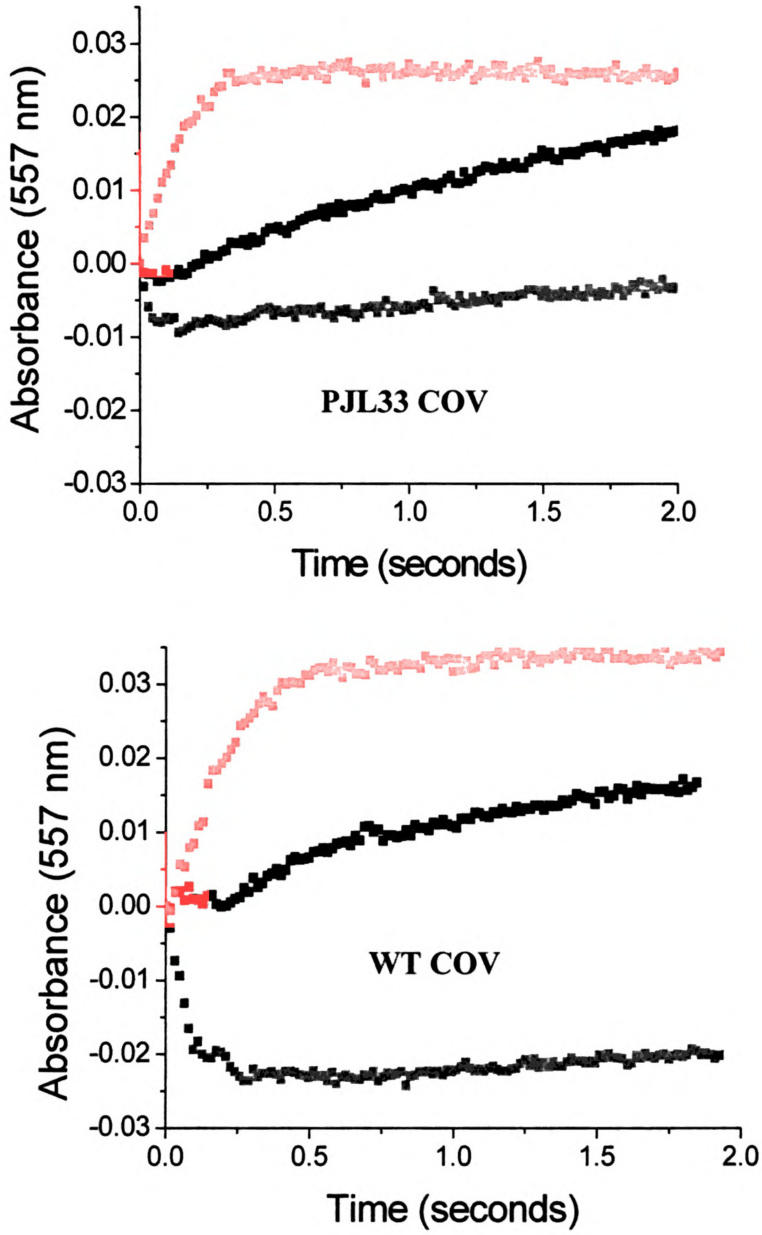

Figure 4. 11 Proton pumping assay results of PJL33 COV and WT COV.
The black line is the controlled state. The blue curve is measured by the absorbance changes after valinomycin was added. Less change in PJL33 COVs blue curve suggest that the proton pumping was impaired. The red curve is the uncontrolled state, measured by adding FCCP.

2.7 Construction of subunit I C-terminus single mutant E552A

To further investigate the reason for the loss of activity and proton pumping in PJL33, a single mutant E552A was also created. The mutation was first made on the plasmid PJS3-SH using the Qiagen QuikChange kit. The PCR primers that were used for the mutagenesis are shown in Figure 4.12. The E552 of the subunit I was mutated into an alanine. After the mutation, a fragment containing subunit II-III operon gene was inserted into the Pst I site on PJS3-SH to form plasmid pJL-44. The DNA fragment containing subunit I with the E552A mutation and the subunit II-III operon was then ligated into pRK415-1 to form the expression plasmid pJL-45. pJL-45 was then conjugated into the *R.sph* strain Δ123 as described in Chapter 2.

2.8 Expression and purification of E552A

E552A protein was expressed and purified as described in Chapter 2. The membrane fraction reduced-minus-oxidized spectrum (Figure 4.13) showed the normal spectrum like WT *Rs*C*c*O. The oxidized and reduced spectra of purified E552A protein are shown in Figure 4.14. The reduced spectrum showed a normal Soret peak at 444 nm and alpha peak at 606nm. These results suggested that the heme centers in the enzyme were not disrupted by the mutation of E552 to A552.

2.9 Activity assay of E552A

The steady state activity of purified E552A protein was measured using the same method as used in Chapter 2. The result (Table 4.1) showed E552A is fully active at pH 6.5 and pH 8.6. No suicide inactivation was observed during the E552A reaction.

Upper primer:

CCGGAGCATACGTTC**GCG**CAGCTTCCCAAGCGG

Lower primer:

CCGCTTGGGAAGCTG**CGC**GAACGTATGCTCCGG

Figure 4. 12: Primers used in the construct of PJL34: E552A mutant.
The underlined GCG and CGC show the mutation from gluatmic acid codon to alanine codon.

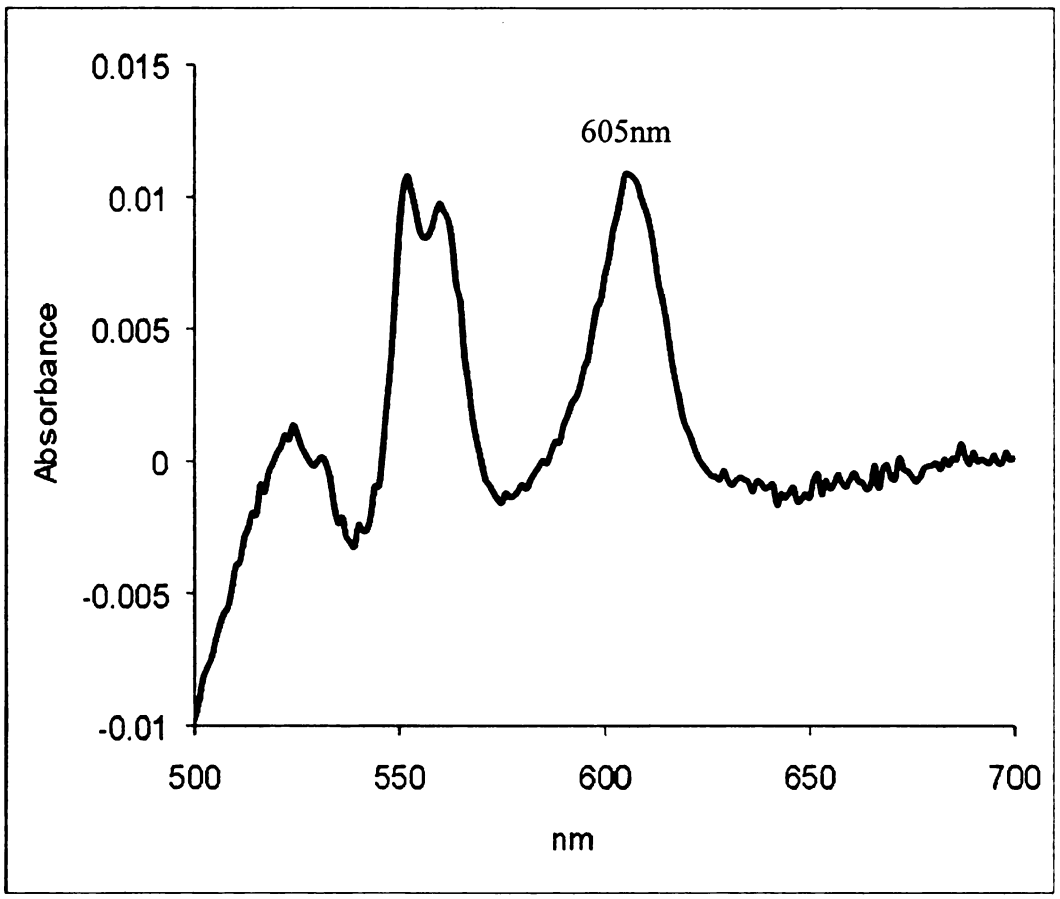

Figure 4. 13: Reduced minus oxidized spectra of PJL45 membrane fraction.
The normal 605 nm peak and high 605 nm/550 nm ratio suggest that PJL45 was highly expressed in the membrane.

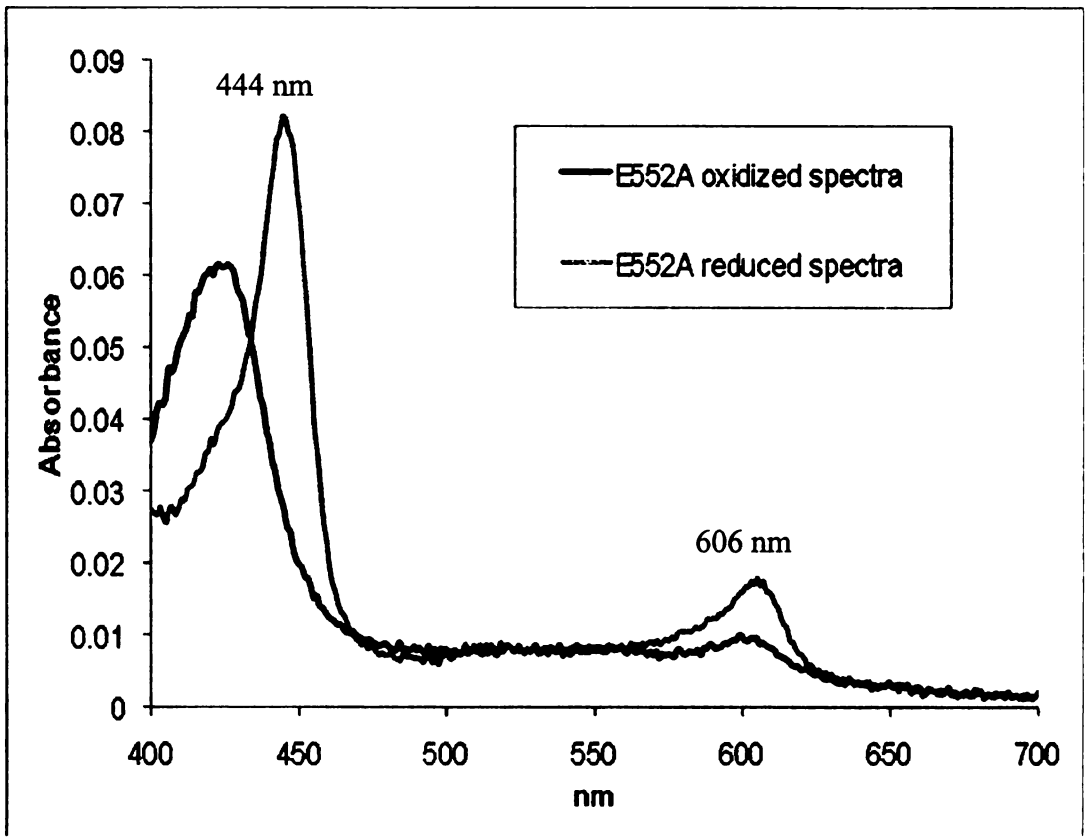

Figure 4. 14: Spectra of purified PJL45 C*c*O.
Purified PJL45 C*c*O (E552A) shows the normal 444 nm Soret peak and 606 nm α peak, indicating the redox centers in PJL45 C*c*O were not affected by the E552A mutation.

	pH 6.5	pH 8.6
WT *Cc*O	1248 (±200)	960 (±210)
PJL45 (E552A)	1200 (±280)	848 (±250)

Table 4. 1: Activity of PJL45 *Cc*Oat pH 6.5 and pH 8.6
Acitivty was measured by oxygen consumption with purified PJL45 protein.
Activity Unit: (e^-/sec/aa_3)

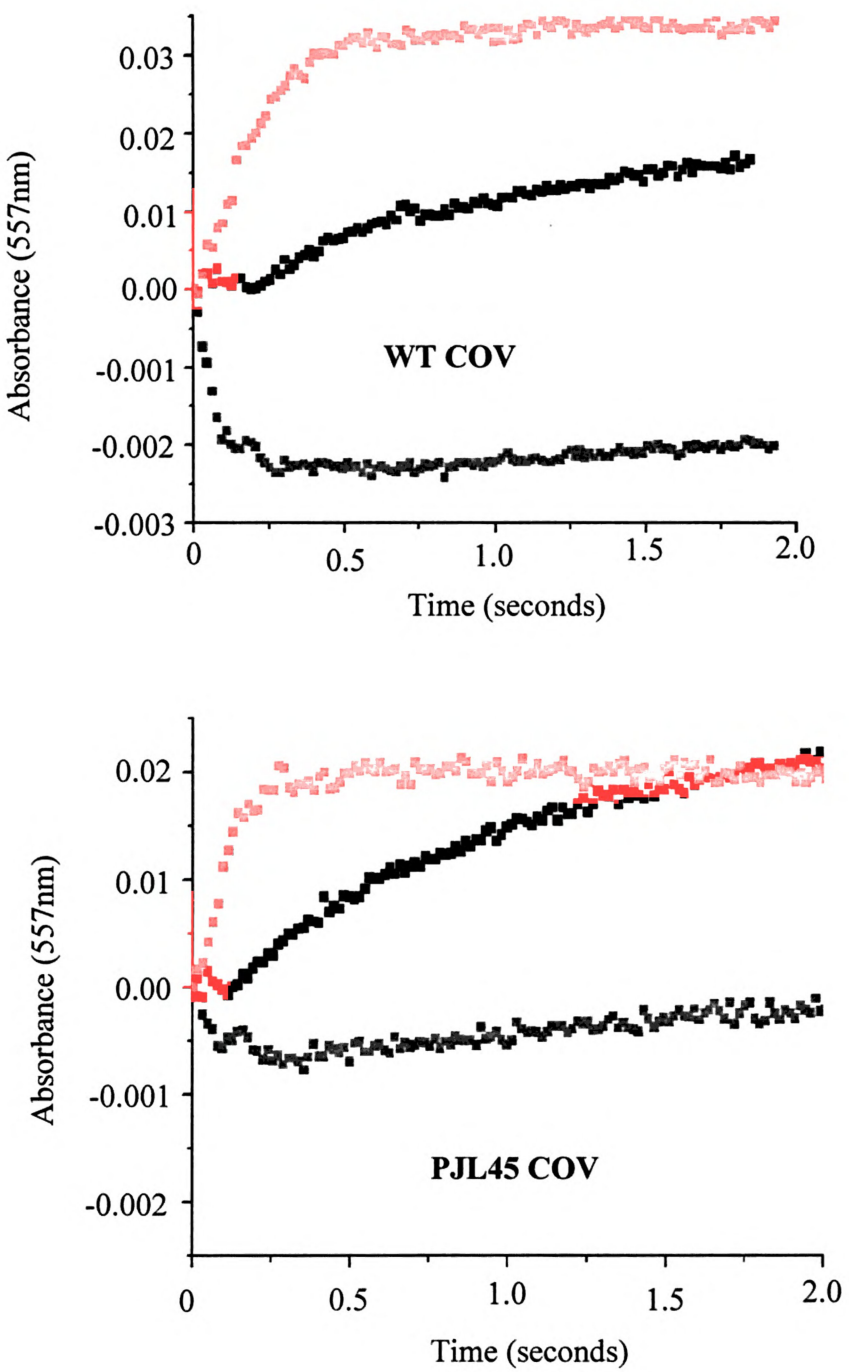

Figure 4. 15: Proton pumping assay of PJL45 COV.
Black: controlled state. Blue: Valinomycin added. Red: FCCP added, uncontrolled state. PJL45 COV (lower chart) showed less proton pumping compared to WT COV (upper chart).

E552A was also reconstituted into vesicles using the methods described in Chapter 2. The proton pumping ability of E552A was measured by stop-flow and compared with WT *Rs*C*c*O. The results are shown in Figure 4.15. From the results we can see that the proton pumping ability of E552A COVs was slightly impaired compared to that of WT COVs. However, more experiments are still needed to comfirm this result since the instability of the proton pumping measurement in COVs.

2.10 Crystallization of PJL33 and PJL49

Both 4-subunit and 2-subunit crystallization conditions were tried on the purified PJL33 and PJL49 proteins. There were no crystals of PJL33 and PJL49 formed under the 4-subunit crystallization conditions. However, purified PJL33 could be crystallized with 2 subunit crystallization conditions. Six μl of enzyme solution containing 10 mM Tris, pH 8.0, 50 mM NaCl, 0.20% decyl maltoside and 120 μM C*c*O was mixed with 3 μL of reservoir solution containing 100 mM MES, pH 6.3, 27% PEG-400 and 3 μl of crystallization additive solution containing 5% heptanetriol, 32 mM $MgCl_2$, 1.3 mM $CdCl_2$ and 0.026% dodecyl maltoside. Two subunit crystals of PJL33 were observed after 3 days growing under 4°C incubation. After two weeks, the crystals of PJL33 were collected and examined at Argonne National Lab. The best resolution of the crystals is 2.1 Å (Table 4.2). Two-subunit crystals of PJL49 were also obtained under the sitting drop condition with slightly different conditions: well solutions containing 100 mM MES, pH 6.3, 27-29% PEG-400. The drop also contained 1.3% heptanetriol, 8 mM $MgCl_2$, 0.4 mM $CdCl_2$ and 0.06% dodecyl maltoside. The best resolution of the crystal of PJL49 is 2.5 Å (Table 4.2)

PJL33	PJL49
A. Unit cell parameters	
Space group: $P2_12_12_1$	Space group: $P2_12_12_1$
Cell dimension:	
α=123.005 β=130.000 γ=177.539	α=124.905 β=131.477 γ =176.601
x=y=z=90.00	x=y=z=90.00
Molecules per A.U. : 2	Molecules per A.U. : 2
B. Data collection:	
Resolution range: **50.0-2.10 Å**	Resolution range: **50.0-2.50 Å**
Completeness: 99%	Completeness: 95%
Number of unique reflections: 165884	Number of unique reflections: 117531
Redundancy: 7.3	Redundancy: 5.7
Rmerge=7	Rmerge=4
C. Structure refinement	
R factor/R_{free}: 23.8/25.5 (%)	R factor/R_{free}: 26/28.3 (%)
RMSD bond length: 0.008Å	RMSD bond length: 0.022Å
RMSD bond angle: 1.34	RMSD bond angle: 1.97
B-Factor: 45.4	B-Factor: 52.3

Table 4. 2: Crystal parameters of PJL33 and PJL45 C*c*O

2. 11 Crystal structure of PJL33

Although the crystal of PJL33 has a similar space group ($_P2_12_12_1$) as the wild type *Rs*C*c*O 2-subunit crystals, the cell dimensions of the crystals are slightly different from that of wild type crystals (Table 4.2). This might be caused by the deletion which affected the crystal packing. Thus molecular replacement, instead of rigid body refinement, was performed to get the right phase information of this crystal. After several refinements, we can see that the overall structure of this mutant is not much different from wild type enzyme. The positions of important redox centers remain unchanged (Figure 4.16). The major structural changes in the PJL33 were found in the T550 region (Figure 4.17). From the crystal structure, we can see that in WT, there are 2 waters bound between T550, H26 and K27, while the distance between these 2 waters is very close (2 Å), indicating one of them could be a metal ion such as Mg or Cd. (More experiments are still needed for this hypothesis.). In PJL33, the loss of the last 16 residues on subunit I make the T550 the new C-terminus. The waters between T550 and H26 are gone. The T550 sidechain has now folded in closer to the H26, forming a hydrogen bond between them. This region is very close to the entrance of the D-pathway at residue D132. (Figure 4.17). The changes in this region, including the loss of the waters (or metal) and direct interaction between T550 and H26, could change the pKa of residues in the environment of the entrance of D-pathway which could explain the altered pH dependence of activity and reduced proton pumping of this mutant. Comparing this structure with wild type *Rs*C*c*O and other mutant structures will help us to further understand the regulation of the D-channel in enzyme function and the proton pumping mechanism.

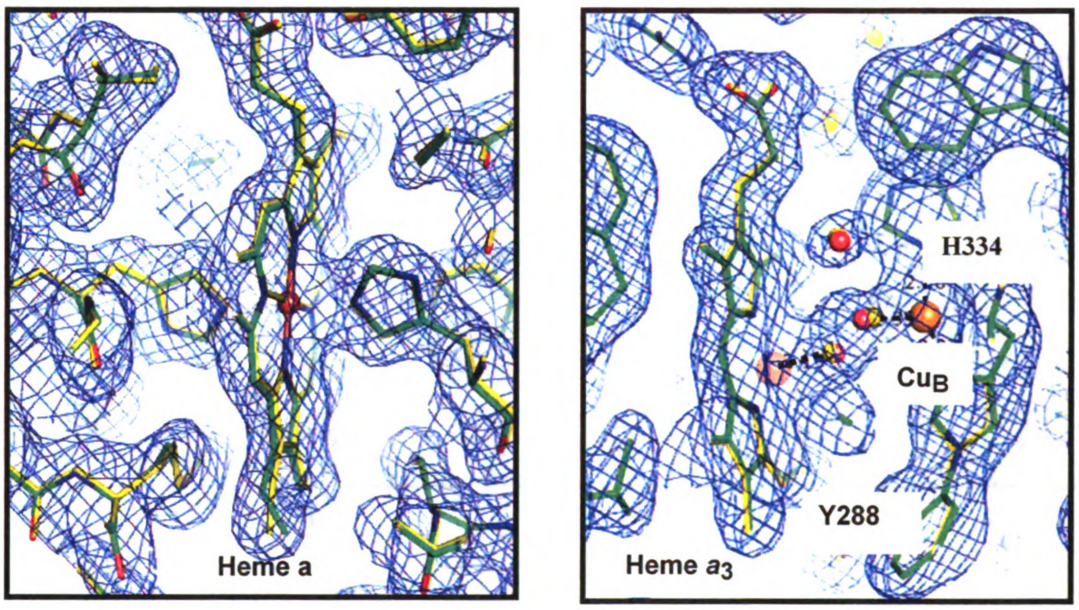

Figure 4. 16 Structure alignment of the redox centers of PJL33 with WT *Cc*O
PJL33 structre are shown in green color. The yellow structure is the WT CcO structure (2GSM). (Blue and red are the nitrogen atoms and oxygen atoms respectively)

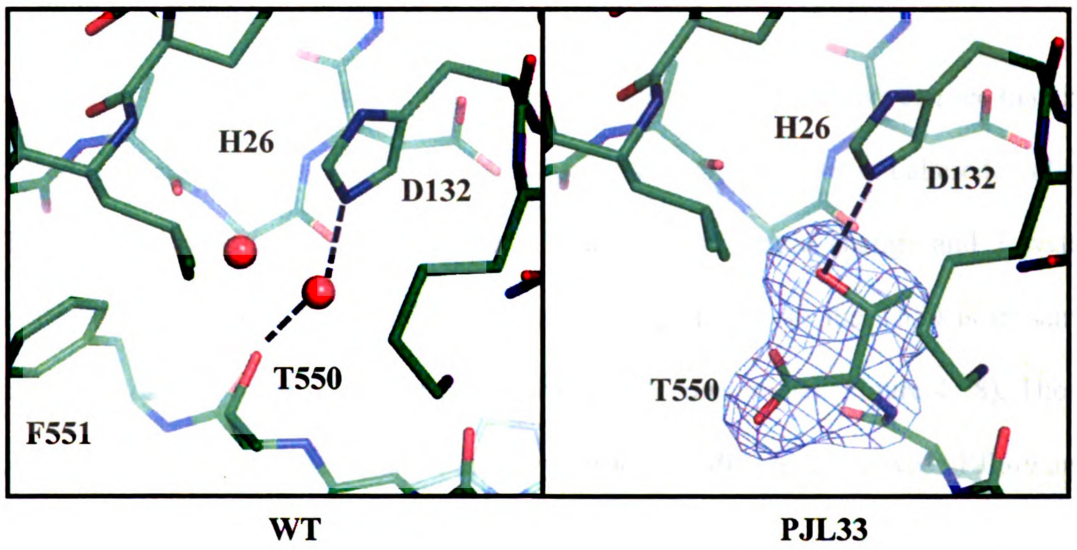

Figure 4. 17: Structure comparsion of PJL33 and WT C*c*O at C-terminus region
The waters are rendered in red spheres. The 2fo-fc map (blue mesh) showed that the mutation in PJL33 makes the T550 became the new C-terminus of subunit III, with the loss of the waters in between H26 and T550. A new hydrogen bond interaction was formed between H26 and T550 directly.

2.12 Crystal structure of PJL49 C*c*O

The 2-subunit crystals of PJL49 C*c*O were examined at LS-CAT at Argonne National Lab and the best of them could diffract to 2.50Å (Table 4.1). The overall structure of PJL49 is very similar to the WT C*c*O structure. It has the same space group ($p2_12_12_1$), similar unit cell dimensions and crystal contacts. After a few rounds of refinement, we can see that the main metal centers of this mutant, heme *a* and the heme a_3-Cu_B site, are not altered. Unlike the T550 region of PJL33 where there is a significant structural change and 2 water molecules that bonded to T550 and H26 were missing, in PJL49 the T550 is in same conformation as wild type C*c*O, as are the 2 water molecules /metal (Figure 4.18). These structural differences could account for the enzyme activity difference between PJL49 and PJL33.All these results showed that PJL49, having lost the last 6 residues from subunit I, is almost the same as wild type C*c*O in the aspects of enzyme activity and structure. This cut off site does not affect the normal function of wild type C*c*O and likely provides a more stabilized C-terminus. It can therefore be used for a new construct of C*c*O with a gene fusion to potentially get better crystal contacts and higher resolution.

2.13 Construction and Preliminary study of the subunit I-III fusion protein : PJL63

An expression plasmid, pJL-63 was constructed to express the subunit I C-terminus subunit III-N-terminus fusion mutant. The C-terminus of subunit I (ending in residue 561) and the N-terminus of subunit III gene (starting from residue 6) were linked together by PCR. A subunit II gene with his-tag was also cloned into the pJL-63 plasmid construct.

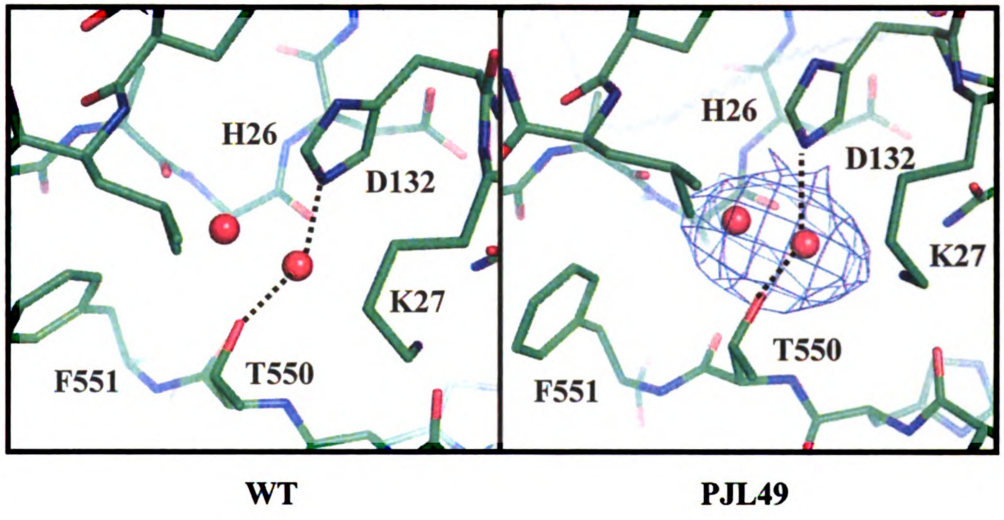

Figure 4. 18: Structral comparison of the C-terminus region of WT CcO and PJL49
The water is rendered in red spheres. In the PJL49 figure the 2fo-fc density map shows the mutation did not affect the c-terminus H26-water-T550 interaction.

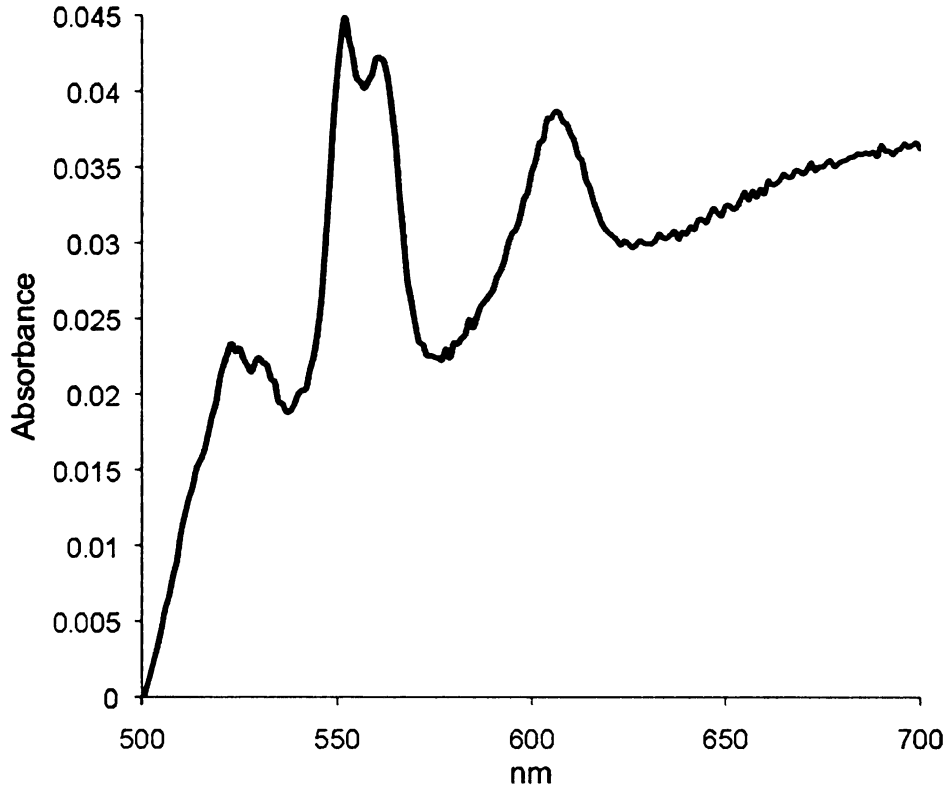

Figure 4. 19: Reduced-minus-oxidized spectra of PJL63 membrane fraction
The spectra show that the expression level of PJL63 is fairly good. And the enzyme showed a normal spectra (605 nm α peak) while inside the membrane.

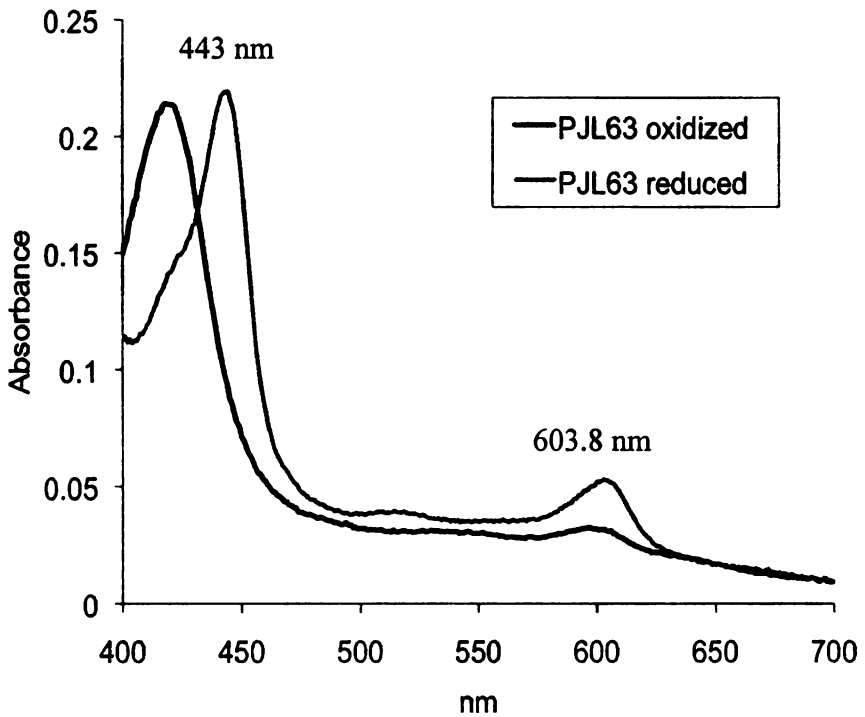

Figure 4. 20: Reduced and oxidized spectra of FPLC purified PJL63
Both soret peak and a peak are shifted in the purified PJL63 C*c*O, suggesting the redox center of this enzyme could be changed.

The plasmid was then conjugated into *R.sph* strain Δ123 as described in Chapter 2 for expression.

The PJL63 protein was expressed and purified as described in Chapter 2. Before the purification, the reduced-minus-oxidized spectrum of the membrane fraction of PJL63 was taken and it looked the same as wild type *Rs*C*c*O (Figure 4.20). However, the reduced spectrum of the Ni-NTA FPLC purified PJL63 protein (Figure 4.21) showed a lower and shifted Soret peak (443nm) and shifted peak (603.8 nm), suggesting a possible loss of heme a_3 and disruption in the heme *a* region.

The steady state activities of purified PJL63 were measured at pH7.4 as described in Chapter 3. Compared to the wild type *Rs*C*c*O, the mutant PJL63 had a lower activity (860 e^-/sec/aa_3 vs 1090 e^-/sec/aa_3) and a tendency toward suicide inactivation – inactivation during turnover. These results and the altered spectrum of PJL63 suggested that this fusion protein might not be stable in structure. The fusion could have caused a conformational change in subunit I and subunit III and thus affected the heme region environment and the enzyme activity.

3. Discussion

The aim of the studies described in this Chapter was to examine several possibilities of improving the quality of *Rs*C*c*O crystals by removing flexible ends and creating gene fusions so as to improve the stability and molecular homogeneity of the protein. Of particular interest was to facilitate production of four subunit crystals at higher resolution than previously achieved. The results were disappointing in this regard, but did reveal some interesting functional information about the C-terminal region of subunit I.

Although the C-terminus of subunit I is not highly conserved and shows evidence of flexibility, there are some residues in that region that appear to be important to the enzyme function. This region is near the D132 residue, at the entrance to the D-channel in C*c*O. A report on the bovine heart C*c*O structure showed that a histidine residue at the subunit I C-terminus may be involved in stabilizing the water network in this region and could serve an important role for proton uptake (Muramoto et al. 2007) . According to the sequence alignment, E552 in the deletion region is also a conserved residue that could play a role in proton uptake. However, steady state activity assay results show that the E552A RsCcO mutant has similar activity to wild type C*c*O, suggesting that the loss of E552 itself may not be the cause of this loss of activity in PJL33. Still, it does not exclude the possibility of other residues in the deletion region being very important to the enzyme function, or the activity loss being caused by multiple changes of several residues together.

The 4 subunit crystal structure of *Rs*C*c*O suggests that the N-terminus of subunit III interacts with subunit I C-terminus to stabilize subunit III on the whole enzyme. Studies on the subunit III deletion enzyme show that one role of subunit III is to stabilize and protect the enzyme from suicide inactivation during reaction (Bratton et al. 1999). The mechanism of suicide inactivation is apparently not due to the production of reactive oxygen species since adding catalase and superoxide dismutase had no effect on the rate of inactivation (Bratton et al. 1999).

SDS-PAGE of the PJL33 protein suggested that after Ni-NTA and DEAE-5pw FPLC columns, the amount of subunit III was reduced compared to the wild type enzyme. Without subunit III, although C*c*O can maintain a high reaction rate at the beginning, it undergoes suicide inhibition and loss of activity. Suicide inactivation in subunit III less

enzyme is ultimately associated with the loss of Cu_B at the heme a_3-Cu_B binuclear center as measured by EPR spectroscopy and metal analysis, possibly due to the dissociation of one or more of Cu_B's ligands (Hosler 2004). Judging from the crystal structure of PJL33, however, the redox center is not affected, suggesting that this loss of subunit III in PJL33 is not servere.

Research results also showed that the rate of proton uptake through the D pathway, as well as the proton exit/back flow pathway, was slowed down in the absence of subunit III (Gilderson et al. 2003; Mills et al. 2003). On the other hand, arachidonic acid, which enhances the D pathway proton uptake, slows down the rate of inactivation of subunit III-less C*c*O. The role of subunit III could be to maintain a conformation of C*c*O that facilitates proton flow to the active site through the D pathway and proton backflow through the exit path to the active site (Mills and Hosler 2005). Although we can get high resolution structure of *Rs*C*c*O from the two subunit crystal, this suicide inactivation effect caused by the loss of subunit III showed the importantce of keeping the subunit III in the whole enzyme. Our ultimate goal is still to get high resolution structures of the whole enzyme.

In an effort to stabilize the subunit III and subunit I together, the subunit I C-terminus-subunit III N-terminus fusion mutant (PJL63) was made. However, initial studies on the properties of this fusion protein showed that the activity of PJL63 is affected. The structure of this enzyme could be disrupted, shown from the reduced spectra. The choice of the fusion point could be very important. More works are still needed to make the subunit I-III fusion protein a better candidate for the crystallization.

4. Conclusion and Summary

(1) Two mutants of *Rs*C*c*O with shortened versions of subunit I (PJL33 with loss of 16 residues at C-terminus, and PJL49 with loss of 6 residues at C-terminus) were created, expressed to good levels and characterized. The results showed that PJL33 has possibly lost some amount of subunit III and has lower activity and proton pumping compared to wild type *Rs*C*c*O. Another version of *Rs*C*c*O with six residues removed from subunit I , PJ49, shows normal activity and spectra compared to wild type *Rs*C*c*O, indicating that the last 6 residues of subunit I do not affect the activity of *Rs*C*c*O. Thus, site 561 was used as a fusion point in future research.

(2) Crystal structures of PJL33 and PJL49 were obtained in the 2 subunit form, but no four subunit crystals were found. Both mutant crystals showed a similar overall structure as the crystal structure of wild type *Rs*C*c*O, suggesting the deletion did not change the overall conformation of *Rs*C*c*O. In PJL33 structure, the conformation of C-terminus was changed because of the deletion of the last 16 residues. T550 became the new C-terminus of PJL33 and 2 water molecules that were bonded to it were lost. These changes could be the reason for the loss of activity and proton pumping of PJL33.

(3) A subunit I-III fusion mutant PJL63 was created. In this mutant, the C-terminus of subunit I and N-terminus of subunit III were fused together by molecule engineering using the subunit III gene (with the deletion of first 6 amino acid at N-terminus) and the 6-amino-acid truncated subunit I. Although the enzyme was produced in good amounts and showed a normal spectrum in the membrane, the reduced spectrum of purified enzyme showed disruption in the heme *a* and heme a_3 regions. The activity of the purified enzyme

was only 80% of wild type *Rs*C*c*O. These results indicated that this fusion could disrupt the subunit I and subunit III interaction, thus causing the activity change.

CHAPTER 5. CRYSTAL STRUCTURES OF PROTON UPTAKE PATHWAY MUTANTS OF *RSCCO* (a paper based on the studies reported in this Chapter is in press, Proc.Natl.Acad.Sci. See Appendix)

1. Introduction

Two proton uptake pathways, the D-pathway and the K-pathway, were found in *Rs*C*c*O by structural studies and site-directed mutagenesis (Fetter et al. 1995; Hosler et al. 1996; Wikstrom et al. 2000; Pawate et al. 2002). Research also showed that these two pathways are highly conserved among mammalian and bacterial C*c*Os(Ferguson-Miller and Babcock 1996). However, in the bovine C*c*O structure an additional pathway, the H-path, has been identified (Tsukihara et al. 1996; Yoshikawa et al. 1998). which appears not to be conserved in the bacterial C*c*O (Lee et al. 2000). The findings in the bovine C*c*O have led to the proposal of an alternative mechanism of proton pumping and questions regarding whether the process of proton transfer and energy transduction is conserved. This critical issue emphasizes the importance of defining the detailed structure of proton pathways.

In *Rs*C*c*O, the D-pathway starts from a conserved aspartic acid D132 (D124 in *Pd* C*c*O and D91 in bovine C*c*O) in subunit I and ends near the glutamic acid E286, which is close to the binuclear heme a_3-Cu_B center (Figure 5.1). Removal of the carboxyl at position 132 strongly inhibits enzyme activity (2% of wildtype *Rs*C*c*O) and proton pumping (Fetter et al. 1995). Several hydrophilic residues in the D-pathway are crucial for the function of proton uptake as evidenced by the effects of their mutation on enzyme activity

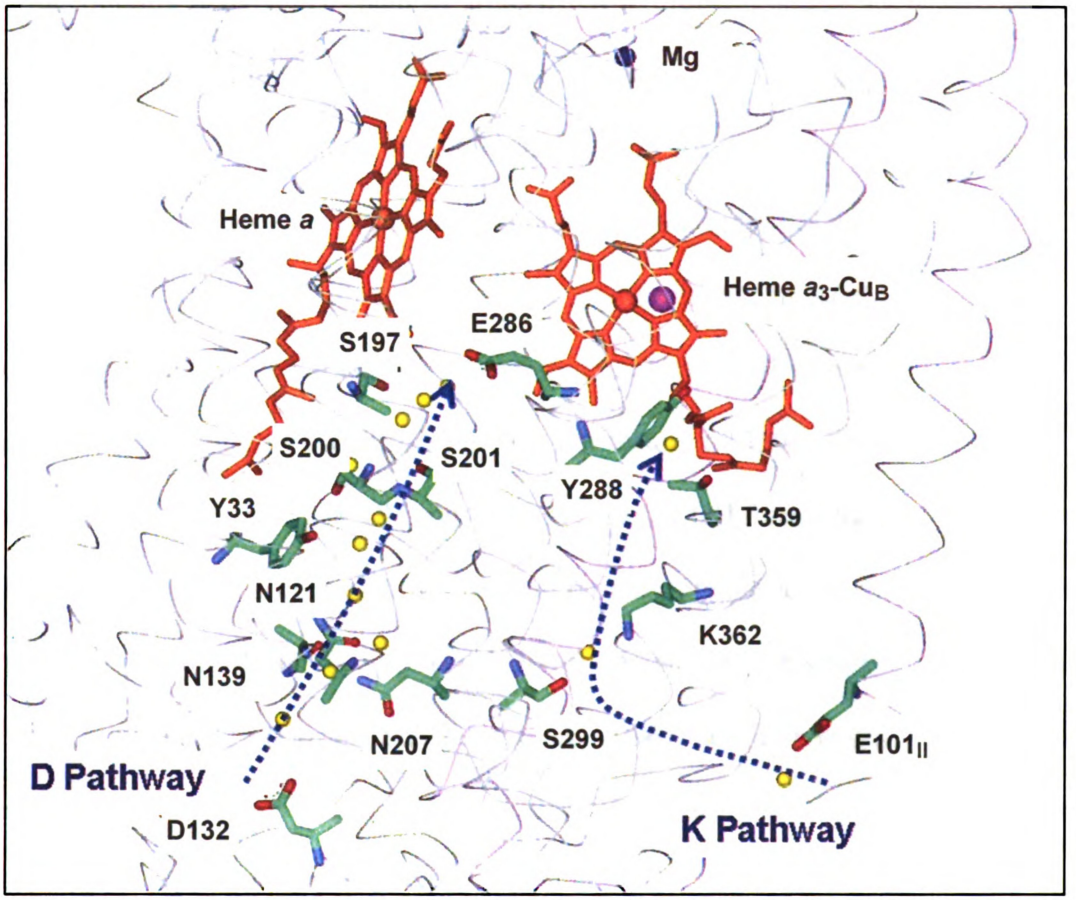

Figure 5. 1: Proton uptake pathways in *Rs*C*c*O
The D and K-pathway are shown in blue arrows. The key residues are rendered as stick model. The waters in the pathway are rendered as yellow spheres.

and proton pumping efficiency (Pfitzner et al. 2000; Pawate et al. 2002; Han et al. 2006; Zhu et al. 2010), in some cases inhibiting and in

others uncoupling activity. A chain of waters that hydrogen-bond to these hydrophilic residues was observed in high-resolution crystal structures of C*c*Os (Svensson-Ek et al. 2002; Qin et al. 2006; Koepke et al. 2009). The waters are in conserved positions in the crystal structures and serve an important function in proton uptake and proton pumping.

The K-pathway was named after a conserved lysine residue in subunit I. Mutational evidence indicates that the K-pathway starts from glutamate E101 in subunit II, involves a water bound between S299 and K362, and another water at T359. The K-pathway ends below heme a_3, where the Y288-OH and heme a_3 farnesyl-OH form a tight hydrogen bond that has been suggested to control the entrance of protons into the active site (Xu et al. 2007; Sharpe and Ferguson-Miller 2008; Qin et al. 2009). Mutations in this pathway cause major loss of enzyme activity (Hosler, Shapleigh et al. 1996), but the remaining activity still appears coupled to proton pumping (Hosler et al. 1996; Adelroth et al. 1998; Zaslavsky and Gennis 1998), implying that this pathway is exclusively involved in substrate proton uptake.

High-resolution crystal structures of two key mutants, D132A and K362M, would help us to further understand the function and mechanism of proton uptake pathways in *Rs*C*c*O. Thus these two mutant proteins were crystallized and are discussed in this Chapter. Both oxidized and reduced forms of crystals of D132A and K362M were analyzed and studied. On-line spectroscopy on the single crystals of D132A and K362M was also performed to study the effects of X-ray radiation on the crystals during data collection.

2. Methods and results

2.1 Plasmid construction

Two expression plasmids were constructed to express D132A and K362M proteins for crystallization. The pJL34 (for the expression of D132A) and pJL35 (for the expression of K362M) are derived from plasmids pCH61 and pCH62 (from Dr. Carrie Hiser in our lab) by inserting a fragment containing a short form of subunit IV gene (18 residues deleted from the C-terminus). The purpose of adding the short form of subunit IV was to improve the crystallization quality for the D132A and K362M, although later results showed that the addition did not have an effect on the crystallization of 4-subunit or 2-subunit crystals. After construction, the plasmids were then conjugated into *R.sph* strain Δ1Δ4 by using the method described in Chapter 2.

2.2 Protein expression and purification

After conjugation, the *R.sph* strains containing D132A or K362M were grown and harvested as described in Chapter 2. The spectra of membrane fractions of D132A and K362M are shown in Figure 5.2. D132A and K362M proteins were purified using the one-step Ni-NTA FPLC method described in Chapter 2. The membrane spectra showed that the constructs were successfully expressed. However, the expression levels of the C*c*Os from D132A and K362M are quite low compared with WT C*c*O and other mutants, making them difficult to purify and crystallize.

2.3 Crystallization of D132A and K362M

Both 4-subunit and 2-subunit crystallization conditions were tried on the purified D132A and K362M proteins. Both forms of crystals could be found under appropriate conditions (Table 5.1). The crystals were analyzed and diffracted at the ANL synchrotron. Datasets

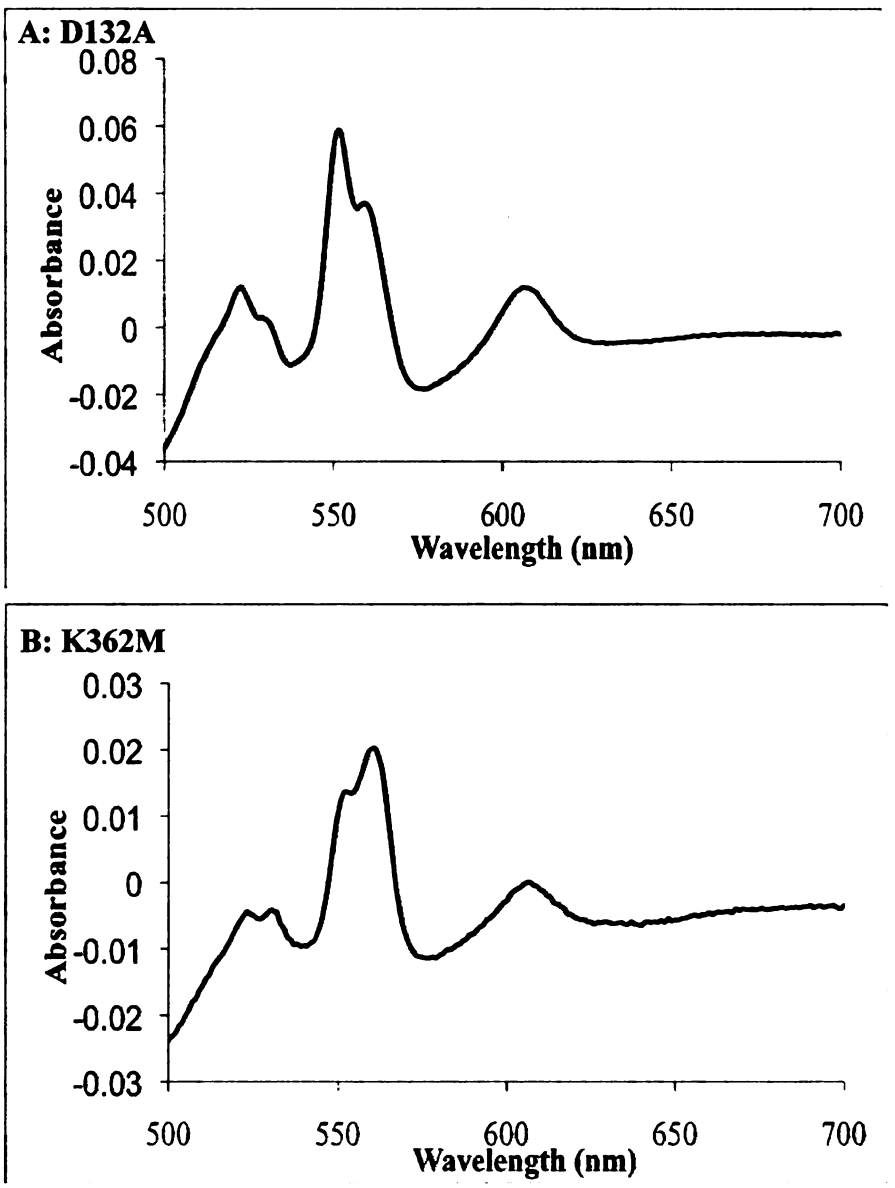

Figure 5. 2: Spectra of membrane fraction of D132A and K362M.
The 605 nm peak in both D132A and K362M reduced minus oxidized spectra is very low compared to 550 nm peak. This suggests that although D132A and K362M protein were expressed successfully, the expression level of them is very low.

	D132A	K362M
4-subunit Crystals	6 μL of enzyme solution containing 10 mM Tris, pH 8.0, 50 mM NaCl, 0.20% decyl maltoside and 120 μM C*c*O was mixed with 6 μL of reservoir solution containing 100 mM MES, pH 5.8, 23% PEG-400	6 μL of enzyme solution containing 10 mM Tris, pH 8.0, 50 mM NaCl, 0.20% decyl maltoside and 120 μM C*c*O was mixed with 6 μL of reservoir solution containing 100 mM MES, pH 5.8, 24.5% PEG-400
	Best Resolution: 3.5Å	Best resolution: 3.7Å
2-subunit Crystals	6 μl of enzyme solution containing 10 mM Tris, pH 8.0, 50 mM NaCl, 0.20% decyl maltoside and 120 μM C*c*O was mixed with 3 μL of reservoir solution containing 100 mM MES, pH 6.3, 29% PEG-400 and 3 μl of crystallization additive solution containing 5% heptanetriol, 32 mM $MgCl_2$, 1.3 mM $CdCl_2$ and 0.026% dodecyl maltoside.	6 μl of enzyme solution containing 10 mM Tris, pH 8.0, 50 mM NaCl, 0.20% decyl maltoside and 120 μM C*c*O was mixed with 3 μL of reservoir solution containing 100 mM MES, pH 6.3, 27.5% PEG-400 and 3 μl of crystallization additive solution containing 5% heptanetriol, 32 mM $MgCl_2$, 1.3 mM $CdCl_2$ and 0.026% dodecyl maltoside.
	Best resolution: 2.15-2.5Å	Best resolution: 2.30-2.6Å

Table 5. 1: Crystallization conditions of D132A and K362M

	D132A	K362M
4-subunit Crystals	6 μL of enzyme solution containing 10 mM Tris, pH 8.0, 50 mM NaCl, 0.20% decyl maltoside and 120 μM C*c*O was mixed with 6 μL of reservoir solution containing 100 mM MES, pH 5.8, 23% PEG-400	6 μL of enzyme solution containing 10 mM Tris, pH 8.0, 50 mM NaCl, 0.20% decyl maltoside and 120 μM C*c*O was mixed with 6 μL of reservoir solution containing 100 mM MES, pH 5.8, 24.5% PEG-400
	Best Resolution: 3.5Å	Best resolution: 3.7Å
2-subunit Crystals	6 μl of enzyme solution containing 10 mM Tris, pH 8.0, 50 mM NaCl, 0.20% decyl maltoside and 120 μM C*c*O was mixed with 3 μL of reservoir solution containing 100 mM MES, pH 6.3, 29% PEG-400 and 3 μl of crystallization additive solution containing 5% heptanetriol, 32 mM $MgCl_2$, 1.3 mM $CdCl_2$ and 0.026% dodecyl maltoside.	6 μl of enzyme solution containing 10 mM Tris, pH 8.0, 50 mM NaCl, 0.20% decyl maltoside and 120 μM C*c*O was mixed with 3 μL of reservoir solution containing 100 mM MES, pH 6.3, 27.5% PEG-400 and 3 μl of crystallization additive solution containing 5% heptanetriol, 32 mM $MgCl_2$, 1.3 mM $CdCl_2$ and 0.026% dodecyl maltoside.
	Best resolution: 2.15-2.5Å	Best resolution: 2.30-2.6Å

Table 5. 1: Crystallization conditions of D132A and K362M

	Protein and PDB number	**D132A** **3OMI**	**K362M** **3OMA**	**D132A reduced** **3OMN**	**K362M Reduced** **3OM3**
Unit Cell Parameters	Space group	$P2_12_12_1$	$P2_12_12_1$	$P2_12_12_1$	$P2_12_12_1$
	Cell dimensions (Å)	a=125.0 b=131.3 c=175.8	a=124.7 b=131.6 c=176.6	a=124.5 b=131.8 c=176.9	a=124.7 b=131.4 c=178.0
	Molecules per asym. unit	2	2	2	2
Data Collection	Resolution range (Å)	50-2.16 (2.23-2.15)*	50-2.30 (2.42-2.32)*	50-2.15 (2.23-2.15)*	50-2.60 (2.76-2.64)*
	Completeness (%)	96.5(81.6)*	97(90.6)*	97(84.0)*	91.8(86.4)*
	No of unique reflections	151,816 (12,579)*	145,094 (14,144)*	153,760 (13,130)*	96,671 (9,305)*
	Redundancy	6.9 (5.0)*	5.5(4.5)*	7.0(5.1)*	4.4 (3.9)*
	Rmerge (%)	9.2 (55.6)*	5.9(35.0)*	8.6(57.5)*	5.6(24.6)*
	I/s	16.3 (2.26)*	22.7(3.6)*	20.3(2.25)*	21.4(3.23)
Structural Refinement	No. of refined atoms	13399	13403	13759	13207
	R-factor/Rfree (%)	19.2/21.5	19/21.9	19.8/21.9	19.9/22.9
	Average B-factor	38.5	46.5	43.9	54.9
	Rmsd bond length (Å)	0.011	0.011	0.011	0.010
	Rmsd bond angle (deg)	1.164	1.185	1.164	1.174

Table 5. 2: Crystal parameters of D132A and K362M

were collected and refined as described in Chapter 2. However, the resolution of the 4-subunit crystals of D132A and K362M is very low (3.5 Å for D132A and 3.9Å for K362M) and the data quality is not good enough for further study. The 2-subunit crystals of D132A and K362M diffracted to high resolution (shown in Table 5.2). The PDB files of these mutants were deposited in RCSB protein data bank as shown in Table 5.2.

2.4 Crystal structure of oxidized D132A

2.4.1 Overall structure of oxidized D132A

The overall structure of oxidized D132A is very similar to the WT *Rs*C*c*O oxidized crystal structure. They are in the same space group ($P2_12_12_1$) and have similar unit cell dimensions (Table 5.2). The heme *a* and Cu_B-heme a_3 center of D132A and their ligating residues were in the same conformation as the WT *Rs*C*c*O (Figure 5.3), indicating that the mutation did not inhibit the activity of the protein by altering the character of the redox centers, as was concluded from previous spectroscopic results on the D132A mutant (Fetter et al. 1995; Mills and Hosler 2005). The D132A crystal structure contains all the lipids and detergent molecules that were resolved in the WT *Rs*C*c*O.

2.4.2 D-pathway waters in oxidized D132A

In the D132A crystal structure, the position of almost all the waters and key residues of the D-pathway are unchanged (Figure 5.4A). The waters between N139 and E286 are all in the same locations as WT *Rs*C*c*O as are key residues including E286, N121 and N139. However, one structural difference was immediately evident: a strong Fo-Fc difference electron density peak appears at the original position of the D132 carboxyl group (Figure 5.4A & 5.5A).

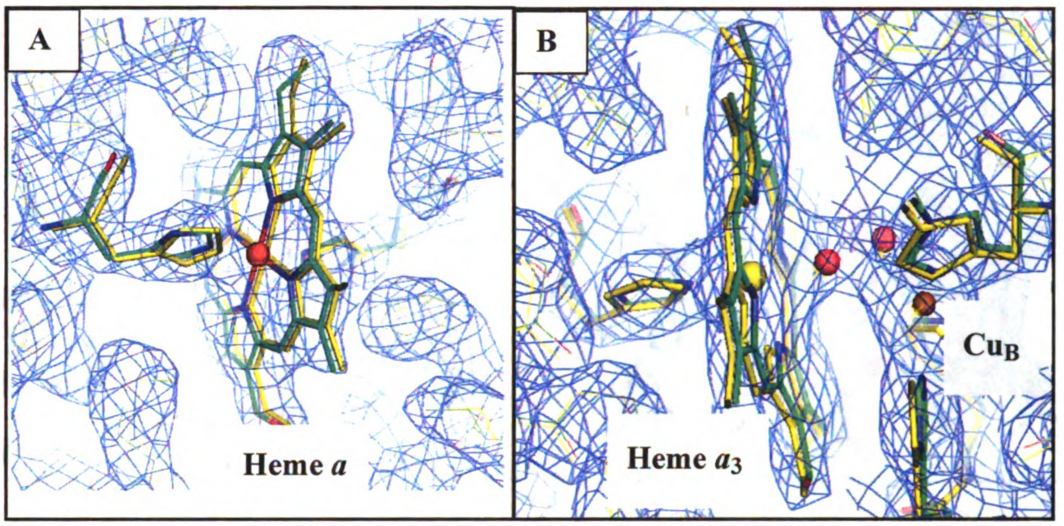

Figure 5. 3: Redox centers in oxidized D132A crystals.
The structure of oxidized D132A crystals were aligned with the WT C*c*O oxidized structure 2GSM. The green structure is the D132A and the yellow structure is the 2GSM. The 2Fo-Fc map at 1σ was shown in blue mesh. The alignment showed that the postitions of the importants ligands and waters at the redox centers of D132A are in the same conformation as WT C*c*O.

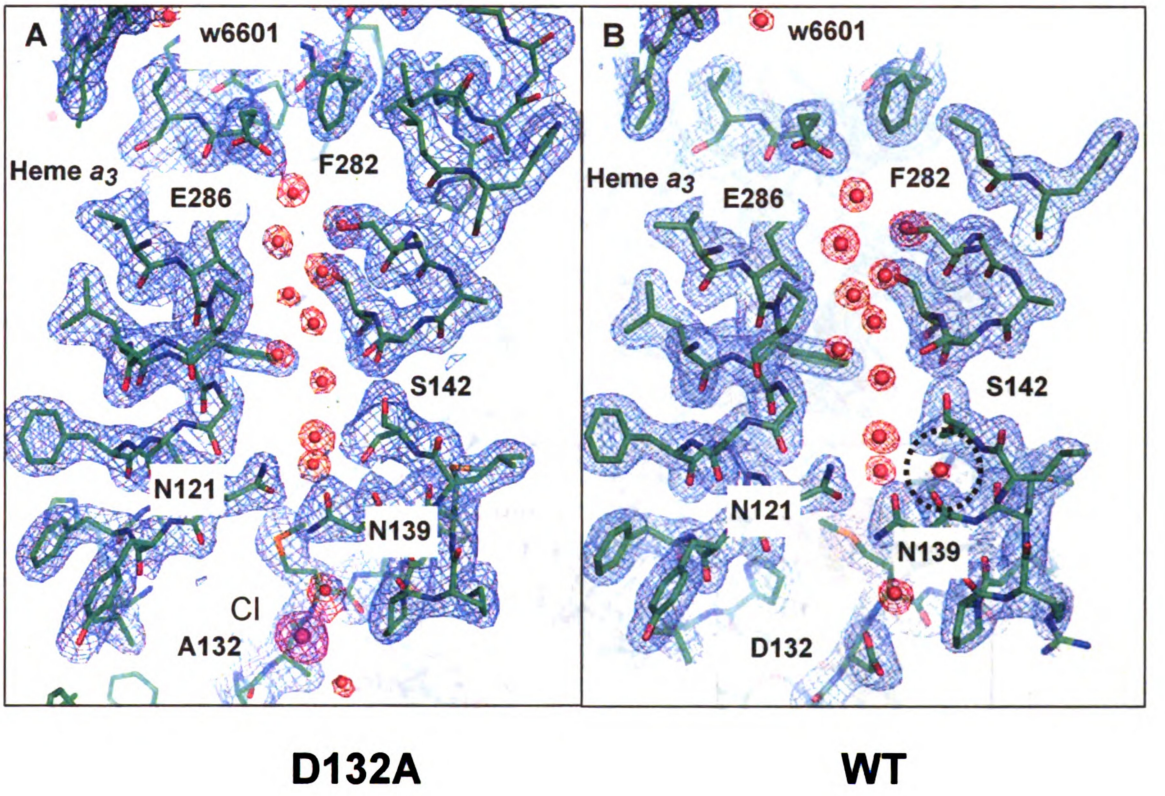

Figure 5. 4: Comparison of D-pathway water arrangement in D132A and WT C*c*O
A: Residues and waters of D132A D-pathway. **B:** Rsidues and waters of WT C*c*O D-pathway. 2Fo-Fc difference Fourier electron density map, contour at 1σ, is shown in blue for protein, and in red for water molecules. The pattern of waters in D132A (left) is almost identical to WTC*c*O (right). There are 12 waters in WTCcO D-pathway, 11 in the D132A D-pathway. The missing water in D132A is the N207 water (black dotted circle). A chloride ion (purple).replacesthe carboxyl group of D132. Except N207 (shown in figure 5.5), the conformations of other key residues in D-pathway remain unchanged

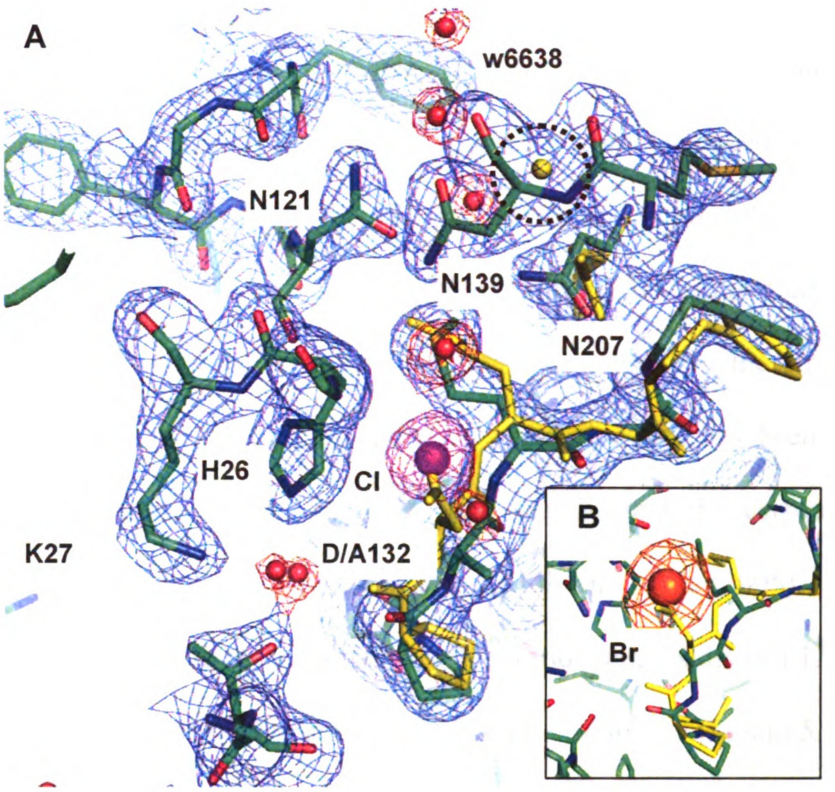

Figure 5. 5: The mutation region in D132A oxidized crystals
A: The Entry of the D-Pathway The chloride ion (magenta sphere) is shown replacing the carboxyl group of D132. The D132A C*c*O mutant structure is in green sticks; WTC*c*O (2GSM) is shown in yellow sticks. Superposition of these 2 structures shows the 1 Å backbone shift of residues 130-135, and the conformational change of N207. Water 6638 that was hydrogen bonded to N207 is gone in D132A structure (black dotted circle). N207 is bonded to water 6574, which is also bonded to N139. **B (inset): The position of bromide in the entry region** The Fo-Fc Difference Fourier electron density map at 3σ level (orange mesh) in a bromide soaked D132A crystal. The resolution of the soaked crystal is lower (3.5 Å) thanthe non-treated crystal, but the bromide density is still very clear in the structure. The size of this density indicates bromide replacement of the chloride (orange sphere).

This density was first modeled as an oxygen atom of water, but strong residual Fo-Fc densities were still observed along with a very low B-factor compared with its neighboring atoms, suggesting an ion larger than oxygen. Further experiments indicated that this position is most likely occupied by a chloride ion, since a bromide-soaked D132A crystal showed an even stronger electron density peak exclusively at this position (Figure 5.5B). Considering the abundance of chloride ion in the protein purification and crystallization buffer systems, it is reasonable for a chloride ion to be present in the structure. The replacement with chloride of an aspartic acid at a mutation site has been previously reported in other proteins (Yao et al. 1996) and implies that the carboxyl is in a deprotonated state, as predicted from pKa estimates (Mills and Hosler 2005). The loss of the carboxyl at 132, along with the substitution of a chloride ion, results in a 1Å backbone shift away from the mouth of the D-pathway in residues 130 to 135 (Figure 5.5A). These local changes significantly alter the entrance of the D-pathway, presumably playing a role in the inhibition of proton uptake.

2.4.3 N207 conformation change and loss of water in D132A

An additional change in conformation is observed in N207 and its associated water 6638 (Figure 5.5A). Water 6638 is lost and the side chain of N207 is now hydrogen-bonded to water 6574. This change could result from the shift of the 130-135 backbone including M133, which impacts N207. The new conformation of N207 may tighten the gate since water 6574 maintains its bond to N139, possibly contributing to the slowed proton transfer in the D-pathway. Previous mutational analysis of N121, N139 and N207 showed that they are all involved in controlling proton movement in the D-pathway (Pawate et al. 2002; Han

et al. 2006; Zhu et al. 2010) as major players in a gating mechanism that regulates proton uptake and backflow in the D pathway of *Rs*C*c*O.

2.5 Structure of oxidized K362M

2.5.1 Overall structure of oxidized K362M

The overall structure of oxidized K362M crystals is similar to WT *Rs*C*c*O. They have the same space group and similar unit cell dimension (Table 5.2). The heme *a* and heme a_3 region of K362M remains unchanged compared to the WT C*c*O. The crystal structure also showed that the mutation did not change the arrangement of D-pathway waters.

2.5.2 Changes in K-pathway in K362M oxidized crystal

Mutation of K362 to methionine results in an enzyme with less than 0.02% of the activity of WT C*c*O (Hosler et al. 1996), with very slow reduction of heme a_3. The possibility has been considered that Lys 362 undergoes a conformational change during enzyme turnover, moving from a "down" to an "up" position to bring the positive charge of the lysine closer to heme a_3 (Lepp et al. 2008). Inability to make such a movement and/or to supply the charge could account for the inhibition of the methionine mutant. However, no such change was observed in either K362M oxidized crystals or reduced crystals. Figure 5.6 shows that in K362M the methionine adopted a similar conformation as the lysine in WT *Rs*C*c*O but water 6633 normally bonded between K362 and S299, and

water 6516 close to T359, are eliminated. This loss of water appears to be the major structural change in this mutant, thus likely accounting for inhibition of K362M activity, possibly due to a role for these pinned waters in organizing a hydrogen-bonded water chain required for proton transfer.

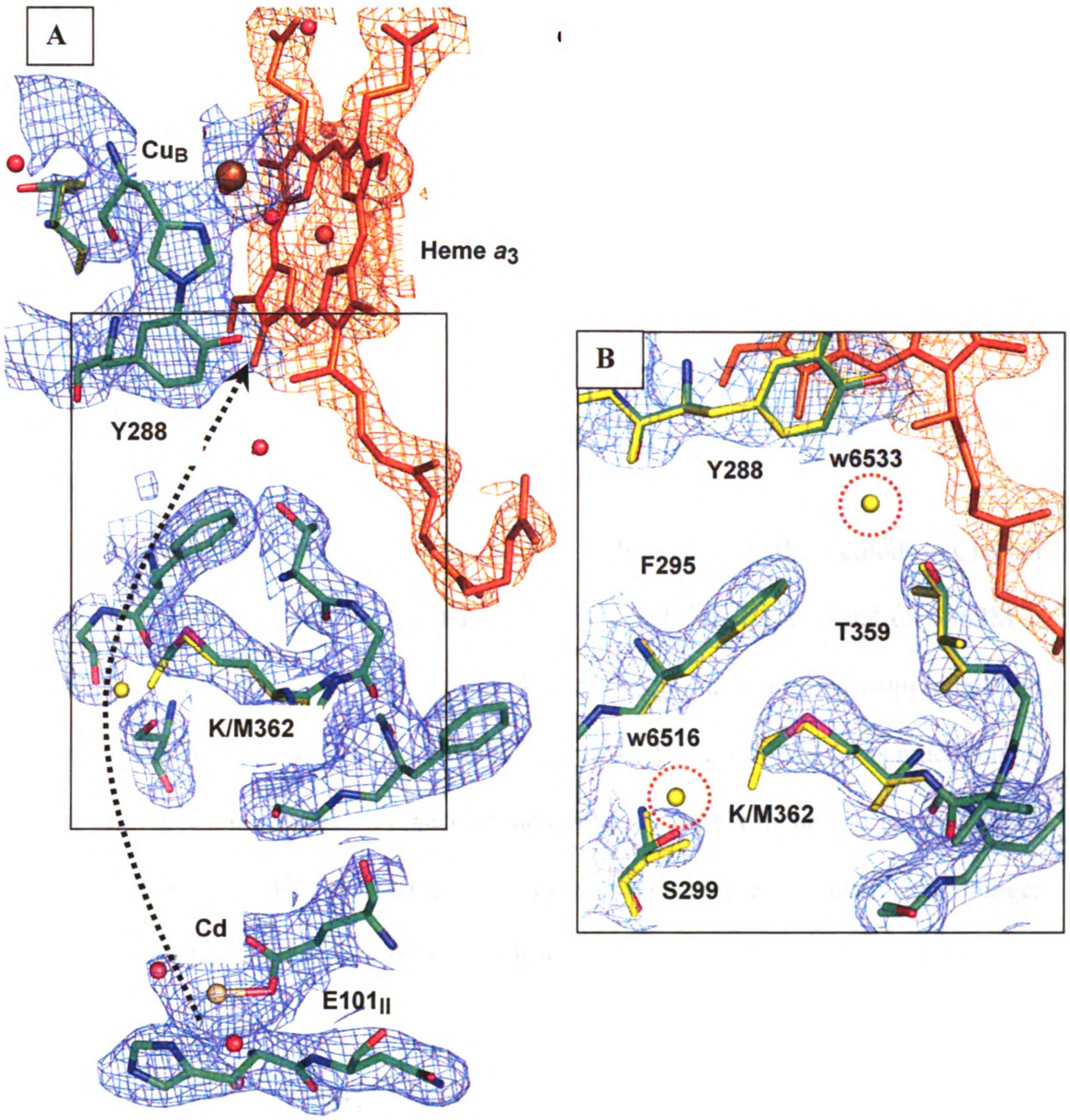

Figure 5. 6: Structural changes in K362M.
A: overall structure of K-pathway in K362M. 2Fo-Fc difference Fourier electron density map contoured at 1σ are shown in blue for the mutant. Cu_B atom is shown in brown sphere. Heme a_3 is shown in organ color. The dotted black arrow is the purposed the proton uptake path in the K pathway. In the K362M oxidized crystal structure, almost all the residues are in the same position as wildtype C*c*O. **B. Structure alignment at M362 region in K362M**. Methionine 362 (green/magenta) overlays lysine 362 (yellow) in WT C*c*O, but the water (w6533) that was bonded to T359 and between K362 and S299 (w6516) are lost (yellow spheres with red dotted circle).

There is a possibility that the loss of waters 6516 and 6633 could be attributed to the lower resolution of the crystal structure (2.3Å). However, in this structure all the D-pathway waters are very clearly observed. Further, other structures of the D132A mutant at 2.4Å showed these two K-pathway waters with similarly strong densities as WT, indicating that the effects of resolution of the crystal do not account for the disappearance of these K path waters.

2.6 Reduction of D132A and K362M crystals

The reduction of D132A and K362M crystals was performed using the methods in Chapter 2. The reductions were performed under 4°C. The usual time for a crystal of K362M at size of 0.3mm X 0.3mm to be fully reduced is about 10 minutes, turning from a dark red color into a green color. However, the time required for D132A crystals was much longer (15 minutes) and the conversion appeared incomplete. Crystals incubated longer than15 minutes deteriorated and did not diffract well. Later results showed that even at this longer incubation time, the D132A crystals were still partially reduced.

2.7 Structure of reduced crystals of D132A and K362M

Our previous results showed that dithionite reduction of oxidized crystals of wildtype *Rs*C*c*O at 4 °C, followed by fast freezing in liquid nitrogen, reveals a significantly altered conformation observable in frozen crystals analyzed by x-ray diffraction (Qin et al. 2009). The alterations include movement of the heme a_3 porphyrin ring, its farnesyl tail, and helix VIII, as well as loss of a key water linking the D path to the active site and

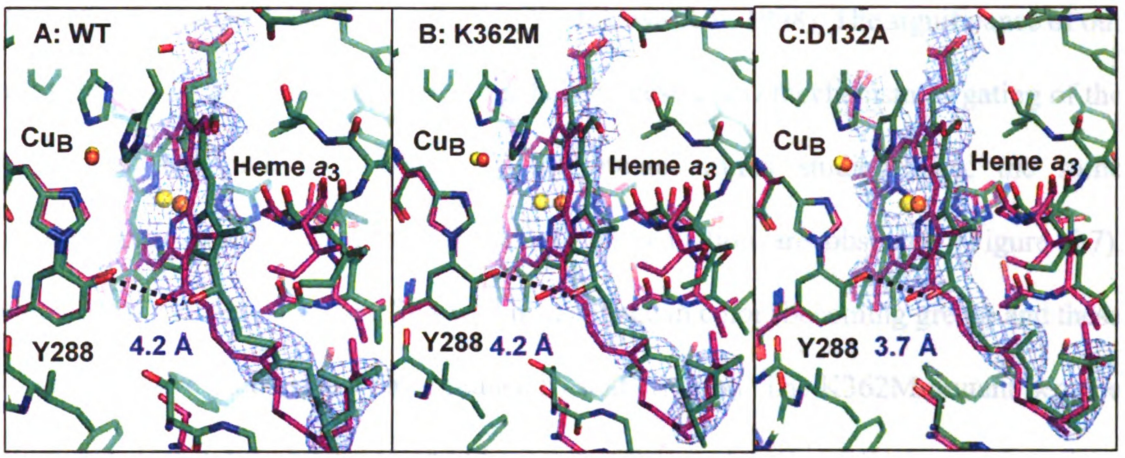

Figure 5. 7: Heme *a*3 region of the reduced crystals of *Rs*C*c*O
Reduced D132A and K362M have similar conformational changes at the heme a_3 and helix VIII region to those in the reduced wildtype CcO. The distance between the hydroxyl group of Y288 and heme a_3-farnesyl-OH is increased from 2.6 to 4.2 Å in wildtype and K362M, suggesting a gate opening mechanism. The reduced D132A crystal is only partially reduced as evidenced by a smaller shift to 3.7 Å. When reduced (60%) and oxidized (40%) forms are refinement separately, a better fit is obtained.

formation of a new water chain into the active site. These changes upon reduction were an unexpected finding since other structural studies of bacterial oxidases (Durr et al. 2008; Koepke et al. 2009) have reported no changes (Only ref 32of PNAS paper applies to no change in reduced state), and in the bovine C*c*O the changes are fewer and mainly involve different regions than those seen in *Rs*C*c*O(Yoshikawa et al. 1998). The significance of our recent findings is potentially profound, as they suggest a new mechanism of gating of the two proton pathways (Qin 2009). In the mutant forms studied here, the same conformational changes seen in WT *Rs*C*c*O on reduction are observed (Figure 5.7). Reduction of the crystals can be followed by a change in color (becoming green) and these two very inactive mutants appear to reduce by that criterion. The K362M mutant became fully reduced, as judged by the color and spectra of the crystals (Fig 5.9 E), even though its reduction in solution is very slow. Along with all the same changes observed in WT, the reduced K362M mutant still showed the loss of the two waters in the K channel as seen in its oxidized form.

Figure 5.7 also shows that a smaller change in distance between Tyr288-OH and the farnesyl-OH is evident in the D132A reduced crystals. The spectra of the single crystal (Figure 5.9F) confirmed that reduction of the crystal was incomplete and the structure was best fitted by the assumption of 40% oxidized / 60% reduced (Figure 5.8, Figure 5.9). Incomplete reduction of D132A resulting in a mixed structure is most clearly seen in the region of serine 425 where a large conformational change occurs (Figure 5.8). Fitting with a fully reduced or fully oxidized structure results in a Fo – Fc map with significant unaccounted-for density. After a number of trials, a good fit was obtained when the regions of greatest conformational change (heme a_3 and residues 424/425/426) were assumed to be

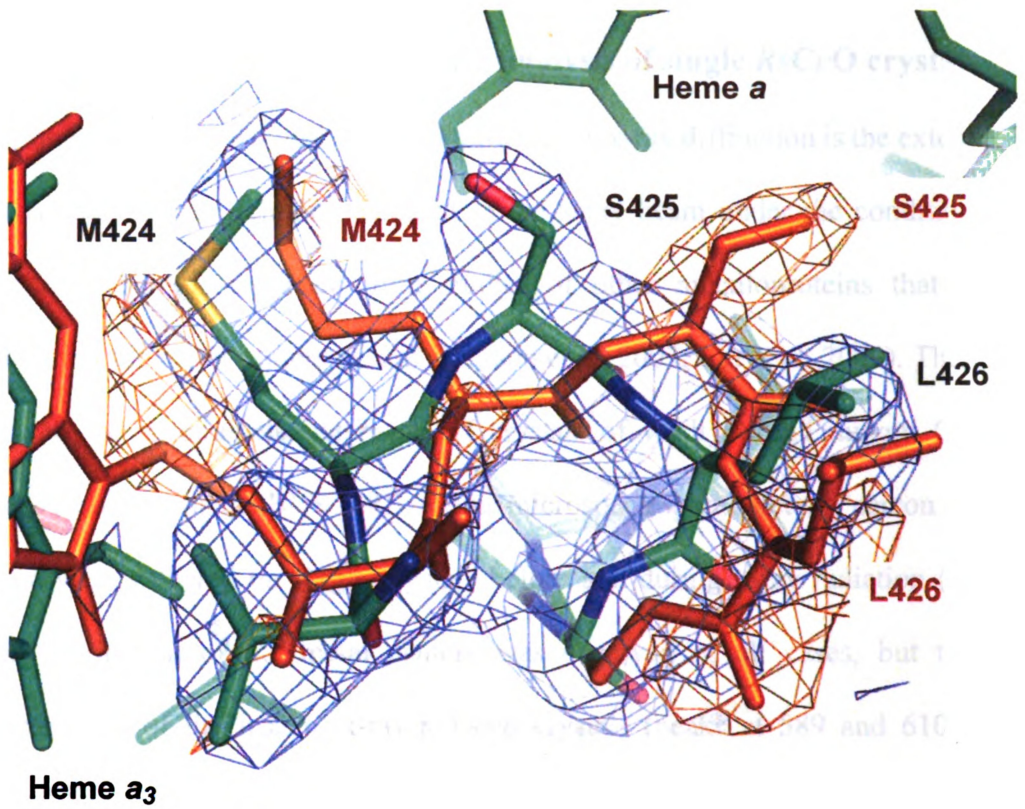

Figure 5. 8: Alternative conformations in D132A
The electron density around S425 suggests that both reduced (60%,blue density) and oxidized (40%, orange density) forms are present in one crystal, which is consistent with the slow reduction of D132A.

made up of two structures, a 40/60 ratio of oxidized/reduced. A single intermediate form did not fit the data well.

2.8 On-line microspectrophotometric analysis of single *Rs*C*c*O crystals

A key question in the analysis of metalloproteins by x-ray diffraction is the extent to which an "oxidized" crystal remains oxidized in the x-ray beam under the conditions of data collection. There is evidence from studies of other metalloproteins that significant reduction of the metal centers occurs (Pearson et al. 2007; Liu et al. 2009). Therefore, we measured the spectral characteristics of crystals of wildtype and mutant C*c*O at 100 degrees Kelvin using the BIOCARS on-line microspectrophotometer (Pearson et al. 2007). Spectra were gathered on single crystals before and during x-ray radiation (Figure 5.9, A-F). Reduction of the metal centers was observed in all cases, but the spectral characteristics of the frozen, x-ray-reduced crystals (peaks at 589 and 610 nm) were different from those of crystals that were dithionite-reduced prior to freezing and x-ray irradiation (a single peak at 606 nm), indicating a strained configuration in the former case. This was confirmed by briefly annealing the crystals (interrupting the flow of 100°K nitrogen gas for 2 -3 seconds) which resulted in the spectral characteristics changing to those of the normal, reduced state. The results are consistent with the maintenance of the oxidized protein conformation (Aoyama et al. 2009) even though the metal centers are reduced, before annealing at warmer temperature allows the protein conformational change to occur. The strained configuration offers interesting spectral features that may reveal an oxygen intermediate captured at the active site during irradiation, absorbing at 589 nm. Other spectral methods such as single crystal low

Figure 5. 9: Online spectra of single crystal of *Rs*C*c*O

Blue curve: spectra collected before X-ray radiation. **Green curve:** spectra taken after X-ray radiation for 2 minutes. **Red curve:** spectra taken after X-ray radiation for 10 minutes. Black dotted curve: annealed spectra, taken after the cooling nitrogen was blocked for 3-4 seconds to briefly warm the crystals. **Figure 5.9A**: oxidized wildtype C*c*O crystal is reduced after X-ray radiation for 10 minutes, producing a strained configuration (peaks at 589nm and 610nm) not equivalent to the native reduced form until annealed (606 nm). **Figure 5.9 B**: D132A spectra. **Figure 5.9 C**: K362M spectra. Note that the D132A oxidized crystal spectrum is different from both wildtype C*c*O and K362M, suggesting that the frozen D132A crystal might be in a different initial oxidized conformation (at room temperature the crystal shows a normal oxidized spectrum. **Figure 5.9D, 5.9E, 5.9 F**: the on-line spectra of C*c*O crystals previously reduced by dithionite and frozen. Spectra show that the crystals are well reduced before the X-ray radiation, except D132A. A similar 589 nm species is produced by irradiating the reduced crystals as is seen in the radiated oxidized crystals, but to a lesser extent.

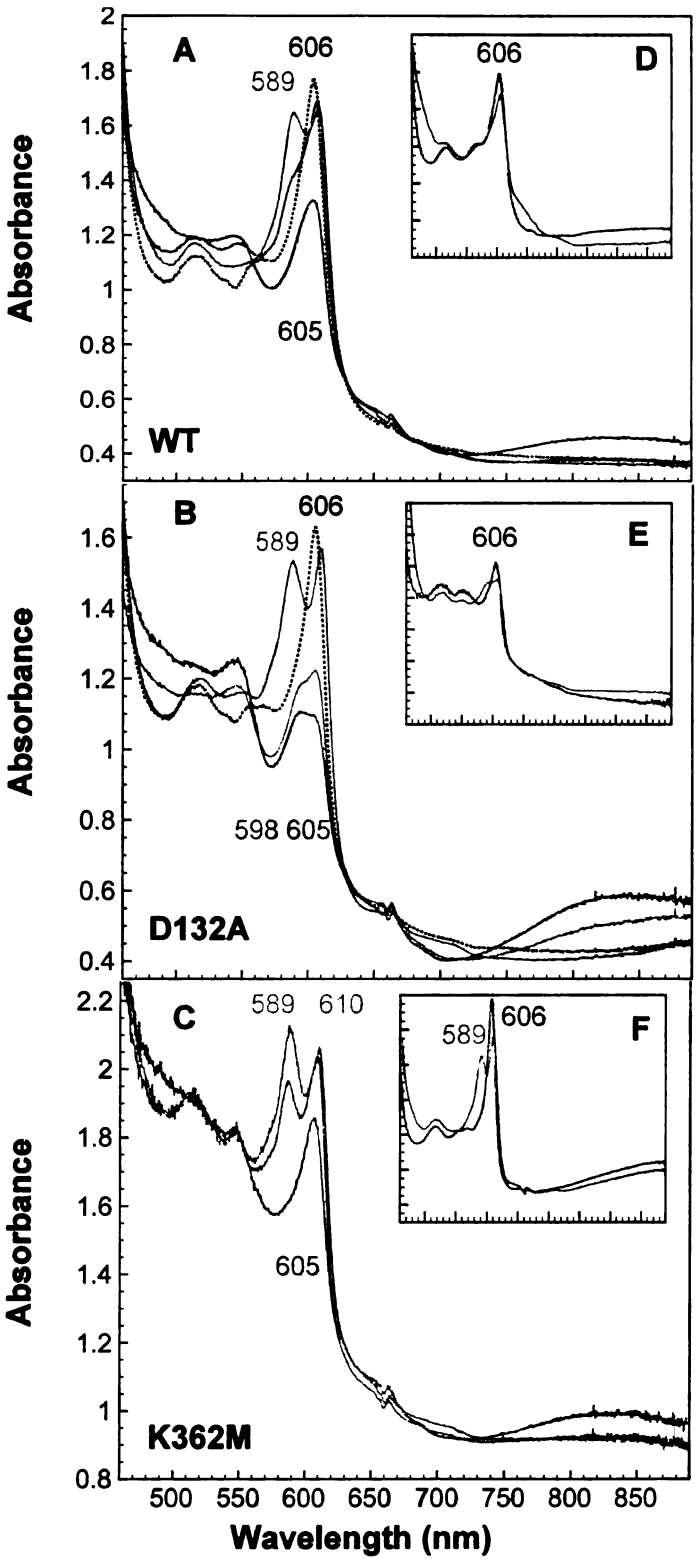

Figure 5. 9 : Online spectra of single crystal of *Rs*C*c*O

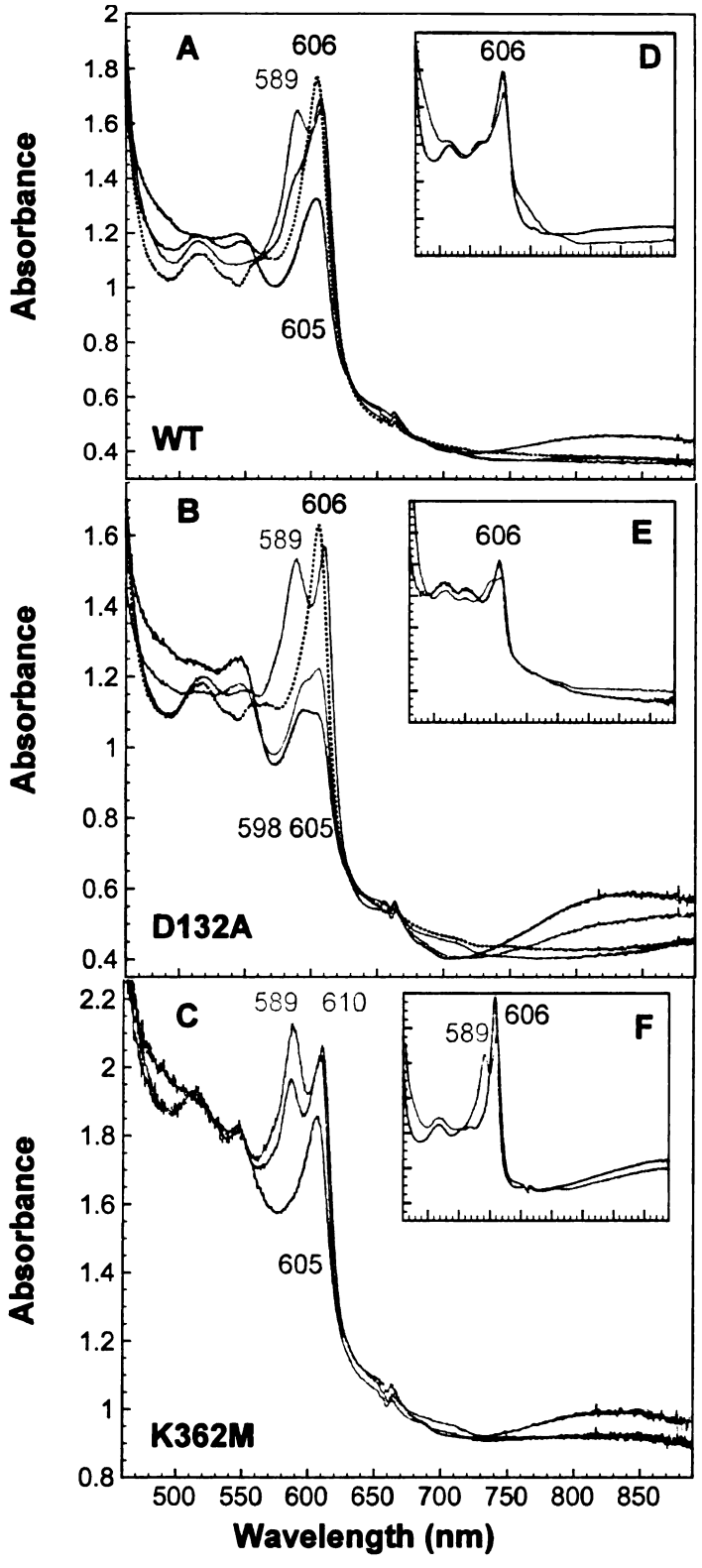

Figure 5. 9 : Online spectra of single crystal of *Rs*C*c*O

temperature EPR or resonance raman will be needed to determine the nature of this form; the Soret region of the spectrum, which could provide some clues, absorbs too strongly to be measured (Figure 5.9).

3. Discussion

A model has been proposed (Sharpe and Ferguson-Miller 2008) that offers a rationale for the sequence of events that could produce the conformational changes seen in the crystallized reduced state, and also provides an explanation for the delayed changes in the D132A mutant. The model proposes that an initial step in reduction of oxidized C*c*O is electron transfer (through Cu_A and heme *a*) to Cu_B^{2+}-OH, followed by rapid protonation of its ligand, His334, with a D-path-supplied proton to maintain charge neutrality. The protonation of one Cu_B ligand results in weakening of the bond to another ligand, the His284-Tyr288 covalently bonded pair, accompanied by hydrogen bond rearrangement within it and breaking of the tight hydrogen bond between Tyr288-OH and farnesyl-OH. The resulting release of the heme a_3-farnesyl-OH leads to the observed shift of heme a_3 away from the Cu_B ligand and the opening of the top of the K path, allowing a water chain to form and proton entry. In this model, if the D-path is inhibited, the sequence of events and conformational changes would proceed very slowly, as observed in the D132A mutant. In solution, the D132A mutant has a very slow turnover limited by proton uptake; in the crystal, proton movement appears to be further compromised, implying that some conformational rearrangements may be necessary to allow proton transfer in the D-path (as suggest for the asparagine bridge (Pawate et al. 2002; Cukier 2004; Henry et al. 2009). A further corollary of this analysis is that the state that has been trapped in the dithionite reduced frozen crystal is the equivalent of the 2- or 4-electron reduced form, before oxygen

binds. Presumably, oxygen would not be available in the presence of high dithionite during reduction and freezing. It is interesting to note that H/D exchange experiments in *Rs*C*c*O (Busenlehner et al. 2006; Busenlehner et al. 2008) show a change in conformation upon reduction in one of the same regions that is altered in the crystallographically-observed reduced state (residues 354-360 of helix VIII), supporting the involvement of protein dynamics in the mechanism of cytochrome *c* oxidase.

4. Summary and Conclusions

The first high resolution crystal structures were obtained of two mutants that define the key proton uptake pathways in bacterial oxidases, D132A and K362M, in both oxidized forms and reduced forms. Minimal changes in their overall structures were found as compared to WT, indicating no long range effects of the mutations.

In D132A, the loss of the carboxyl group at position 132 and its replacement by a chloride ion caused a local backbone shift in residues 131-135 and a conformational change of N207.

Although no conformational change was observed for the mutated lysine 362 in the K362M crystal structure, two K-pathway waters are lost. These results suggest that loss of water itself accounts for the drastic changes of activity in this mutant, emphasizing the important role of waters in proton uptake and proton pumping.

On-line spectral analysis of wildtype and mutant crystals during x-ray exposure provides definitive evidence that low temperature restricts conformational change when the metal centers are reduced by x-rays, suggesting the maintenance of a strained configuration. This

clarifies why conformational differences between reduced and oxidized forms can be observed.

APPENDIX

An article based on the research in Chapter 5:

Crystallographic and Online Spectral Evidence for Functional Role of Conformational Change and Conserved Water in Cytochrome Oxidase

Jian Liu, Ling Qin, Shelagh Ferguson-Miller

has been accepted by the PNAS, Nov. 2010.

PNAS, BIOLOGICAL SCIENCES: Biochemistry

Crystallographic and Online Spectral Evidence for Functional Role of Conformational Change and Conserved Water in Cytochrome Oxidase

Jian Liu[1], Ling Qin[2], Shelagh Ferguson-Miller[1*]

[1]Department of Biochemistry and Molecular Biology

Michigan State University, East Lansing, MI 48824. E-mail: fergus20@msu.edu

Telephone: 517-355-0199, Fax: 517-353-9334

[2] Department of Biomass Science and Conversion Technology

Sandia National Laboratories

Livermore, CA 94551

Abstract

Crystal structures in both oxidized and reduced forms are reported for two bacterial cytochrome c oxidase mutants that define the D and K proton paths, showing the loss of strategic waters as key to inhibited proton transfer and conformational change in response to reduction. In the oxidized state both mutants of the *Rhodobacter sphaeroides* enzyme, D132A and K362M, show overall structures similar to wildtype, indicating no long-range effects of mutation. In the reduced state, the mutants show an altered conformation similar to that seen in reduced wildtype (Qin et al. Biochemistry 48: 5121, 2009), confirming this reproducible, reversible response to reduction. In the strongly inhibited D132A mutant, positions of residues and waters in the D-pathway are unaffected except in the entry region close to the mutation, where a chloride ion replaces the missing carboxyl and a 2 Å shift in N207 results in loss of its associated water. In K362M the methionine occupies the same position as the original lysine, but K362- and T359-associated waters in the wildtype structure are missing, likely accounting for the severe inhibition. Spectra of oxidized frozen crystals taken during X-ray radiation show metal center reduction, but indicate development of a strained configuration that only relaxes to a native form upon annealing. Resistance of the frozen crystal to structural change explains why the oxidized conformation is observable and supports the conclusion that the reduced conformation has functional significance. A mechanism is described that explains the conformational change and the inhibited conversion of the D-path mutant.

BIBLIOGRAPHY

Aagaard, A., A. Namslauer and P. Brzezinski (2002). "Inhibition of proton transfer in cytochrome c oxidase by zinc ions: delayed proton uptake during oxygen reduction." *Biochim Biophys Acta* **1555**(1-3): 133-9.

Adelroth, P., R. B. Gennis and P. Brzezinski (1998). "Role of the pathway through K(I-362) in proton transfer in cytochrome c oxidase from R. sphaeroides." *Biochemistry* **37**(8): 2470-6.

Albracht, S. P. and R. Hedderich (2000). "Learning from hydrogenases: location of a proton pump and of a second FMN in bovine NADH--ubiquinone oxidoreductase (Complex I)." *FEBS Lett* **485**(1): 1-6.

Antunes, F., A. Boveris and E. Cadenas (2004). "On the mechanism and biology of cytochrome oxidase inhibition by nitric oxide." *Proc Natl Acad Sci U S A* **101**(48): 16774-16779.

Aoyama, H., K. Muramoto, K. Shinzawa-Itoh, K. Hirata, E. Yamashita, T. Tsukihara, T. Ogura and S. Yoshikawa (2009). "A peroxide bridge between Fe and Cu ions in the O2 reduction site of fully oxidized cytochrome c oxidase could suppress the proton pump." *Proc Natl Acad Sci U S A* **106**(7): 2165-9.

Bailey, S. (1994). "The CCP4 suite: programs for protein crystallography." *Acta Crystallogr D Biol Crystallogr* **D50**(5): 760-763.

Beauvoit, B. and M. Rigoulet (2001). "Regulation of cytochrome c oxidase by adenylic nucleotides. Is oxidative phosphorylation feedback regulated by its end-products?" *IUBMB Life* **52**(3,4,5): 143-152.

Berry, E. A., M. Guergova-Kuras, L. S. Huang and A. R. Crofts (2000). "Structure and function of cytochrome bc complexes." *Annu Rev Biochem* **69**: 1005-75.

Branden, M., F. Tomson, R. B. Gennis and P. Brzezinski (2002). "The entry point of the K-proton-transfer pathway in cytochrome c oxidase." *Biochemistry* **41**(35): 10794-8.

Bratton, M., M. Pressler and J. Hosler (1999). "Suicide inactivation of cytochrome c oxidase: Catalytic turnover in the absence of subunit III alters the active site." *Biochemistry* **38**: 16236-16245.

Brunger, A. T., P. D. Adams, G. M. Clore, W. L. DeLano, P. Gros, R. W. Grosse-Kunstleve, J.-S. Jiang, J. Kuszewski, M. Nilges, N. S. Pannu, R. J. Read, L. M. Rice, T. Simonson and G. L. Warren (1998). "Crystallography & NMR System: a new software suite for macromolecular structure determination." *Acta Crystallogr D Biol Crystallogr* **D54**(5): 905-921.

Buse, G., T. Soulimane, M. Dewor, H. E. Meyer and M. Bluggel (1999). "Evidence for a copper-coordinated histidine-tyrosine crosslink in the active site of cytochrome oxidase." *Protein Science* **8**(5): 985-990.

Busenlehner, L. S., G. Branden, I. Namslauer, P. Brzezinski and R. N. Armstrong (2008). "Structural elements involved in proton translocation by cytochrome c oxidase as revealed by backbone amide hydrogen-deuterium exchange of the E286H mutant." *Biochemistry* **47**(1): 73-83.

Busenlehner, L. S., L. Salomonsson, P. Brzezinski and R. N. Armstrong (2006). "Mapping protein dynamics in catalytic intermediates of the redox-driven proton pump cytochrome c oxidase." *Proc Natl Acad Sci U S A* **103**(42): 15398-403.

Byrne, B., J. Abramson, M. Jansson, E. Holmgren and S. Iwata (2000). "Fusion protein approach to improve the crystal quality of cytochrome bo3 ubiquinol oxidase from Escherichia coli." *Biochim Biophys Acta* **1459**(2-3): 449-455.

Cannon, M. B. and S. J. Remington (2006). "Re-engineering redox-sensitive green fluorescent protein for improved response rate." *Protein Sci* **15**(1): 45-57.

Chan, S. I. and P. M. Li (1990). "Cytochrome c oxidase: understanding nature's design of a proton pump." *Biochemistry* **29**(1): 1-12.

Chang, H. Y., J. Hemp, Y. Chen, J. A. Fee and R. B. Gennis (2009). "The cytochrome ba3 oxygen reductase from Thermus thermophilus uses a single input channel for proton delivery to the active site and for proton pumping." *Proc Natl Acad Sci U S A* **106**(38): 16169-73.

Cherezov, V., D. M. Rosenbaum, M. A. Hanson, S. G. Rasmussen, F. S. Thian, T. S. Kobilka, H. J. Choi, P. Kuhn, W. I. Weis, B. K. Kobilka and R. C. Stevens (2007).

"High-resolution crystal structure of an engineered human beta2-adrenergic G protein-coupled receptor." *Science* **318**(5854): 1258-65.

Cherny, V. and T. DeCoursey (1999). "pH-dependent inhibition of voltage-gated H+ currents in rat alveolar epithelial cells by Zn^{2+} and other divalent cations." *J. Gen. Physiol.* **114**: 819-838.

Cubitt, A. B., R. Heim, S. R. Adams, A. E. Boyd, L. A. Gross and R. Y. Tsien (1995). "Understanding, improving and using green fluorescent proteins." *Trends Biochem Sci* **20**(11): 448-55.

Cukier, R. I. (2004). "Quantum molecular dynamics simulation of proton transfer in cytochrome c oxidase." *Biochim Biophys Acta* **1656**(2-3): 189-202.

Daldal, F., M. Deshmukh and R. C. Prince (2003). "Membrane-anchored cytochrome c as an electron carrier in photosynthesis and respiration: past, present and future of an unexpected discovery." *Photosynthesis Research* **76**(1-3): 127-134.

Daldal, F., S. Mandaci, C. Winterstein, H. Myllykallio, K. Duyck and D. Zannoni (2001). "Mobile cytochrome c2 and membrane-anchored cytochrome cy are both efficient electron donors to the cbb3- and aa3-type cytochrome c oxidases during respiratory growth of Rhodobacter sphaeroides." *J Bacteriol* **183**(6): 2013-2024.

Darrouzet, E., M. Valkova-Valchanova, C. C. Moser, P. L. Dutton and F. Daldal (2000). "Uncovering the [2Fe2S] domain movement in cytochrome bc1 and its implications for energy conversion." *Proc Natl Acad Sci U S A* **97**(9): 4567-72.

Dowhan, W., E. Mileykovskaya and M. Bogdanov (2004). "Diversity and versatility of lipid-protein interactions revealed by molecular genetic approaches." *Biochim Biophys Acta* **1666**(1-2): 19-39.

Durr, K. L., J. Koepke, P. Hellwig, H. Muller, H. Angerer, G. Peng, E. Olkhova, O. M. Richter, B. Ludwig and H. Michel (2008). "A D-pathway mutation decouples the Paracoccus denitrificans cytochrome c oxidase by altering the side-chain orientation of a distant conserved glutamate." *J Mol Biol* **384**(4): 865-77.

Elsliger, M. A., R. M. Wachter, G. T. Hanson, K. Kallio and S. J. Remington (1999). "Structural and spectral response of green fluorescent protein variants to changes in pH." *Biochemistry* **38**(17): 5296-301.

Ferguson-Miller, S. and G. Babcock (1996). "Heme/Copper Terminal Oxidases." *Chemical Reviews* **96**(7): 2889-2907.

Ferguson-Miller, S., D. Brautigan and E. Margoliash (1976). "Correlation of the Kinetics of Electron Transfer Activity of Various Eukaryotic Cytochrome c with Binding to Mitochondrial Cytochrome c Oxidase." *J. Biol. Chem* **251**: 1104-1115.

Fetter, J. R., J. Qian, J. Shapleigh, J. W. Thomas, A. Garcia-Horsman, E. Schmidt, J. Hosler, G. T. Babcock, R. B. Gennis and S. Ferguson-Miller (1995). "Possible proton relay pathways in cytochrome c oxidase." *Proc Natl Acad Sci U S A* **92**(5): 1604-8.

Flock, D. and V. Helms (2002). "Protein-protein docking of electron transfer complexes: cytochrome c oxidase and cytochrome c." *Proteins: Structure, Function, and Genetics* **47**(1): 75-85.

Fromme, P. and H. T. Witt (1998). "Improved isolation and crystallization of Photosystem I for structural analysis." *Biochim Biophys Acta* **1365**(1-2): 175-184.

Garavito, R. M. and S. Ferguson-Miller (2001). "Detergents as tools in membrane biochemistry." *J Biol Chem* **276**(35): 32403-32406.

Garcia-Horsman, J. A., B. Barquera, J. Rumbley, J. Ma and R. B. Gennis (1994). "The superfamily of heme-copper respiratory oxidases." *J Bacteriol* **176**(18): 5587-600.

Gilderson, G., L. Salomonsson, A. Aagaard, J. Gray, P. Brzezinski and J. Hosler (2003). "Subunit III of cytochrome c oxidase of Rhodobacter sphaeroides is required to maintain rapid proton uptake through the D pathway at physiologic pH." *Biochemistry* **42**(24): 7400-7409.

Gohon, Y. and J.-L. Popot (2003). "Membrane protein-surfactant complexes." *Current Opinion in Colloid & Interface Science* **8**(1): 15-22.

Gordeliy, V. I., J. Labahn, R. Moukhametzianov, R. Efremov, J. Granzin, R. Schlesinger, G. Bueldt, T. Savopol, A. J. Scheidig, J. P. Klare and M. Engelhard (2002). "Molecular basis of transmembrane signalling by sensory rhodopsin II-transducer complex." *Nature* **419**(6906): 484-487.

Hakansson, K. O. and J. R. Winther (2007). "Structure of glutaredoxin Grx1p C30S mutant from yeast." *Acta Crystallogr D Biol Crystallogr* **63**(Pt 3): 288-94.

Han, D., A. Namslauer, A. Pawate, J. E. Morgan, S. Nagy, A. S. Vakkasoglu, P. Brzezinski and R. B. Gennis (2006). "Replacing Asn207 by aspartate at the neck of the D channel in the aa3-type cytochrome c oxidase from Rhodobacter sphaeroides results in decoupling the proton pump." *Biochemistry* **45**(47): 14064-74.

Hanson, G. T., R. Aggeler, D. Oglesbee, M. Cannon, R. A. Capaldi, R. Y. Tsien and S. J. Remington (2004). "Investigating mitochondrial redox potential with redox-sensitive green fluorescent protein indicators." *J Biol Chem* **279**(13): 13044-53.

Harrenga, A. and H. Michel (1999). "The cytochrome c oxidase from Paracoccus denitrificans does not change the metal center ligation upon reduction." *J Biol Chem* **274**(47): 33296-33299.

Heim, R., D. C. Prasher and R. Y. Tsien (1994). "Wavelength mutations and posttranslational autoxidation of green fluorescent protein." *Proc Natl Acad Sci U S A* **91**(26): 12501-4.

Henry, R. M., C. H. Yu, T. Rodinger and R. Pomes (2009). "Functional hydration and conformational gating of proton uptake in cytochrome c oxidase." *J Mol Biol* **387**(5): 1165-85.

Hiser, C., D. A. Mills, M. Schall and S. Ferguson-Miller (2001). "C-Terminal Truncation and Histidine-Tagging of Cytochrome c Oxidase Subunit II Reveals the Native Processing Site, Shows Involvement of the C-Terminus in Cytochrome c Binding, and Improves the Assay for Proton Pumping." *Biochemistry* **40**(6): 1606-1615.

Hofacker, I. and K. Schulten (1998). "Oxygen and proton pathways in cytochrome c oxidase." *Proteins: Structure, Function, and Genetics* **30**(1): 100-107.

Hosler, J. P. (2004). "The influence of subunit III of cytochrome c oxidase on the D pathway, the proton exit pathway and mechanism-based inactivation in subunit I." *Biochim Biophys Acta* **1655**(1-3): 332-339.

Hosler, J. P., S. Ferguson-Miller and D. A. Mills (2006). "Energy Transduction: Proton Transfer Through the Respiratory Complexes." *Annu Rev Biochem.*

Hosler, J. P., J. Fetter, M. M. Tecklenburg, M. Espe, C. Lerma and S. Ferguson-Miller (1992). "Cytochrome aa3 of Rhodobacter sphaeroides as a model for mitochondrial cytochrome c oxidase. Purification, kinetics, proton pumping, and spectral analysis." *J Biol Chem* **267**(34): 24264-72.

Hosler, J. P., J. P. Shapleigh, D. M. Mitchell, Y. Kim, M. Pressler, C. Georgiou, G. T. Babcock, J. O. Alben, S. Ferguson-Miller and R. B. Gennis (1996). "Polar residues in helix VIII of subunit I of cytochrome *c* oxidase influence the activity and the structure of the active site." *Biochemistry* **35**: 10776-10783.

Hunte, C., J. Koepke, C. Lange, T. Rossmanith and H. Michel (2000). "Structure at 2.3 .ANG. resolution of the cytochrome bc1 complex from the yeast Saccharomyces cerevisiae co-crystallized with an antibody Fv fragment." *Structure* **8**(6): 669-684.

Iverson, T. M., C. Luna-Chavez, I. Schroder, G. Cecchini and D. C. Rees (2000). "Analyzing your complexes: structure of the quinol-fumarate reductase respiratory complex." *Curr Opin Struct Biol* **10**(4): 448-55.

Iwata, S., C. Ostermeier, B. Ludwig and H. Michel (1995). "Structure at 2.8 Å resolution of cytochrome c oxidase from Paracoccus denitrificans." *Nature* **376**: 660-669.

Kadenbach, B. (1986). "Regulation of respiration and ATP synthesis in higher organisms: hypothesis." *J Bioenerg Biomembr* **18**(1): 39-54.

Kadenbach, B. and S. Arnold (2000). "3,5-Diiodothyronine binds to subunit Va of cytochrome c oxidase: possible mechanism of short-term effects of thyroid hormones." *Membrane Structure in Disease and Drug Therapy*: 271-281.

Kadenbach, B., L. Kuhn-Nentwig and U. Buge (1987). *Curr. Topics Bioenergetics* **15**: 113 -161.

Kim, E., E. E. Chufan, K. Kamaraj and K. D. Karlin (2004). "Synthetic Models for Heme-Copper Oxidases." *Chemical Reviews* **104**(2): 1077-1133.

Koepke, J., E. Olkhova, H. Angerer, H. Muller, G. Peng and H. Michel (2009). "High resolution crystal structure of Paracoccus denitrificans cytochrome c oxidase: new insights into the active site and the proton transfer pathways." *Biochim Biophys Acta* **1787**(6): 635-45.

Kolbe, M., H. Besir, L.-O. Essen and D. Oesterhelt (2000). "Structure of the light-driven chloride pump halorhodopsin at 1.8 .ANG. resolution." *Science* **288**(5470): 1390-1396.

Konstantinov, A. A., S. Siletsky, D. Mitchell, A. Kaulen and R. B. Gennis (1997). "The roles of the two proton input channels in cytochrome c oxidase from Rhodobacter

sphaeroides probed by the effects of site-directed mutations on time-resolved electrogenic intraprotein proton transfer." *Proc Natl Acad Sci U S A* **94**(17): 9085-9090.

Kuo, A., M. W. Bowler, J. Zimmer, J. F. Antcliff and D. A. Doyle (2003). "Increasing the diffraction limit and internal order of a membrane protein crystal by dehydration." *Journal of Structural Biology* **141**(2): 97-102.

Landau, E. M. and J. P. Rosenbusch (1996). "Lipidic cubic phases: a novel concept for the crystallization of membrane proteins." *Proc Natl Acad Sci U S A* **93**(25): 14532-14535.

le Maire, M., P. Champeil and J. V. Moller (2000). "Interaction of membrane proteins and lipids with solubilizing detergents." *Biochim Biophys Acta* **1508**(1-2): 86-111.

Lee, H.-m., T. K. Das, D. L. Rousseau, D. Mills, S. Ferguson-Miller and R. B. Gennis (2000). "Mutations in the Putative H-Channel in the Cytochrome c Oxidase from Rhodobacter sphaeroides Show That This Channel Is Not Important for Proton Conduction but Reveal Modulation of the Properties of Heme a." *Biochemistry* **39**(11): 2989-2996.

Lepp, H., E. Svahn, K. Faxen and P. Brzezinski (2008). "Charge transfer in the K proton pathway linked to electron transfer to the catalytic site in cytochrome c oxidase." *Biochemistry* **47**(17): 4929-35.

Liu, B., Y. Chen, T. Doukov, S. M. Soltis, C. D. Stout and J. A. Fee (2009). "Combined microspectrophotometric and crystallographic examination of chemically reduced and X-ray radiation-reduced forms of cytochrome ba3 oxidase from Thermus thermophilus: structure of the reduced form of the enzyme." *Biochemistry* **48**(5): 820-6.

Luecke, H., B. Schobert, H.-T. Richter, J.-P. Cartailler and J. K. Lanyi (1999). "Structure of bacteriorhodopsin at 1.55 .ANG. resolution." *J Mol Biol* **291**(4): 899-911.

MacMillan, F., A. Kannt, J. Behr, T. Prisner and H. Michel (1999). "Direct Evidence for a Tyrosine Radical in the Reaction of Cytochrome c Oxidase with Hydrogen Peroxide." *Biochemistry* **38**(29): 9179-9184.

Maneg, O., F. Malatesta, B. Ludwig and V. Drosou (2004). "Interaction of cytochrome c with cytochrome oxidase: two different docking scenarios." *Biochim Biophys Acta* **1655**(1-3): 274-281.

McLuskey, K., S. M. Prince, R. J. Cogdell and N. W. Isaacs (2001). "The crystallographic structure of the B800-820 LH3 light-harvesting complex from the purple bacteria Rhodopseudomonas acidophila strain 7050." *Biochemistry* **40**(30): 8783-9.

Michel, H. (1982). "Three-dimensional crystals of a membrane protein complex. The photosynthetic reaction center from Rhodopseudomonas viridis." *J Mol Biol* **158**(3): 567-72.

Michel, H. (1998). "The Mechanism of Proton Pumping by Cytochrome *c* Oxidase." *Proc Natl Acad Sci U S A* **95**: 12819-12824.

Michel, H. (1999). "Cytochrome c Oxidase: Catalytic Cycle and Mechanisms of Proton Pumping-A Discussion." *Biochemistry* **38**(46): 15129-15140.

Michel, H., J. Behr, A. Harrenga and A. Kannt (1998). "Cytochrome c oxidase: structure and spectroscopy." *Annu Rev Biophys Biomol Struct* **27**: 329-56.

Miesenbock, G., D. A. De Angelis and J. E. Rothman (1998). "Visualizing secretion and synaptic transmission with pH-sensitive green fluorescent proteins." *Nature* **394**(6689): 192-5.

Mills, D. A. and S. Ferguson-Miller (1998). "Proton uptake and release in cytochrome c oxidase:seperate pathways in time and space?" *Biochim Biophys Acta* **1365**: 46-52.

Mills, D. A. and S. Ferguson-Miller (2003). "Understanding the mechanism of proton movement linked to oxygen reduction in cytochrome c oxidase: lessons from other proteins." *Febs Letters* **545**(1): 47-51.

Mills, D. A., L. Florens, C. Hiser, J. Qian and S. Ferguson-Miller (2000). "Where is 'outside' in cytochrome c oxidase and how and when do protons get there?" *Biochim Biophys Acta* **1458**(1): 180-187.

Mills, D. A., J. P. Hosler (2005). "Slow proton transfer through the pathways for pumped protons in cytochrome *c* oxidase induces suicide inactivation of the enzyme." *Biochemistry* **44**((12)): 4656-4666.

Mills, D. A., B. Schmidt, C. Hiser, E. Westley and S. Ferguson-Miller (2002). "Membrane potential-controlled inhibition of cytochrome *c* oxidase by zinc." *J. Biol. Chem.* **277**: 14894-14901.

Mills, D. A., Z. Tan, S. Ferguson-Miller and J. Hosler (2003). "A role for subunit III in proton uptake into the D pathway and a possible proton exit pathway in Rhodobacter sphaeroides cytochrome c oxidase." *Biochemistry* **42**(24): 7410-7417.

Muramoto, K., K. Hirata, K. Shinzawa-Itoh, S. Yoko-o, E. Yamashita, H. Aoyama, T. Tsukihara and S. Yoshikawa (2007). "A histidine residue acting as a controlling site for dioxygen reduction and proton pumping by cytochrome c oxidase." *Proc Natl Acad Sci U S A* **104**(19): 7881-6.

Murshudov, G. N., A. A. Vagin and E. J. Dodson (1997). "Refinement of macromolecular structures by the maximum-likelihood method." *Acta Crystallogr D Biol Crystallogr* **D53**(3): 240-255.

Nicholls, P. (1975). "The effect of sulphide on cytochrome aa3. Isosteric and allosteric shifts of the reduced alpha-peak." *Biochim Biophys Acta* **396**(1): 24-35.

Nicholls, P., V. Hildebrandt and J. Wrigglesworth (1980). "Orientation and reactivity of cytochrome aa_3 heme groups in proteoliposomes." *Arch. Biochem. Biophys.* **204**: 533-543.

Ormoe, M., A. Cubitt, K. Kallio, L. Gross, R. Tsien and J. Remington (1996). "Crystal structure of the Aequorea victoria green fluorescent protein." *Science* **273**: 1392-1395.

Ostermeier, C., A. Harrenga, U. Ermler and H. Michel (1997). "Structure at 2.7 .ANG. resolution of the Paracoccus denitrificans two-subunit cytochrome c oxidase complexed with an antibody Fv fragment." *Proc Natl Acad Sci U S A* **94**(20): 10547-10553.

Otwinowski, Z. and W. Minor (1997). "Processing of x-ray diffraction data collected in oscillation mode." *Methods in Enzymology* **276**(Macromolecular Crystallography, Part A): 307-326.

Pan, L. P., S. Hibdon, R. Q. Liu, B. Durham and F. Millett (1993). "Intracomplex electron transfer between ruthenium-cytochrome c derivatives and cytochrome c oxidase." *Biochemistry* **32**(33): 8492-8.

Pautsch, A., J. Vogt, K. Model, C. Siebold and G. E. Schulz (1999). "Strategy for membrane protein crystallization exemplified with OmpA and OmpX." *Proteins: Structure, Function, and Genetics* **34**(2): 167-172.

Pawate, A. S., J. Morgan, A. Namslauer, D. Mills, P. Brzezinski, S. Ferguson-Miller and R. B. Gennis (2002). "A mutation in subunit I of cytochrome oxidase from *Rhodobacter sphaeroides* results in an increase in steady-state activity but completely eliminates proton pumping." *Biochemistry* **41**(45): 13417-23.

Pearson, A. R., R. Pahl, E. G. Kovaleva, V. L. Davidson and C. M. Wilmot (2007). "Tracking X-ray-derived redox changes in crystals of a methylamine dehydrogenase/amicyanin complex using single-crystal UV/Vis microspectrophotometry." *J Synchrotron Radiat* **14**(Pt 1): 92-8.

Peiffer, W. E., R. T. Ingle and S. Ferguson-Miller (1990). "Structurally unique plant cytochrome c oxidase isolated from wheat germ, a rich source of plant mitochondrial enzymes." *Biochemistry* **29**(37): 8696-701.

Pfitzner, U., K. Hoffmeier, A. Harrenga, A. Kannt, H. Michel, E. Bamberg, O. M. Richter and B. Ludwig (2000). "Tracing the D-pathway in reconstituted site-directed mutants of cytochrome *c* oxidase from *Paracoccus denitrificans*." *Biochemistry* **39**(23): 6756-62.

Pollok, B. A. and R. Heim (1999). "Using GFP in FRET-based applications." *Trends Cell Biol* **9**(2): 57-60.

Proshlyakov, D. A., M. A. Pressler, C. DeMaso, J. F. Leykam, D. L. DeWitt and G. T. Babcock (2000). "Oxygen activation and reduction in respiration: involvement of redox-active tyrosine 244." *Science* **290**(5496): 1588-91.

Qian, J., D. A. Mills, L. Geren, K. Wang, C. W. Hoganson, B. Schmidt, C. Hiser, G. T. Babcock, B. Durham, F. Millett and S. Ferguson-Miller (2004). "Role of the Conserved Arginine Pair in Proton and Electron Transfer in Cytochrome c Oxidase." *Biochemistry* **43**(19): 5748-5756.

Qin, L., C. Hiser, A. Mulichak, R. M. Garavito and S. Ferguson-Miller (2006). "Identification of conserved lipid/detergent-binding sites in a high-resolution structure of the membrane protein cytochrome c oxidase." *Proc Natl Acad Sci U S A* **103**(44): 16117-22.

Qin, L., J. Liu, D. A. Mills, D. A. Proshlyakov, C. Hiser and S. Ferguson-Miller (2009). "Redox-dependent conformational changes in cytochrome C oxidase suggest a gating mechanism for proton uptake." *Biochemistry* **48**(23): 5121-30.

Qin, L., D. A. Mills, L. Buhrow, C. Hiser and S. Ferguson-Miller (2008). "A conserved steroid binding site in cytochrome C oxidase." *Biochemistry* **47**(38): 9931-3.

Ramirez, B. E., B. G. Malmstrom, J. R. Winkler and H. B. Gray (1995). "The currents of life: the terminal electron-transfer complex of respiration." *Proc Natl Acad Sci U S A* **92**(26): 11949-51.

Regan, J. J., B. E. Ramirez, J. R. Winkler, H. B. Gray and B. G. Malmstrom (1998). "Pathways for electron tunneling in cytochrome c oxidase." *J Bioenerg Biomembr* **30**(1): 35-39.

Roberts, V. A. and M. E. Pique (1999). "Definition of the interaction domain for cytochrome c on cytochrome c oxidase.: III. Prediction of the docked complex by a complete, systematic search." *J Biol Chem* **274**(53): 38051-38060.

Rosevear, P., T. VanAken, J. Baxter and S. Ferguson-Miller (1980). "Alkyl glycoside detergents: a simpler synthesis and their effects on kinetic and physical properties of cytochrome c oxidase." *Biochemistry* **19**(17): 4108-15.

Sack, J. S. and F. A. Quiocho (1997). "CHAIN: A crystallographic modeling program." *Methods in Enzymology* **277**(Macromolecular Crystallography, Part B): 158-173.

Schmidt, B., J. McCracken and S. Ferguson-Miller (2003). "A discrete water exit pathway in the membrane protein cytochrome *c* oxidase." *Proc Natl Acad Sci U S A* **In press.**

Schultz, S.I. and S. Chan (2001). Structures and proton-pumping strategies of mitochondrial respiratory enzymes. Annu Rev Biophys Struct **30:** 23-65.

Shapleigh, J. P., J. J. Hill, J. O. Alben and R. B. Gennis (1992). "Spectroscopic and Genetic Evidence for Two Heme-Cu Containing Oxidases in *Rhodobacter sphaeroides*." *J. Bacteriol.* **174**: 2338-43.

Sharma, V., M. Wikstrom and L. Laakkonen (2008). "Modeling the active-site structure of the cbb3-type oxidase from Rhodobacter sphaeroides." *Biochemistry* **47**(14): 4221-7.

Sharpe, M., I. Perin, J. Wrigglesworth and P. Nicholls (1996). "Fatty acids as modulators of cytochrome c oxidase in proteoliposomes." *Biochemical Journal* **320**(2): 557-561.

Sharpe, M., L. Qin and S. Ferguson-Miller (2005). Proton entry, exit and pathways in cytochrome oxidase: Insight from "Conserved" Water. Biophysical and Structural Aspects of Bioenergetics. M. Wikstroem. Cambridge, accepted, Royal Society of Chemistry.

Sharpe, M. A. and S. Ferguson-Miller (2008). "A chemically explicit model for the mechanism of proton pumping in heme-copper oxidases." *J Bioenerg Biomembr* **40**(5): 541-9.

Shimomura, O., F. H. Johnson and Y. Saiga (1962). "Extraction, purification and properties of aequorin, a bioluminescent protein from the luminous hydromedusan, Aequorea." *J Cell Comp Physiol* **59**: 223-39.

Shinzawa-Itoh, K., H. Aoyama, K. Muramoto, H. Terada, T. Kurauchi, Y. Tadehara, A. Yamasaki, T. Sugimura, S. Kurono, K. Tsujimoto, T. Mizushima, E. Yamashita, T. Tsukihara and S. Yoshikawa (2007). "Structures and physiological roles of 13 integral lipids of bovine heart cytochrome c oxidase." *Embo J.*

Smith, P. K., R. I. Krohn, G. T. Hermanson, A. K. Mallia, F. H. Gartner, M. D. Provenzano, E. K. Fujimoto, N. M. Goeke, B. J. Olson and D. C. Klenk (1985). "Measurement of protein using bicinchoninic acid." *Analytical Biochemistry* **150**(1): 76-85.

Steinrucke, P., G. C. Steffens, G. Panskus, G. Buse and B. Ludwig (1987). "Subunit II of cytochrome c oxidase from Paracoccus denitrificans. DNA sequence, gene expression and the protein." *European journal of biochemistry / FEBS* **167**(3): 431-9.

Storoni, L. C., A. J. McCoy and R. J. Read (2004). "Likelihood-enhanced fast rotation functions." *Acta Crystallogr D Biol Crystallogr* **D60**(3): 432-438.

Suzuki, N., M. Hiraki, Y. Yamada, N. Matsugaki, N. Igarashi, R. Kato, I. Dikic, D. Drew, S. Iwata, S. Wakatsuki and M. Kawasaki (2010). "Crystallization of small proteins assisted by green fluorescent protein." *Acta Crystallogr D Biol Crystallogr* **66**(Pt 10): 1059-66.

Svensson-Ek, M., J. Abramson, G. Larsson, S. Tornoth, P. Brzezinski and S. Iwata (2002). "The X-ray crystal structures of wild-type and EQ(I-286) mutant cytochrome c oxidases from Rhodobacter sphaeroides." *J. Mol. Biol.* **321**: 329-339.

Swaminathan, R., C. P. Hoang and A. S. Verkman (1997). "Photobleaching recovery and anisotropy decay of green fluorescent protein GFP-S65T in solution and cells: cytoplasmic viscosity probed by green fluorescent protein translational and rotational diffusion." *Biophys J* **72**(4): 1900-7.

Tan, M.-L., I. Balabin and J. N. Onuchic (2004). "Dynamics of electron transfer pathways in cytochrome c oxidase." *Biophysical Journal* **86**(3): 1813-1819.

Tomson, F., J. A. Bailey, R. B. Gennis, C. J. Unkefer, Z. Li, L. A. Silks, R. A. Martinez, R. J. Donohoe, R. B. Dyer and W. H. Woodruff (2002). "Direct Infrared Detection of the Covalently Ring Linked His-Tyr Structure in the Active Site of the Heme-Copper Oxidases." *Biochemistry* **41**(48): 14383-14390.

Tomson, F. L., J. Morgan, G. Gu, B. Barquera, T. V. Vygodina and R. B. Gennis (2003). "Substitutions for Glutamate 101 in Subunit II of Cytochrome c Oxidase from Rhodobacter sphaeroides Result in Blocking the Proton-Conducting K-Channel." *Biochemistry* **42**(6): 1711-1717.

Tsien, R. Y. (1998). "The green fluorescent protein." *Annu Rev Biochem* **67**: 509-44.

Tsukihara, T., H. Aoyama, E. Yamashita, T. Tomizaki, H. Yamaguchi, K. Shinzawa-Itoh, R. Nakashima, R. Yaono and S. Yoshikawa (1996). "The whole structure of the 13-subunit oxidized cytochrome c oxidase at 2.8 .ANG." *Science* **272**(5265): 1136-1144.

Tsukihara, T., K. Shimokata, Y. Katayama, H. Shimada, K. Muramoto, H. Aoyama, M. Mochizuki, K. Shinzawa-itoh, E. Yamashita, M. Yao, Y. Ishimura and S. Yoshikawa (2003). "The low-spin heme of cytochrome c oxidase as the driving element of the proton-pumping process." *Proc Natl Acad Sci U S A* **100**(26): 15304-15309.

Vygodina, T. V., N. Capitanio, S. Papa and A. A. Konstantinov (1997). "Proton pumping by cytochrome c oxidase is coupled to peroxidase half of its catalytic cycle." *FEBS Letters* **412**(3): 405-409.

Wadhams, G. H., A. C. Martin and J. P. Armitage (2000). "Identification and localization of a methyl-accepting chemotaxis protein in Rhodobacter sphaeroides." *Mol Microbiol* **36**(6): 1222-33.

Wang, K., Y. Zhen, R. Sadoski, S. Grinnell, L. Geren, S. Ferguson-Miller, B. Durham and F. Millett (1999). "Definition of the interaction domain for cytochrome c on cytochrome c oxidase.: II. Rapid kinetic analysis of electron transfer from cytochrome c to Rhodobacter sphaeroides cytochrome oxidase surface mutants." *J Biol Chem* **274**(53): 38042-38050.

Wikstrom, M., A. Bogachev, M. Finel, J. E. Morgan, A. Puustinen, M. Raitio, M. Verkhovskaya and M. I. Verkhovsky (1994). "Mechanism of proton translocation by the respiratory oxidases. The histidine cycle." *Biochim Biophys Acta* **1187**(2): 106-11.

Wikstrom, M., A. Jasaitis, C. Backgren, A. Puustinen and M. I. Verkhovsky (2000). "The role of the D- and K-pathways of proton transfer in the function of the haem-copper oxidases." *Biochim Biophys Acta* **1459**(2-3): 514-20.

Wikstrom, M. and H. Saari (1975). "A spectral shift in cytochrome a induced by calcium ions." *Biochim Biophys Acta* **408**(2): 170-9.

Wikstrom, M. and M. I. Verkhovsky (2002). "Proton translocation by cytochrome c oxidase in different phases of the catalytic cycle." *Biochim Biophys Acta* **1555**(1-3): 128-132.

Winn, M. D., M. N. Isupov and G. N. Murshudov (2001). "Use of TLS parameters to model anisotropic displacements in macromolecular refinement." *Acta Crystallogr D Biol Crystallogr* **D57**(1): 122-133.

Witt, H., F. Malatesta, F. Nicoletti, M. Brunori and B. Ludwig (1998). "Tryptophan 121 of subunit II is the electron entry site to cytochrome-c oxidase in Paracoccus denitrificans. Involvement of a hydrophobic patch in the docking reaction." *J Biol Chem* **273**(9): 5132-5136.

Xu, J., M. A. Sharpe, L. Qin, S. Ferguson-Miller and G. A. Voth (2007). "Storage of an excess proton in the hydrogen-bonded network of the d-pathway of cytochrome C oxidase: identification of a protonated water cluster." *J Am Chem Soc* **129**(10): 2910-3.

Yagi, T., T. Yano, S. Di Bernardo and A. Matsuno-Yagi (1998). "Procaryotic complex I (NDH-1), an overview." *Biochim Biophys Acta* **1364**(2): 125-33.

Yao, N., P. S. Ledvina, A. Choudhary and F. A. Quiocho (1996). "Modulation of a salt link does not affect binding of phosphate to its specific active transport receptor." *Biochemistry* **35**(7): 2079-85.

Yoshikawa, S., K. Shinzawa-Itoh, R. Nakashima, R. Yaono, E. Yamashita, N. Inoue, M. Yao, M. J. Fei, C. P. Libeu, T. Mizushima, H. Yamaguchi, T. Tomizaki and T. Tsukihara (1998). "Redox-coupled crystal structural changes in bovine heart cytochrome c oxidase." *Science* **280**(5370): 1723-9.

Zaslavsky, D. and R. Gennis (1998). "Substitution of lysine-362 in a putative proton-conducting channel in the cytochrome *c* oxidase from *Rhodobacter sphaeroides* blocks turnover with O_2 but not with H_2O_2." *Biochemistry* **37**: 3062-3067.

Zaslavsky, D. and R. B. Gennis (2000). "Proton pumping by cytochrome oxidase: progress, problems and postulates." *Biochim Biophys Acta* **1458**(1): 164-179.

Zhen, Y., C. W. Hoganson, G. T. Babcock and S. Ferguson-Miller (1999). "Definition of Interaction Domain for the Reaction of Cytochrome c with Cytochrome c Oxidase: I. Biochemical, spectral and kinetic characterization of surface mutants in subinit II of Rhodobacter sphaeroides cytochrome aa3." *J. Biol. Chem.* **274**: 38032-38041.

Zhen, Y., J. Qian, K. Follmann, T. Hayward, T. Nilsson, M. Dahn, Y. Hilmi, A. G. Hamer, J. P. Hosler and S. Ferguson-Miller (1998). "Overexpression and purification of cytochrome c oxidase from Rhodobacter sphaeroides." *Protein Expr Purif* **13**(3): 326-36.

Zhen, Y., B. Schmidt, U. G. Kang, W. Antholine and S. Ferguson-Miller (2002). "Mutants of the CuA site in cytochrome c oxidase of Rhodobacter sphaeroides: I. Spectral and functional properties." *Biochemistry* **41**(7): 2288-2297.

Zhou, Y., J. H. Morals-Cabral, A. Kaufman and R. MacKinnon (2001). "Chemistry of ion coordination and hydration revealed by a K+ channel-Fab complex at 2.0ANG. resolution." *Nature* **414**(6859): 43-48.

Zhu, J., H. Han, A. Pawate and R. B. Gennis (2010). "Decoupling mutations in the D-channel of the aa(3)-type cytochrome c oxidase from Rhodobacter sphaeroides suggest that a continuous hydrogen-bonded chain of waters is essential for proton pumping." *Biochemistry* **49**(21): 4476-82.